4. EXPLANATORY NOTES[1]

Shipboard Scientific Party[2]

INTRODUCTION

In this chapter, we have assembled information that will help the reader understand the observations on which our preliminary conclusions are based and provide guidance to investigators who wish to select samples for further analysis. This information concerns only shipboard operations and analyses described in the site reports in the *Initial Reports* volume of the Leg 155 *Proceedings of the Ocean Drilling Program*. Methods used by various investigators for shore-based analyses of Leg 155 data will be described in the individual scientific contributions to be published in the *Scientific Results* volume.

Authorship of Site Chapters

The separate sections of the site chapters were written by the following shipboard scientists (authors are listed in alphabetical order; no seniority is implied):

Site Summary: Flood, Piper
Setting and Objectives: Flood, Piper
Operations: Klaus, Pollard
Lithostratigraphy: Cramp, Damuth, Hiscott, Kowsmann, Lopez, Nanayama, Normark, Schneider
Biostratigraphy: Haberle, Maslin, Mikkelsen, Showers
Paleomagnetism: Cisowski, Hall
Organic Geochemistry: Goni, Hinrichs
Inorganic Geochemistry: Burns, McDaniel
Physical Properties: Busch, Long, Manley, Soh
Downhole Logging: Kronen, Pirmez, Thibal
Core-Seismic Integration: Damuth, Klaus, Lopez, Manley, Pirmez
In-situ Temperature Measurements: Kronen
Synthesis and Significance: Flood, Piper

Following the text of all the site chapters, summary core descriptions and photographs of each core can be found in the "Cores" section.

Shipboard Scientific Procedures

Numbering of Sites, Holes, Cores, and Samples

ODP drill sites are numbered consecutively, and refer to one or more holes drilled while the ship was positioned over one acoustic beacon. Multiple holes may be drilled at a single site by pulling the drill pipe above the seafloor (out of the hole), moving the ship some distance from the previous hole, and then drilling another hole. A letter suffix (A, B, C, etc.) distinguishes holes drilled sequentially at the same site. (Note that this procedure differs slightly from that used by DSDP, Sites 1 through 624.) Sediments recovered at the same nominal depth from different holes may not come from exactly equivalent positions in the stratigraphic column.

The cored interval is measured in meters below seafloor (mbsf). The depth interval assigned to an individual core begins with the depth below the seafloor at which the coring began, and extends to the depth at which the coring ended (see previous *Initial Reports* volumes, e.g., p. 16 of Gillis, Mével, Allan, et al., 1993). When the recovered core is shorter than the cored interval, the top of the recovered core is assigned to the top of the cored interval. Generally each coring interval is 9.5 m long, the length of a core barrel, but coring intervals may be shorter. They may not necessarily be adjacent if separated by drilled intervals. In soft sediments, the drill string can be washed ahead with the core barrel in place, without recovering sediments. This is achieved by pumping water down the pipe at high pressure to wash the sediment out of the way of the bit and up the space between the drill pipe and the wall of the hole. During Leg 155, we experienced considerable problems with core liners breaking within the core barrel, making it difficult to remove the liner. Such cores are noted in the "Operations" section of each site chapter. Some physical property measurements from such cores may be of questionable value.

Cores taken from a hole are numbered serially from the top of the hole downward. Core numbers and their associated cored intervals in meters below seafloor usually are unique in a given hole. Maximum recovery for a single core is normally 9.5 m of sediment contained in a plastic liner (6.6 cm internal diameter) plus about 0.2 m (without a plastic liner) in the core catcher. The core catcher is a device at the bottom of the core barrel that prevents the core from sliding out when the barrel is being retrieved from the hole. When coring gas-charged sediments that expand while being brought on deck, recovery may exceed the 9.5-m maximum. In some Leg 155 cores, gas expansion was so severe that as much as a meter of core was extruded on the rig floor. This sediment was replaced in plastic liners, but in some cases sections from the rig floor may have been placed in the liner in the wrong sequence or may have been inverted. In all cases, this sediment was highly disturbed. Information on such extruded sections is noted in the "Operations" section of each site chapter.

A recovered core is divided into 1.5-m sections that are numbered serially from the top (see previous *Initial Reports* volumes, e.g., p. 16 of Gillis, Mével, Allan, et al., 1993). When full recovery is obtained, the sections are numbered from 1 through 7, with the last section generally being shorter than 1.5 m (rarely, an unusually long core may require more than 7 sections). When less than full recovery is obtained, there will be as many sections as needed to accommodate the length of the core recovered; for example, 4 m of core would be divided into two 1.5-m sections and a 1-m section. If individual cores contain discontinuous packages of sediment, the sections are numbered serially and intervening sections are noted as void, whether shipboard scientists think that the fragments were contiguous in situ or not. Voids are not systematically closed by sliding sediment within the core liner. In rare cases a section less than 1.5 m may be cut to preserve features of interest (e.g., lithologic contacts). When the core is described, material recovered from the core catcher is treated as a separate section below the last regular section.

[1]Flood, R.D., Piper, D.J.W., Klaus, A., et al., 1995. *Proc. ODP, Init. Repts.*, 155: College Station, TX (Ocean Drilling Program).
[2]Shipboard Scientific Party is as given in the list of participants in the contents.

Samples removed from the cores are designated by distance measured in centimeters from the top of the section to the top and bottom of each sample removed from that section. A full identification number for a sample consists of the following information: leg, site, hole, core number, core type, section number, and interval in centimeters measured from the top of the section. For example, a sample identification of "155-930A-5H-1, 10–12 cm" represents a sample removed from the interval between 10 and 12 cm below the top of Section 1, Core 5 (H designates that this core was taken using the advanced hydraulic piston corer) of Hole 930A during Leg 155. Because of the large number of voids caused by gas expansion in Leg 155 sediments, sedimentological logs were prepared with larger voids removed and sediment positions adjusted accordingly (see back-pocket foldout). The sub-bottom depths recorded on these logs therefore do not correspond exactly to depths calculated for samples. For this reason, investigators who wish to precisely relate samples to sedimentological features should request the relevant section-by-section handwritten core-description forms from ODP.

All ODP core and sample identifiers indicate core type. The following abbreviations are used: H = Hydraulic Piston Corer (HPC; also referred to as APC, or Advanced Hydraulic Piston Corer); P = Pressure Core Sampler (PCS); X = Extended Core Barrel (XCB); W = wash-core recovery; and M = miscellaneous material. APC, XCB, W, and PCS cores were cut on Leg 155.

Core Handling

As soon as a core is retrieved on deck, a sample is taken from the core catcher and given to the paleontological laboratory for an initial age assessment. The core is then placed on the long horizontal rack, and gas samples may be taken by piercing the core liner where there are voids and withdrawing gas into a vacuum tube. Some of the gas samples are stored for shore-based study, but others are analyzed immediately as part of the shipboard safety and pollution-prevention program. Next, the core is marked into section lengths, each section is labeled, and the core is cut into sections. Interstitial-water (IW) and physical properties (PP) whole-round samples are then taken. In addition, a small tube of sediment is taken from the ends of cut sections for analysis of headspace gas, and sealed in glass vials for light hydrocarbon analysis. Each section is then sealed at the top and bottom using acetone to seal color-coded plastic caps to the core liner. When organically clean samples are desired, the plastic caps are attached to the liner with tape instead of acetone.

If the core begins expanding, holes are punctured through the core liner at voids (presumably where there is gas) to minimize disturbance to the core. When gas caused the sediments to extrude from the core liners, core liner extensions were attached to the 1.5-m-long core sections (or where IW samples were taken) to maintain the stratigraphic position of the sediment. In some cases, this additional core liner affected some of the whole-core pass-through measurements. Following core splitting, the original liner and the extension are sealed together with acetone.

The cores then are carried into the laboratory, where the sections are again labeled, using an engraver to permanently mark the full designation of the section. The length of the core in each section and the core-catcher sample are measured to the nearest centimeter; this information is logged into the shipboard CORELOG database program. After the core has equilibrated to room temperature (approximately 3–4 hr), whole-round sections from APC and XCB cores normally are run through the multisensor track (MST). The MST includes the gamma-ray attenuation porosity evaluator (GRAPE) and *P*-wave logger devices, which measure bulk density, porosity, and sonic velocity. The MST also contains a meter that determines volume magnetic susceptibility and a natural gamma detector. On selected cores, thermal conductivity measurements were performed.

Next, the cores are split lengthwise into working and archive halves. During Leg 155, cores were split with a wire. The wire-cut cores are split from the bottom to top, so investigators should be aware that older material could have been transported up the core on the split face of each section.

The working half of the core is sampled for both shipboard and shore-based laboratory studies. Each extracted sample is logged into the sampling computer database program by the location and the name of the investigator receiving the sample. Records of all samples taken are kept by the curator at ODP. The extracted samples are sealed in plastic vials or bags and labeled. Samples are routinely taken for shipboard analyses including those for physical properties, paleomagnetism, and inorganic geochemistry and organic carbon (CNS elemental analyzer), and the data are reported in the site chapters.

As soon as possible after splitting, the archive half is scraped clean and described visually. Then it is photographed with both black-and-white and color film, a whole core at a time. Leg 155 sediments changed color rapidly upon exposure to air. Colors in photographs thus depend on the elapsed time between splitting and photography, and whether the surface of the core was scraped to expose fresh sediment immediately before photography. Investigators who re-examine the cores in the repository will find that the cores have oxidized to a uniform color and that many of the features identified aboard ship are no longer visible. Smear slides are made from samples taken from the archive half, and are supplemented by thin sections taken from the working half. Most archive sections are run through the cryogenic magnetometer. Close-up photographs (black-and-white) are taken of particular features for illustrations in the summary of each site, as requested by individual scientists.

Both halves of the core are then put into labeled plastic tubes, sealed, and transferred to cold-storage space aboard the drilling vessel. At the end of Leg 155, the cores were transferred from the ship in refrigerated airfreight containers to cold storage at the Bremen Repository of the Ocean Drilling Program, at the Universität Bremen, Bremen, Germany.

LITHOSTRATIGRAPHY

The following methods are described in this section:

1. Visual description of sediment cores and the procedure followed to condense these descriptions into computer-generated summary sheets using the ODP "VCD" program.
2. Procedures for sediment classification.
3. Construction of graphic sedimentological logs that appear in the "Lithostratigraphy" section of each site chapter and in the back-pocket foldout.
4. X-ray diffraction methods used to analyze the mineralogy of selected sediment samples.
5. Routine measurement of sediment color using a spectrophotometer.
6. Procedures used in the X-radiography of selected core intervals.
7. Preparation of thin sections of samples taken from laminated muds, and petrographic classification of sands in thin section.

Visual Core Description and the Barrel Sheet Program "VCD"

Sedimentologists were responsible for visual core descriptions, smear-slide analyses, and thin-section descriptions. Information from megascopic description of each core was recorded manually section by section on visual core description (VCD) paper forms (eight forms for each full core; vertical scale 1:6.7). This information was then condensed and entered into the ODP "VCD" computer program, which generates a simplified, one-page graphical core description.

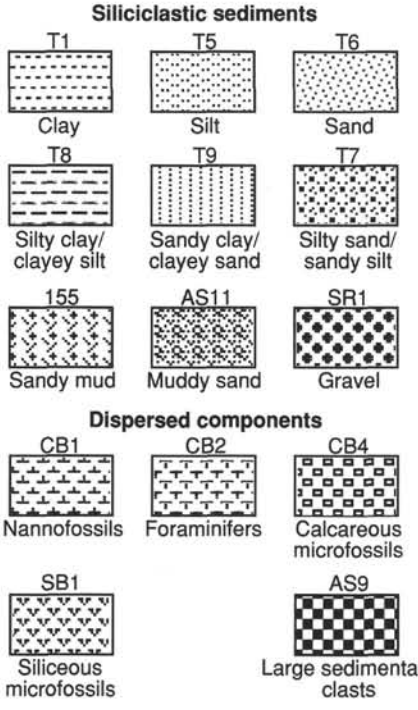

Figure 1. Key to patterns used to represent lithology in the "Graphic Lithology" column of the computer-generated core description forms, which follow the text of all the site chapters.

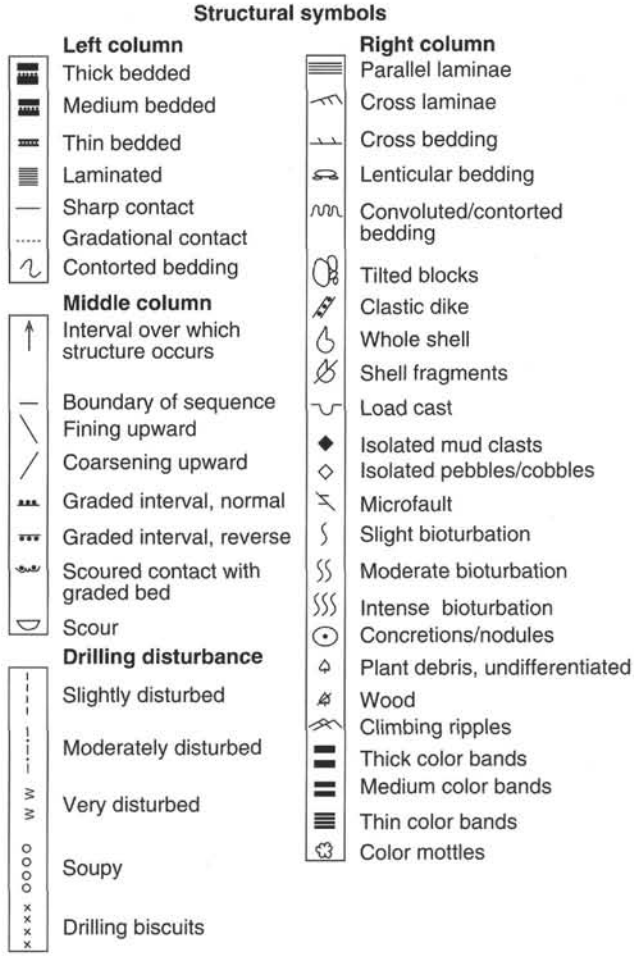

Figure 2. Key to symbols used to represent sedimentary structures, components, and drilling disturbance in the "Structure" and "Drilling Disturbance" columns of the computer-generated core description forms.

These descriptions are presented with whole-core photographs and smear-slide data following the text of all the site chapters.

The lithology of the recovered material is shown on the computer-generated core description forms by symbols representing up to three components (Fig. 1), separated by vertical lines, in the column entitled "Graphic Lithology." Amazon Fan sediment generally contains small percentages of biogenic particles (e.g., nannofossils, foraminifers, spicules) that are dispersed in muds of variable texture, where mud is defined as a mixture of silt and clay (grain-size divisions for sand, silt, and clay are those of Wentworth, 1922). Sediment with a biogenic fraction greater than 10% has this biogenic component plotted as a vertical strip on the right side of the "Graphic Lithology" column, with the implication that the biogenic grains are dispersed in the coexisting muddy sediment. The nonbiogenic fraction is represented by a single symbol if it is homogeneous in texture, or by two "Siliciclastic Sediment" symbols (Fig. 1) if texturally distinct siliciclastic sediments are interbedded (for example, interbeds of sand and silty clay forming sand-mud couplets). The relative width of the columns indicates the relative proportion of each type of siliciclastic sediment in the interbedded section. The position of sediment symbols in the "Graphic Lithology" column is, from left to right, the coarsest siliciclastic sediment (e.g., sand or silt), the finer grained siliciclastic sediment (e.g., clays or silty clays), and finally the biogenic components.

Large sedimentary clasts (predominantly mud clasts) form a special component of some muddy sand and sandy mud units and are represented in the "Graphic Lithology" column by a special symbol whose width shows the proportion of the sediment that is formed of mud clasts.

Constituents accounting for <10% of a given lithology (or others remaining after the representation of the three most abundant lithologies and components) cannot be shown in the "Graphic Lithology" column, but are listed in the "Lithologic Description" section of the core description form (see below).

Chronostratigraphic units were identified by shipboard paleontologists and paleomagnetists, and are recorded in the "Age" column on the barrel sheets. Boundaries are indicated as follows: sharp boundary = straight line; unconformity or hiatus = line with + signs above; uncertain boundary = line with question marks.

The "Structure" column is used to indicate a variety of features that characterize the sediment, such as bed thicknesses, primary sedimentary structures, soft-sediment deformation, and diagenetic features (Fig. 2). The symbols are schematic and are placed as close as possible to their proper stratigraphic position; for exact positions of sedimentary features, the detailed, section-by-section, paper core description forms can be obtained from ODP. The "Structure" column is divided into three vertical windows:

1. The left window displays symbols indicating thickness of sand-mud or silt-mud couplets, distinctness of lithologic boundaries, and synsedimentary contorted bedding. Using a scheme simplified from Ingram (1954), thick bedded refers to couplets thicker than 30 cm, medium bedded to couplets 10–30 cm thick, and thin bedded to couplets thinner than 10 cm. Laminae are thinner than 1 cm. Because of the limited space on the VCD form for recording sedimentary structures, we combined the repeated grading that generally characterizes couplets of sand (or silt) and mud with the symbols for bed thickness. Therefore, unless otherwise indicated in the "Description" column, sand-mud and silt-mud couplets represented by any of the bed-thickness symbols have sharp bases and are graded throughout.

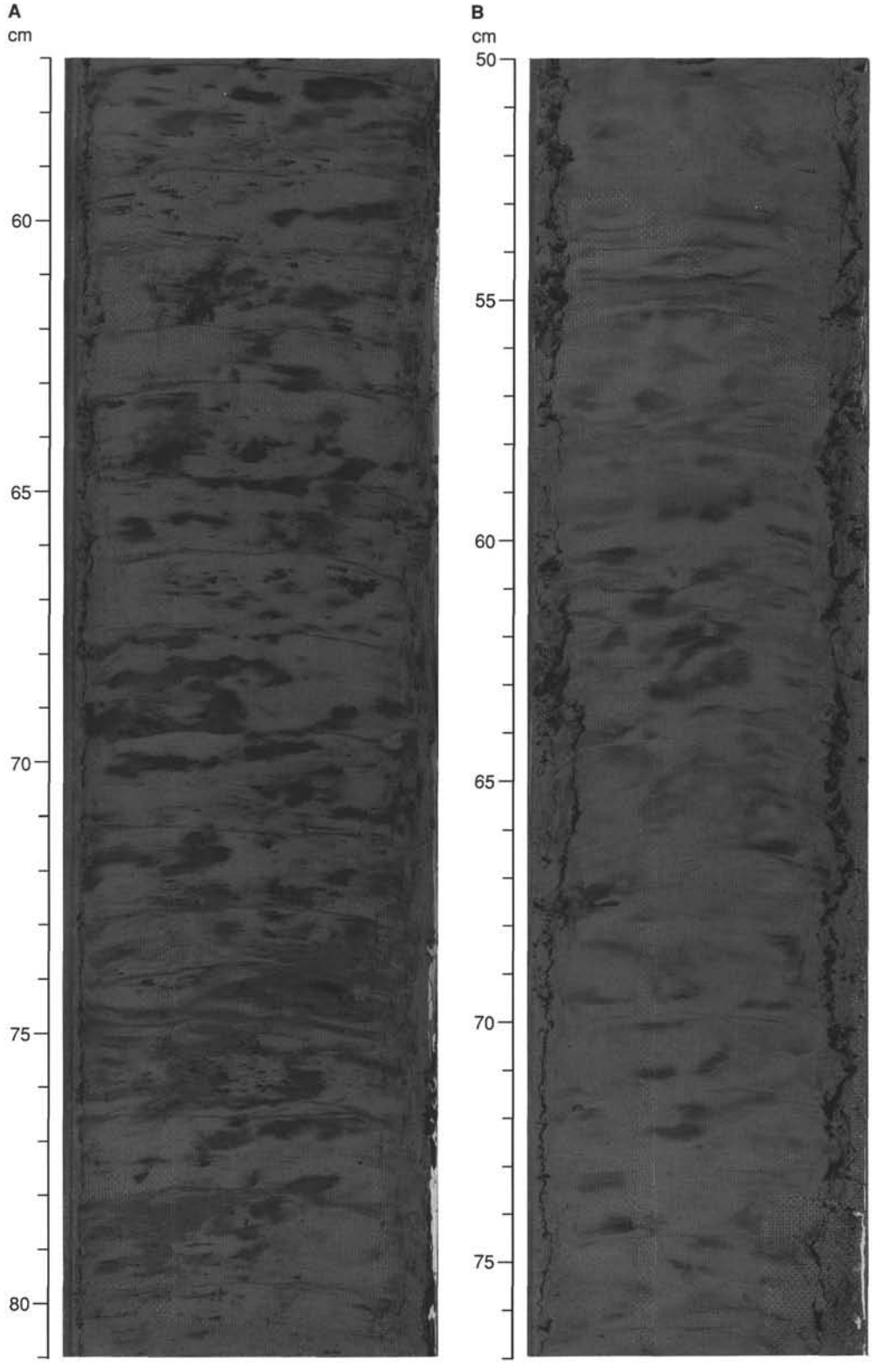

Figure 3. Examples of drilling biscuits formed during XCB coring. **A.** Very thin black laminae at 1- to 2-cm spacing mark boundaries of drilling biscuits in silty clay formed as a result of rotation during XCB coring. Offset of distinctive black burrow mottles helps define the extent of disruption (interval 155-938A-16X-3, 57–81 cm). **B.** Drilling biscuits of variable thickness in silty clay sediment disrupted during XCB coring; biscuit boundaries are marked by less distinct laminae. The threaded or irregular sawtooth edges of the core are also typical of biscuit formations (interval 155-938A-16X-1, 50–77 cm).

2. The central vertical window is reserved for information on grading types, the locations of fining-upward and coarsening-upward sequences that involve a number of beds, and the nature of the bases of beds (e.g., basal scours). Other symbols that normally would be placed in the right window can appear in this window if additional space is needed to show all important structures.
3. The right vertical window contains symbols for sedimentary structures (e.g., lamination, fluid-escape features, burrowing intensity, scours) and other components of special interest in the sediments (e.g., concretions, plant debris, microfaults). Thin solid or dashed lines that extend across all three vertical windows can reflect either color or lithologic contrasts (dashed where gradational).

Deformation and disturbance of sediment that clearly resulted from the coring process are illustrated in the "Drilling Disturbance" column, using symbols shown in Figure 2. Blank regions indicate the absence of coring disturbance. Categories of coring disturbance are distinguished in the following manner: slightly deformed = bedding contacts are slightly bent; moderately deformed = bedding contacts are extremely bowed, but not disrupted; highly deformed = bedding is completely disrupted, with local diapir-like or flow structures; soupy = water-saturated intervals that have lost all aspects of original bedding. Both highly deformed and soupy intervals can result from "flow-in" of sediment during piston coring, caused by incomplete strokes of the corer.

"Drilling biscuits" are rotated core segments and are common in sediment recovered with the extended core barrel (XCB) during Leg 155. In clay and silty clay sequences, the biscuits are recognized as intervals, generally 1 to 10 cm long, separated by thin to thick (generally 1–2 mm, thinnest near the center of the core) black pseudo-laminae that apparently consist of injected drilling slurry. The character and size of both the biscuits and the laminae varies with lithology and with the strength of the sediment where the lithology is similar. In silty clay with extensive bioturbation, the biscuits are recognized by linear truncations of the normally highly irregular patterns of burrows and mottles against thin (≤1 mm), flat, dark laminae (Fig. 3A). In some sections, the biscuit laminae are much less pronounced and, where burrows are smaller or indistinct, the core deformation may not be identified with confidence unless accompanied by other forms of core disruption that result from XCB use. One such character is the chewed up (sawtooth) edge of the core that forms when the outer part of the sediment sticks to the liner and separates from the center part of the core (Fig. 3B).

Some biscuits show internal deformation that includes shearing of tilted laminae to form sigmoidal or wedge-like patterns (14–18 cm in Fig. 4). Where biscuits disrupt sediment that was folded or tilted in the subsurface, "chevron" patterns with variable dips of laminae or color bands result (e.g., Fig. 4; Fig. 9B of "Site 932" chapter, this volume). Where curved or irregularly folded bedding is broken by the formation of biscuits, the resulting pattern is more complex and resembles the surface of a planar diagonal cut through a tree branch. This more complex pattern is termed "wood-grain" structure in the detailed section-by-section core description forms (e.g., Fig. 9 of "Site 932" chapter, Fig. 23 of "Site 941" chapter, Fig. 12 of "Site 944" chapter, and Fig. 11B of "Site 946" chapter, this volume). In some intervals, the crests of small folds with horizontal axial planes appear aligned along the center line of the core section indicating that at least some of the deformation is induced by rotary drilling (e.g., 55–85 cm in Fig. 10 of "Site 933" chapter, and Fig. 9 of "Site 943" chapter, this volume).

Coring deformation by the XCB corer tends to disrupt primary sedimentary structures, especially within sand and silt units and makes determination of depositional trends or processes difficult. In some cases, accurate tabulation of the number of beds and laminae is difficult because the silt and sand grains have been smeared or

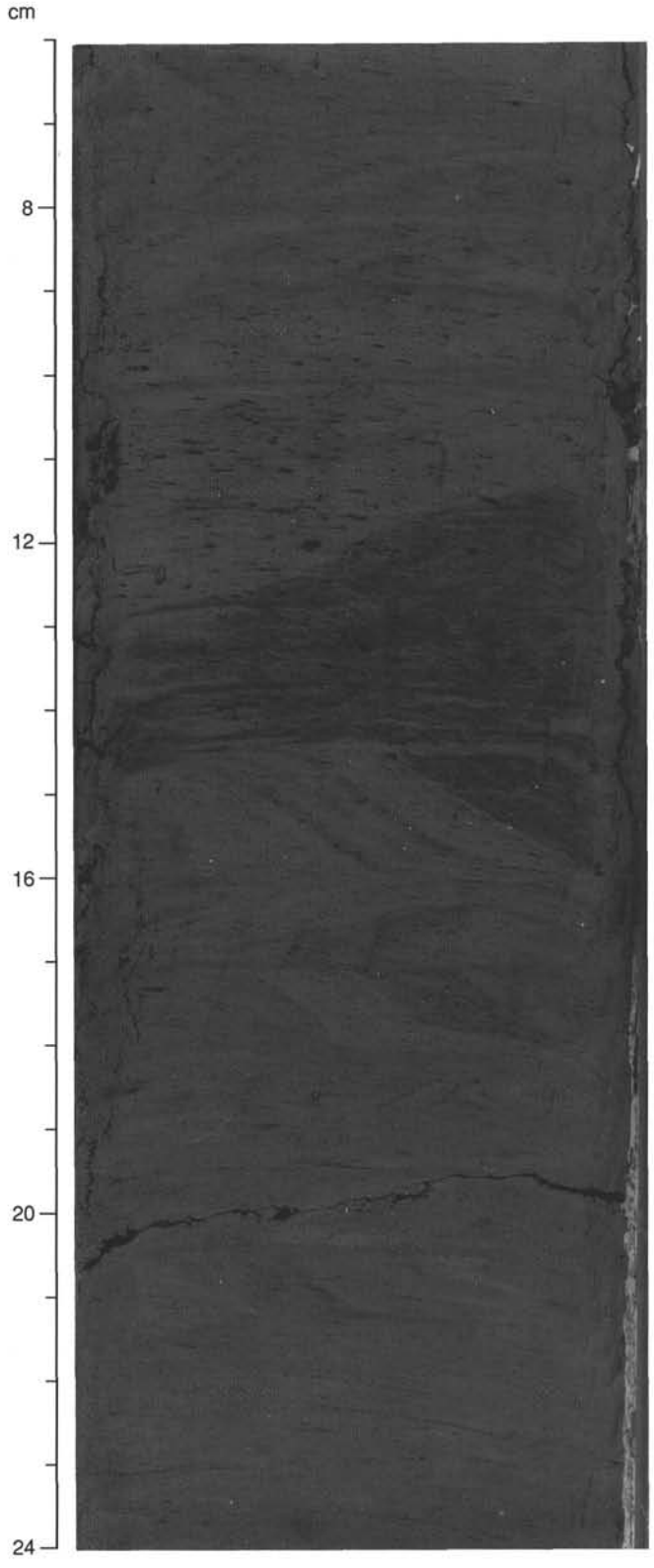

Figure 4. Drilling biscuits approximately 1 cm thick in silty clay, separated by thin black pseudo-laminae of drilling slurry. The variably tilted and folded color bands within the biscuits are thought to reflect primary dips in tilted or folded mass-transport deposits and the formation of biscuits results in chevron patterns and "wood-grain" texture (interval 155-936A-19X-6, 6–24 cm).

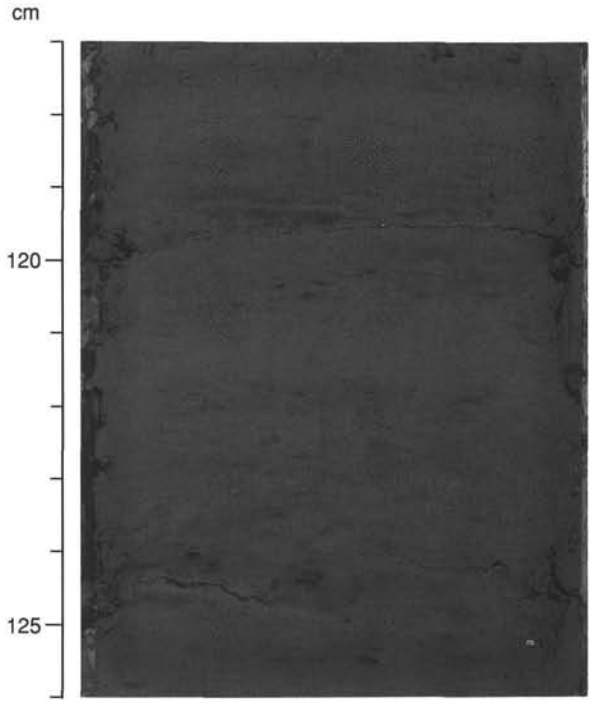

Figure 5. Silt laminae (e.g., 119.5 cm and 124.5 cm) disrupted by XCB coring so that only discontinuous remnants of original laminae remain (interval 155-938A-16X-5, 117–126 cm).

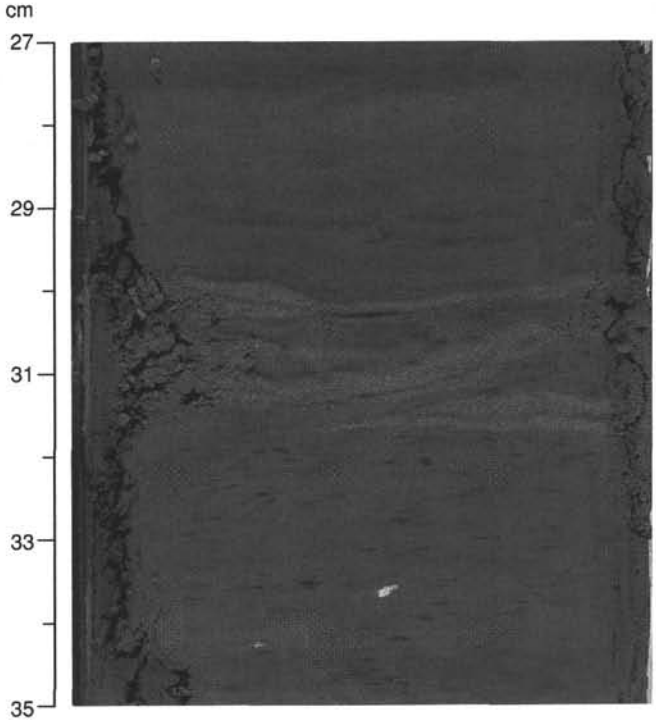

Figure 6. Silt lamina disrupted during XCB coring (30–31.5 cm); one part of the lamina has been rotated over the other (interval 155-938A-22X-4, 27–35 cm).

streaked into discontinuous, irregularly shaped blebs (119–120 and 124–125 cm in Fig. 5). If a bed has a distinctive internal structure, it might be possible to recognize that segments have been truncated and repeated as a result of rotation (Fig. 6). In some thin-bedded silt sequences, the XCB deformation is recognized through the formation of "anvil" structures, in which the coarser sediment is forced into the underlying silty clay (Fig. 7).

Expansion of methane gas during core recovery disrupted the sediment in many of the Leg 155 cores. The expansion effects are more extensive within beds and laminae of silt and fine sand, resulting in widespread destruction of primary sedimentary structures (35–52 cm in Fig. 8). In addition, these coarser-grained layers were commonly thinned by sediment entrainment with the escaping gas. Some sediment was lost from the core sections as a result of extrusion through holes drilled in the liner to vent the gas (Fig. 9). This sediment loss, combined with displacement of intervals of more consolidated clayey sediment along the core liner as gas pressure was released, resulted in as much as 60 cm of void space within a 150-cm core section. Only gas voids greater than 20 cm in length are documented in the core descriptions in this volume; however, the whole-core photographs record the full extent of disruption of the cores, including voids (e.g., Cores 930B-14X, 933A-4H, 935A-3H, 935A-6H). In addition, the detailed section-by-section paper core description forms can be obtained from ODP.

Samples taken for shipboard analysis are indicated in the "Samples" column by the following codes: D = XRD sample, I = interstitial water sample, M = micropaleontology sample, P = physical properties sample, S = smear slide, T = thin section, C = carbon analysis (organic and carbonate carbon), X = paleomagnetic sample, W = whole-round sample. Generally, one or two samples were routinely taken for XRD analysis from each core in the "A" hole at each site. Sufficient carbonate samples (generally 1–2 per core) were taken to characterize sedimentary units and calibrate carbonate content against color measured by spectrophotometer (see below).

The hue and value/chroma attributes of color were recorded in the "Color" column based on visual comparisons with Munsell Soil Color Charts (1975). The sediment colors observed in most of the Leg 155 cores are ephemeral, and after several hours of exposure to the atmosphere the sediment turns a nearly uniform dark grayish brown (2.5Y 4/2) as a result of oxidation of labile iron-bearing minerals (e.g., hydrotroilite, see "Introduction" chapter, this volume). The coloration seen during shipboard core description is permanently recorded on whole-core color transparencies available from ODP.

The lithologic description in each of the computer-generated core description forms consists of three parts:

1. A heading that lists all the major sediment lithologies in the core.
2. A heading for minor lithologies.
3. A more detailed description of the sediments, including color, composition, sedimentary structures, trace fossils identified, and other notable characteristics.

Descriptions and locations of thin, interbedded, or minor lithologies that could not be depicted in the "Graphic Lithology" column are presented where space permits. Many of the graded beds recovered from the Amazon Fan contain "Bouma sequences," which are sequences of sedimentary structures similar to those recorded in graded beds of Alpine flysch by Bouma (1962). To simplify descriptions, such Bouma sequences are noted in some cases by a code, such as T_{bde}, that consists of an uppercase T (for "turbidite") followed by lowercase letters that summarize the order and identity of internal divisions within the Bouma sequence, (e.g., a = massive or graded division, b = parallel laminated sand or silt division, c = ripple cross-laminated division (may be overprinted by convolution), d = muddy parallel laminated division, and e = essentially homogeneous mud division, possibly graded). Hemipelagic muds (containing a pelagic biogenic component and burrows) are described separately.

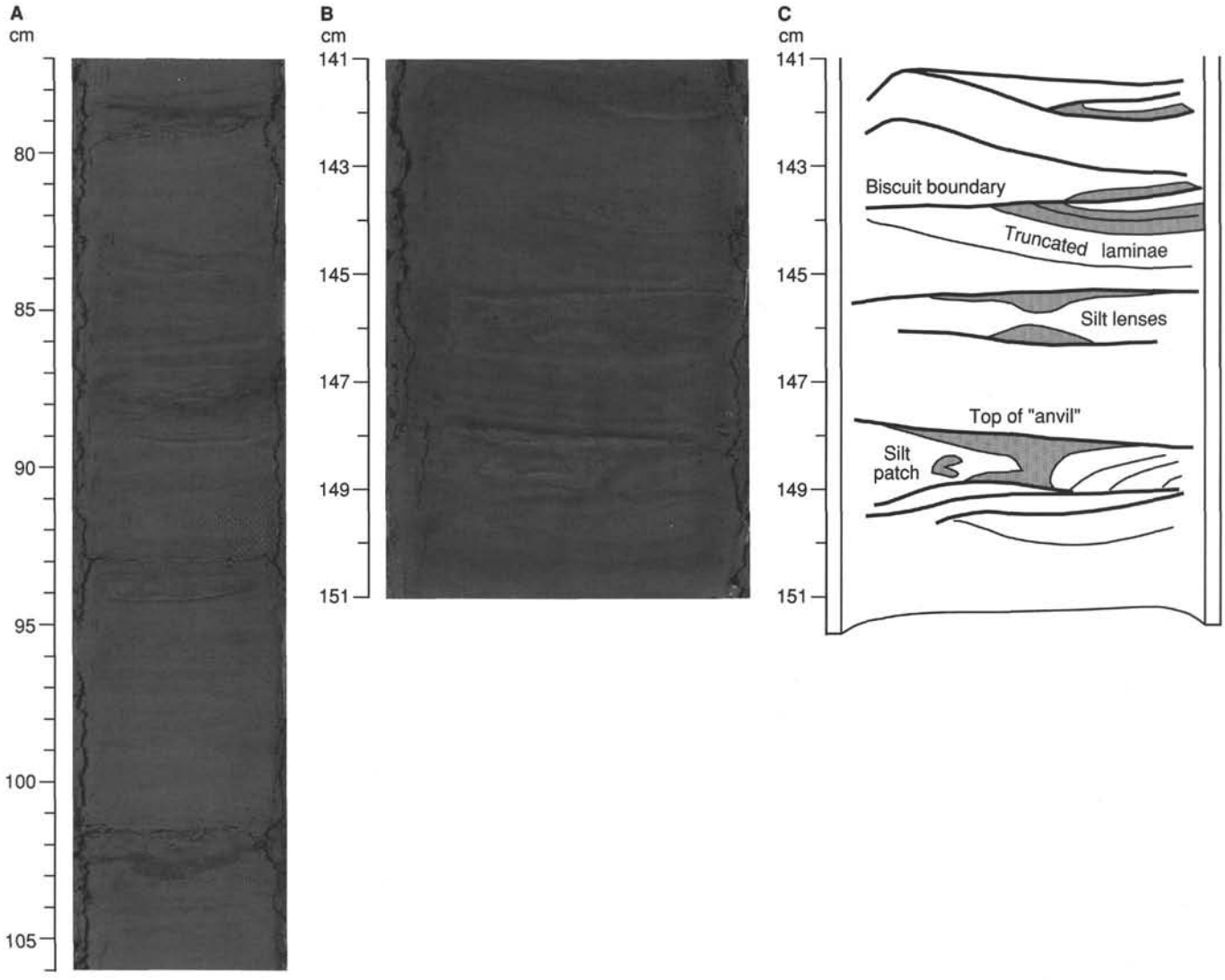

Figure 7. **A.** Anvil structures in silt beds disrupted by XCB coring (interval 155-940A-21X-3, 77–106 cm). **B.** Close-up of anvil structures (145–146 cm and 148–149 cm) showing deformation of underlying silty clay (interval 155-940A-21X-3, 141–151 cm). **C.** Line drawing interpretation of (B); the top of the anvil is all that remains to indicate the original level of the disrupted silt bed.

Procedures for Classification of Sediments

The sediment classification scheme used during Leg 155 is descriptive. Composition and texture are the only criteria used to define lithologies. Genetic terms such as pelagic, hemipelagic, turbidite, debris flow do not appear in this classification. The term "clay" is used for clay minerals and other siliciclastic material less than 4 μm in size. Biogenic components are not described in textural terms. Thus, a sediment with 55% sand-sized foraminifers and 45% siliciclastic clay is called a foraminifer clay, not a foraminifer clayey sand. The following rules apply.

1. The principal name is determined by the component or group of components (e.g., total biogenic carbonate) that compose(s) at least 60% of the sediment or rock, except for subequal mixtures of biogenic and nonbiogenic material. The most common principal names are as follows:
   a. Nonbiogenic: If the total of a nonbiogenic component is greater than 60%, the main name is determined by the relative proportions of sand, silt, and clay sizes when plotted on a modified Shepard (1954) classification diagram (Fig. 10). Examples of nonbiogenic principal names are clay, silt, silty clay, or sand.
   b. Biogenic: If the total of biogenic components is greater than 60%, the principal name is "ooze." No oozes were recovered on Leg 155.
   c. Mixed sediments: In mixtures of biogenic and nonbiogenic material where the biogenic content is 30%–60%, the principal name consists of two parts: (i) the name of the major fossil(s), hyphenated if necessary with the least common fossil listed first, followed by (ii) the textural name appropriate for the siliciclastic components (Fig. 10). For example, if nannofossils form 30%–60% of a sediment that contains nothing else but clay, then the name is nannofossil clay even if nannofossils are somewhat more abundant than clay. In cases of subequal mixtures of calcareous microfossils, the modifiers "calcareous" or "carbonate-rich" can be used in the classification instead of microfossil names.

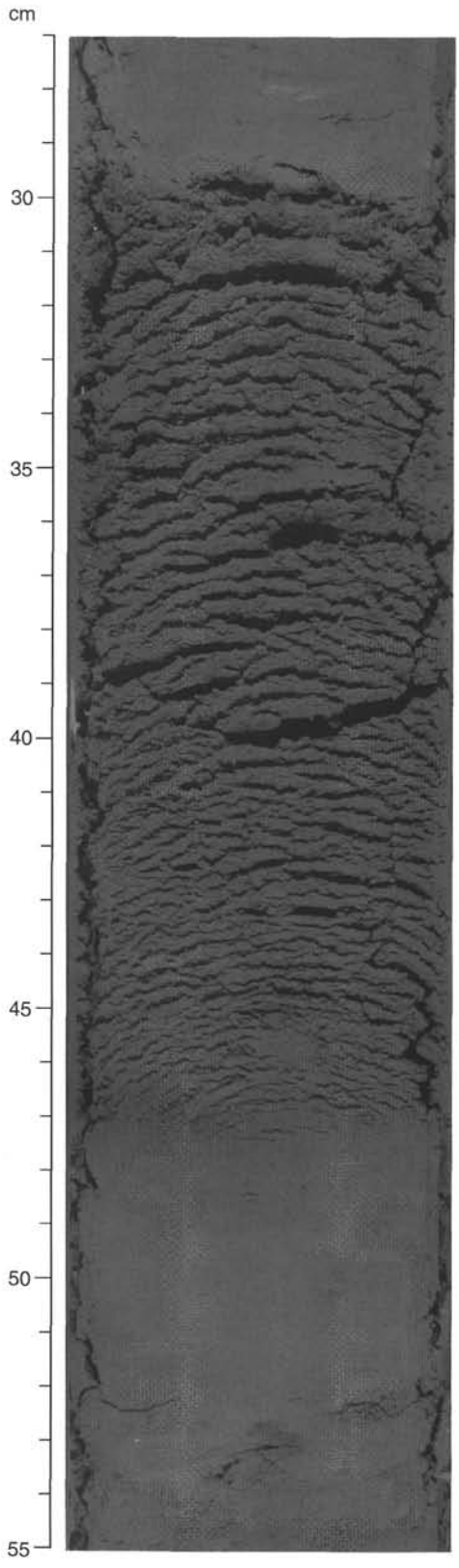

Figure 8. Silt bed disrupted by gas expansion (interval 155-931B-15X-2, 27–55 cm).

2. When a component comprises 10%–30% of the sediment, it qualifies for minor modifier status and is hyphenated with the word "rich" (e.g., nannofossil-rich clay).
3. When a component comprises only 5% to 10% of the sediment and thus would otherwise not form part of the sediment name (e.g., plant material, granules, sand), it can be indicated with a minor modifier that consists of the component name hyphenated with the word "bearing." Examples are plant-bearing clay and sand-bearing silty clay. This is an optional modifier.
4. The most abundant accessory component appears closest to the principal name. Major and minor modifiers are listed in order of decreasing abundance to the left of the principal name.

Example: foraminifer-rich nannofossil clay
(10%) (35%) (55%)

Graphic Sedimentological Columns

Graphic sedimentological columns are presented in the "Lithostratigraphy" section of each site chapter and in the back-pocket foldout. The columns show grain-size variation (width of columns), bed thickness where beds are thick enough for their bases and tops to be shown separately, and sedimentary structures. Normally, all laminae and beds of silt and sand are shown in the column, so that these are true bed-by-bed sections; however, the minimum bed thickness that can be represented is 10 cm. For intervals with more than about 20 laminae and/or beds per 1.5-m section (e.g., Fig. 9 at 315–335 mbsf in the "Site 935" chapter, this volume), the graphic column contains closely spaced lines that are fewer in number than the actual number of laminae and beds.

In some cases, symbols used in the graphic sedimentological columns and the back-pocket foldout are different or additional to those used on the computer-generated VCD forms. To avoid any confusion, a key to the full set of symbols used on the graphic sedimentological columns is presented in Figure 11. The graphic columns for those cores with greater than 100% recovery were compressed to account for gas-induced expansion by first subtracting large voids present in core sections and then, using graphics software, by uniformly scaling the remaining length to the length of the cored interval. Void subtraction, but no compression, was applied to cores for which the ODP official recovery was less than 100%, even though many of these cores also showed evidence for pervasive gas expansion. Arrows indicate the boundaries of lithostratigraphic units and subunits. The plotted depths of both these lithostratigraphic boundaries and other sedimentological features differ slightly from official ODP depths because of the compression applied to the primary data to fit all recovered sediments into the cored interval.

X-ray Diffraction

Relative abundances of the main silicate and carbonate minerals were determined semi-quantitatively using a Philips™ model PW-1729 X-ray diffractometer with Cu Kα radiation (Ni filter). Instrument conditions were as follows: 40 kV, 20 mA, goniometer scan from 2° to 70° 2θ for bulk samples and 2° to 35° for <2-µm samples, step size 0.01° 2θ, count time 0.5 s, peak intensities converted to values appropriate for a fixed slit width.

Each bulk sediment sample was freeze-dried and crushed. Two subsamples were taken. For some samples, one subsample was heated to 550°C for 2 hr to collapse kaolinite peaks (e.g., at 0.716 nm). Both subsamples were then packed with random orientation into separate aluminum sample holders. Samples for clay-mineral analysis were put into a 50-ml beaker with 25 ml of distilled water and Calgon solution, and placed in an ultrasonic vibrator for approximately 1 min. The resultant suspension was centrifuged for 5 min at 1000 rpm to settle the particles coarser than 2 µm. The material that remained

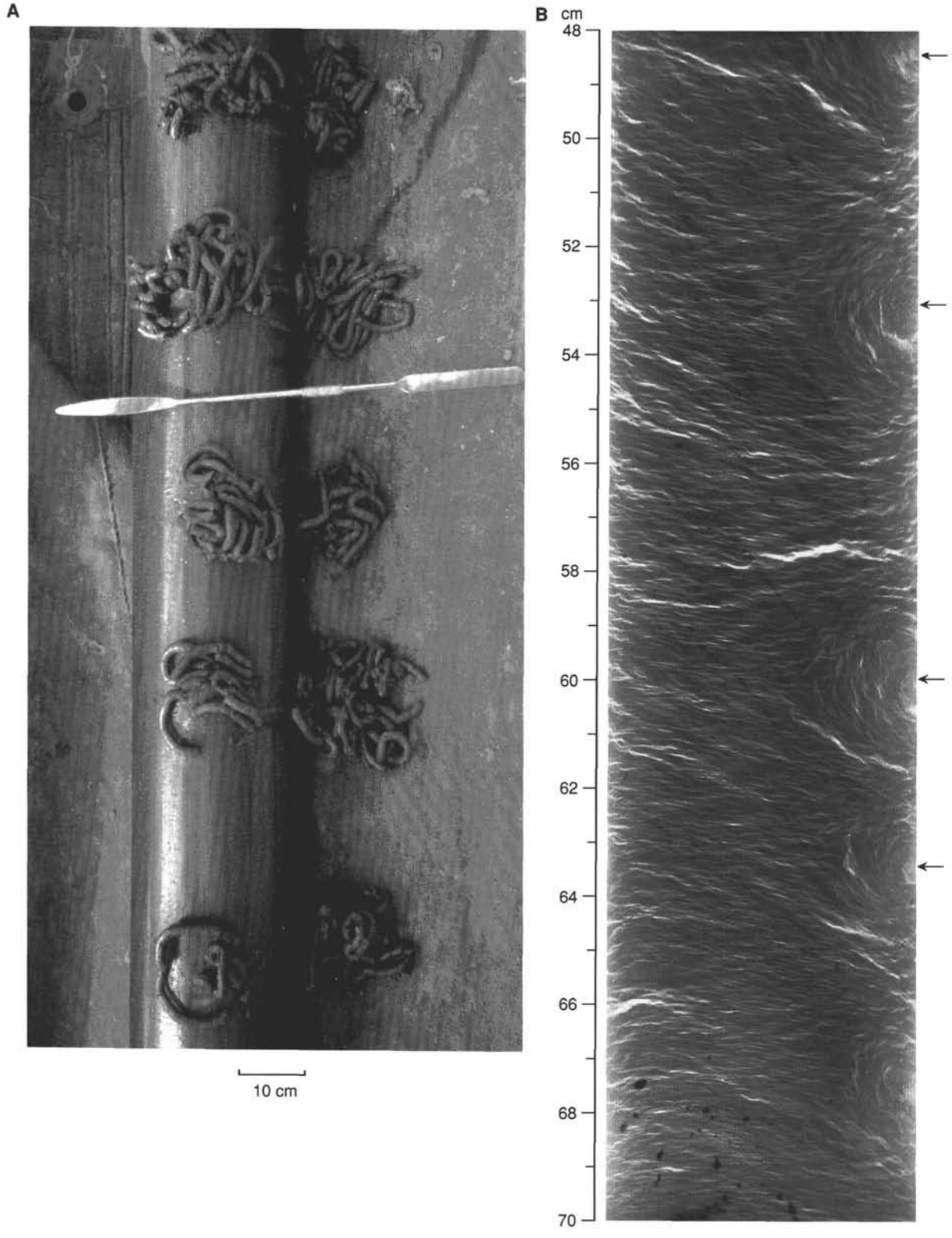

Figure 9. **A.** Mud worms formed by sediment extruded through holes drilled in the core liner to vent methane gas. **B.** X-radiograph of core interval disrupted by gas showing expansion cracks. Sediment fractured horizontally within the liner, even though the bedding is steeply dipping (faint black laminae). Localized deformation of sediment around hole drilled in the liner to vent gas (noted by arrows) is also clearly visible.

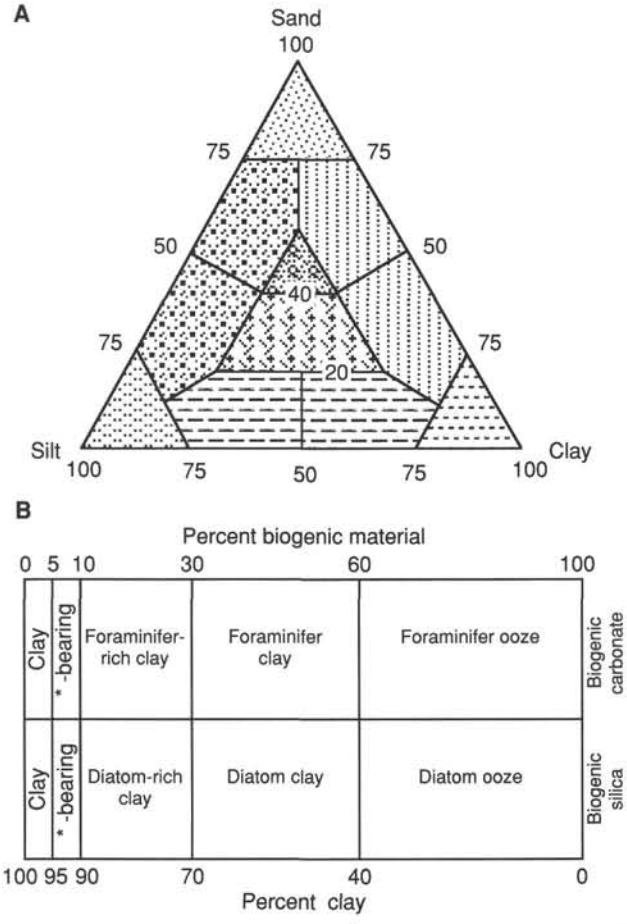

Figure 10. **A.** Textural classification scheme for siliciclastic sediments, modified from Shepard (1954) by subdivision of the central triangular field into muddy sand and sandy mud. The sand-, silt-, and clay-sized fractions are defined using the Wentworth (1922) grade scale. The patterns used on the Shepard triangle are explained in Figure 1. **B.** Classification for mixed siliciclastic and biogenic sediments. Names for microfossil components and the siliciclastic fraction shown in the table are examples only (i.e., place-holders), and can be replaced by any valid textural name (for siliciclastic fraction) or microfossil name. Examples are foraminifer silty clay and nannofossil-rich sandy mud. The asterisks in the scheme for biogenic-clastic mixtures indicate an unusual component, such as plant debris, present in amounts of 5%–10%; use of the "-bearing" category is optional.

Table 1. Positions of diagnostic peaks used for the identification of minerals in X-ray diffractograms, and for quantification of peak intensities.

Mineral name	Peak position (°2θ)	d-spacing (nm)
Hornblende	10.30–10.70	0.859–0.827
Augite	29.70–30.00	0.300–0.298
Calcite	29.25–29.60	0.304–0.301
Kaolinite	12.20–12.60	0.725–0.702
K-feldspar	27.35–27.79	0.326–0.321
Illite (+ mica)	8.70–8.87	1.010–0.996
Plagioclase	27.80–28.15	0.321–0.316
Quartz	26.45–26.95	0.337–0.331
Smectite	6.00–6.80	1.424–1.260

in suspension was removed from the top 1 cm of the centrifuge tube with an eyedropper and dropped onto two small glass slides to make oriented clay mounts. After air drying, the first mount was run untreated, then glycolated in a closed container for 18 hr and run again. The second mount was heat-treated at 550°C for 1 hr prior to running. Heat treatment and glycolation allow distinction of smectite and kaolinite (Moore and Reynolds, 1989). In some cases, heating of glass-mounted subsamples resulted in peeling of the sample from the glass surface, and these subsamples could not be analyzed.

A computer analysis package prepared by the instrument manufacturer (Philips Analytical, 1990) was used to select diffraction peaks, and to quantify the peak intensity, in counts above the baseline. The limits for maximum permissible tip and base widths were set at 1° and 2° 2θ for bulk samples, and 2° and 4° 2θ for clay-mineral runs. The wider peak window for clays was chosen to ensure that the peak-selection algorithm recognized the broad smectite peaks that characterize Leg 155 oriented clay-mineral mounts.

Minerals were identified by searching for diagnostic peaks in areas of the spectrum with minimum overlap (compare Cook et al., 1975). The locations of those peaks used for mineral recognition and semi-quantitative estimation of abundance are presented in Table 1. Each value of peak intensity above baseline was normalized by dividing its intensity by the intensity of the 0.334 nm quartz peak, for bulk samples, and the 0.720 nm kaolinite peak, for clay-mineral samples. These "relative" intensities are reported in the site chapters. Ratios and relative abundances reported in this volume are useful for general characterization of the sediments, but should not be viewed as precise quantitative data. The original diffractograms and the primary computer data files are available from ODP.

Spectrophotometry

Spectrophotometer readings of sediment color were routinely measured to establish semi-quantitative relationships between spec-

Figure 11. Key to symbols used in graphic sedimentological columns in each site chapter and the back-pocket foldout.

tral reflectance in distinctive wave bands and identified lithologies, in addition to providing a continuous stratigraphic record of color variations. The spectrophotometer readings were made with a Minolta CM-2002 Spectrophotometer after cleaning the surface of the archive half each core section. Measurement locations on each section were first covered with strips of very thin, transparent plastic film (food wrap) to avoid getting sediment on the lens of the instrument. Routine measurements were made at 20 cm, 60 cm, 100 cm, and 140 cm of each section, dependent on section length and the position of gas voids within the section. The measurement spacing was reduced to 5 or 10 cm for core intervals with distinct color variations or changes in lithology over short distances (i.e., <40 cm). Before obtaining measurements from each hole, the spectrophotometer was calibrated for white color reflectance by attaching a white calibration cap, which was covered with the same plastic wrap to prevent bias in the readings when compared to the sediment values. These white color calibrations were made to avoid variation in color readings dependent on the laboratory environment (temperature, humidity, and background light) and instrument deviations. White color readings were taken immediately before a core was measured in order to evaluate instrumental variations between measurements on different cores.

The spectrophotometer readings were recorded using the Spectrolog Program 3.0™ on a Macintosh personal computer. Each reading consists of 31 separate determinations that measure reflectance in 10-nm-wide spectral bands in the visible range between 400- and 700-nm wavelength. Reflectance in the wavelength band from 400 to 450 nm is not presented in site reports after Site 931 because we found that minor changes in the structure and placement of the plastic film on the split-core surface markedly affected reflectance values in this spectral range.

The initial use of the spectrophotometer at Site 930 showed that the reflectance never exceeded 35% at all wavelengths. Changes in the observed reflectance were dominated by very high variability of individual measurements (noise) that results from millimeter-scale changes in lithology and core condition (e.g., the presence of silt laminae or disseminated iron-monosulfide or the occurrence of gas partings; see Fig. 4 in the "Site 930" chapter, this volume). Thus, the shipboard interpretations of the spectrometer data concentrate on variations in the ratio of reflectance between particular wavelength bands. Based on the relationships between lithology and reflectance in distinct wavelength bands described above, it was possible to correlate deviations from the mean red/blue ratio of the reflectance data at each site to the lithologic units characterized from the recovered sediment. The results of the color reflectance measurements are summarized in Schneider et al. (this volume).

X-radiography

Both half-rounds and 1-cm-thick slabs of core sediment (in either stainless-steel or Plexiglas trays) were X-rayed using a Hewlett-Packard Faxitron™ X-ray unit, Model 43855A, and Kodak Industrex™ AA X-ray film in ready packs. ODP has modified the shipboard X-ray unit by attaching lead side arms that allow 150-cm-long core sections to be passed through the X-ray cabinet. Half-round sections were placed in an aluminum trough fabricated at Memorial University of Newfoundland; both the core and the trough were positioned between the X-ray source and the film. The trough is about 1 mm thick along its center line and about 1 cm thick beneath the edge of the core liner. The aluminum has the effect of compensating for the variable thickness of sediment in the split cores, thus balancing the intensity of the X-radiation that reaches the film under all parts of the half core and providing a more uniform exposure of the X-ray film. The automatic exposure capability of the Faxitron™ unit was inoperative throughout Leg 155, so manual exposure settings were used. We used a fixed potential of 45 kV and a film-selection setting of zero. By trial and error, it was determined that the most suitable exposure times were 3 min for half-round sections, 4 min for slabs taken in uncovered, 0.9-mm-thick stainless-steel trays, and 40 s for slabs in Plexiglas trays taken with the "Scripps sampler."

Preparation of Thin Sections of Mud and Petrographic Classification of Sand

Slices of soft mud were taken with a 40-cm^3 scoop, then gently transferred to a flat surface, and trimmed to even thickness with a thin wire. Samples were freeze-dried for about 12 hr to avoid excessive cracking, although thin microcracks still penetrated much of the freeze-dried sediment. The dried samples were impregnated with Epo-tek™ resin under vacuum, and then made into standard thin sections.

Thin sections of unconsolidated sand were made by pouring resin over loose grains in a plastic mold. Neither the apparent sand porosity nor the sorting in these thin sections is primary. Composition of sand samples was visually estimated at the microscope with the aid of the comparison charts of Terry and Chilingar (1955). Petrographic classification is based on the scheme of Folk (1980).

BIOSTRATIGRAPHY

Introduction

The biostratigraphic framework was based primarily on the Ericson zones (Ericson, 1961; Ericson et al., 1961; Ericson and Wollin, 1968). These ecostratigraphic zones in the tropical Atlantic Ocean were defined by the presence or absence of *Globorotalia menardii* and *Globorotalia tumida*. In the western equatorial Atlantic the Z/Y boundary has been regarded as approximately equivalent to the Holocene/Pleistocene boundary (e.g., Ericson and Wollin, 1968; Damuth, 1977; Prell and Damuth, 1978). For the purpose of biostratigraphy during Leg 155, we have defined the Holocene/late Pleistocene boundary to be coeval with the Ericson Z/Y boundary or as the reappearance of *G. tumida*. Recent AMS ^{14}C dating has shown that *G. tumida* repopulated the Atlantic Ocean from the Indian Ocean 9,000 years ago, whereas *G. menardii* did not reoccur until 6,250 years ago (G. Jones, pers. comm., 1994). Previous studies show that in general in the Amazon Fan the Z/Y Zone boundary approximately correlates with a change in the type of sediment deposited, and is associated with the occurrence of an iron-rich crust. However, this crust is diachronous across the Amazon Fan and adjacent western equatorial Atlantic (McGeary and Damuth, 1973; Damuth, 1977; Damuth et al., 1988; see "Introduction" chapter, this volume). Recent high-resolution studies have also shown that on the Mississippi Fan, the Ericson Z/Y boundary was apparently not correlated with shifts in either sedimentology or sedimentation rates (Kolla and Perlmutter, 1993). Thus, changes in sedimentology and sedimentation rate are driven by other factors (e.g., sea level), whereas the shifts in abundance of planktonic foraminifers such as *G. menardii* and *G. tumida,* are driven by climate and surface water circulation changes (Pujol and Duprat, 1983; Pflaumann, 1986; Maslin, 1993). Direct correlation between sedimentological changes and changes in the faunal assemblage is not necessarily expected in high-resolution post-cruise studies of Leg 155 material.

A tripartite division of the Pleistocene has been used in the shipboard study of Leg 155 sediments. Following Harland et al. (1990), the boundary between late and middle Pleistocene is placed at the beginning of isotopic Substage 5e. The middle-early Pleistocene boundary is placed at the Matuyama-Brunhes magnetic polarity reversal. Two short geomagnetic features were used for regional correlations: the Lake Mungo Excursion at about 30 ka and the Blake Event at about 105 ka (Table 2; Fig. 12). The boundary between oxygen isotopic Stages 1 and 2, dated at 12 ka by SPECMAP (Imbrie et al., 1984; Prell et al., 1986; Martinson et al., 1987), is offset from the

Table 2. Age estimates of paleomagnetic boundaries and excursions.

Event	Age (Ma)	Reference
Lake Mungo	0.03	Mankinen and Dalrymple (1979)
Blake	0.1	Mankinen and Dalrymple (1979)
Brunhes/Matuyama	0.78	Cande and Kent (1992)
Jaramillo	0.984–1.049	Cande and Kent (1992)
Cobb Mountain	1.1	Mankinen et al. (1978)
Olduvai	1.757–1.983	Cande and Kent (1992)

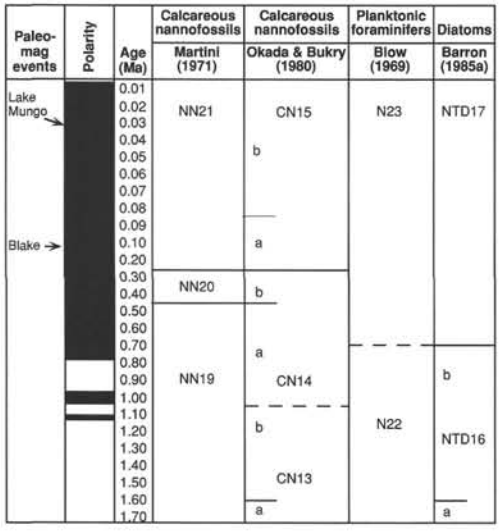

Figure 12. Correlation of Quaternary chronostratigraphy, biostratigraphy, and magnetostratigraphy used during Leg 155. Correlation of the magnetic polarity record, epoch boundaries, and planktonic foraminifers follows Cande and Kent (1992). Note time scale is not linear.

Holocene/Pleistocene boundary. The coarse resolution of the SPECMAP study implied that it did not take into account the high-resolution detail of the last deglaciation (e.g., two-step deglaciation found in the North Atlantic; Jansen and Veum, 1990).

Biostratigraphy

Preliminary age assignments were based on biostratigraphic analyses of calcareous nannofossils and planktonic foraminifers. Stratigraphic datums were defined by examination of the core-catcher samples and selected samples from critical core intervals. Spores, pollen, freshwater and marine diatoms, and phytoliths were used for paleoenvironmental analyses to support the interpretations of the marine calcareous microfossil assemblages.

Biostratigraphic efforts were usually concentrated on the deepest hole of a site, usually the A hole, similar to the method adopted on Leg 138 by Shipboard Scientific Party (1992). The abundance, preservation, and zonal assignment for each sample are recorded in the biostratigraphic site summary sheets.

Calcareous Nannofossils

Zonation and Datum Levels

During Leg 155, the zonal scheme of Bukry (1973, 1975, 1978), code numbered by Okada and Bukry (1980), was used and compared to the zonation of Martini (1971; Fig. 12). Modifications to improve the chronostratigraphic resolution of the Pleistocene by these standard nannofossil zonations were made by Gartner (1977), who proposed a higher resolution scheme, which subsequently was modified by, for example, Takayama and Sato (1987) and Raffi et al. (1993). The Pleistocene biostratigraphic events based on calcareous nannofossils are listed in Table 3.

Table 3. Calcareous nannofossil datums and estimated ages.

Event	Species	Zone (base)	Age (Ma)	Reference
B	acme *Emiliania huxleyi*	CN15b	0.085	1
B	*Emiliania huxleyi*	CN15a	0.26	1
T	*Pseudoemiliania lacunosa*	CN14b	0.46	1
	reappearance *medium Gephyrocapsa* spp.	CN14a?	1.03	2
T	large *Gephyrocapsa* spp.		1.24	2
B	large *Gephyrocapsa* spp.		1.46	2
T	*Helicopontosphaera sellii*		1.47	2
T	*Calcidiscus macintyrei*		1.60	2

Notes: B = base/first occurrence; T = top/last occurrence. References refer to (1) Thierstein et al., 1977; (2) Raffi et al., 1993.

Methods

The nannofossil assemblages were described directly from smear slides prepared from unprocessed sediment. The slides were prepared using standard methods, where a small amount of sediment is smeared onto a glass slide with a drop of water and dried on a hot plate and subsequently mounted with a drop of Norland Optical Adhesive on a cover glass. The slides were examined with a Zeiss Axioplan light microscope under crossed nicols and transmitted light at 1000×. A few critical identifications were confirmed by scanning electron microscopy immediately following the cruise.

The state of preservation of the nannofossil assemblages was characterized by the code system of the Leg 154 Shipboard Scientific Party (in press) as follows:

g = good (little or no evidence of dissolution and/or secondary overgrowth of calcite; diagnostic characters well preserved);
m = moderate (dissolution and/or secondary overgrowth; partially altered primary morphological characteristics; however, nearly all specimens can be identified at the species level);
p = poor (severe dissolution, fragmentation, and/or secondary overgrowth with primary features largely destroyed; many specimens cannot be identified at the species level and/or generic level).

The relative abundance of nannoplankton was recorded as follows:

a (abundant) = more than 100 specimens per field;
c (common) = 50–100 specimens per field;
f (few) = 10–50 specimens per field;
r (rare) = 1–10 specimens per field;
vr (very rare) = 1 specimen per 1–10 fields;
tr (trace) = <1 specimen per field;
b (barren) = no nannofossils present.

Planktonic Foraminifers

The Quaternary planktonic foraminifer datums are based on those of Pujol and Duprat (1983), Berggren et al. (1985), and Chaisson and Leckie (1993). In cores with abundant foraminifers, several methods can be used to define additional datums: localized appearances, climatically driven changes in abundance, and changes in coiling direction. These key faunal changes as well as additional climatically driven datums (Fig. 13; Table 4) are discussed below:

1. The first appearances of *Globigerinoides ruber* (pink) and *Globorotalia tumida flexuosa* have been shown to correlate

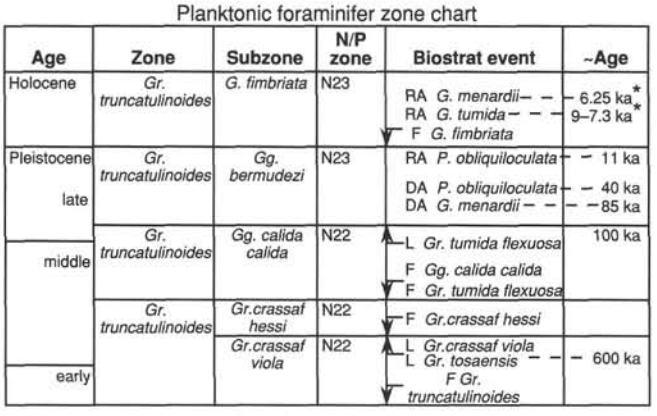

Figure 13. Planktonic foraminifer zone chart for Leg 155. * = AMS carbon dated by Jones et al. (pers. comm., 1994). RA = reappearance; F = first occurrence; DA = disappearance; L = last occurrence.

with oxygen Stages 16 and 18, respectively, in the eastern equatorial Atlantic (Pflaumann, 1986). These species also show a significant increase in abundance at oxygen isotope Stage 12 (Pflaumann, 1986). These abundance maxima are also reported in the southwest Atlantic by Pujol and Duprat (1983). Neither of these studies is in the western equatorial Atlantic, but the major tropical and subtropical current systems of the Atlantic link these areas. This suggests that first appearance and changes in abundance of these species could be coeval between the three areas, allowing them as a first approximation to be used as a datum for the equatorial western Atlantic.

2. In the eastern Atlantic *Globorotalia tumida flexuosa* is present in Pleistocene interglacials and peaks in abundance during oxygen isotope Stage 5, especially during Stage 5e (Pflaumann, 1986; Pflaumann, pers. comm., 1994). *Globorotalia hexagonus* is also abundant in interglacials.
3. The disappearance of *Pulleniatina obliquiloculata* within the Ericson Y Zone has been placed between 36 and 44 ka in the western tropical Atlantic, and has been defined as the $Y_{P.\ obliq.}$ datum within the Ericson zone system (Prell and Damuth, 1978). During Leg 155, the $Y_{P.\ obliq.}$ datum was assigned an age of 40 ka. *P. obliquiloculata* reappears at 11 ka based on AMS ^{14}C dating (G. Jones, pers. comm., 1994).
4. Ericson (1961), Ericson and Wollin (1968), and Ericson et al. (1961) defined ecostratigraphic zones in tropical Atlantic cores based on the presence and absences of *G. menardii* and *G. tumida*. These Ericson zones are climatically driven and compare well with oxygen isotope stratigraphy (Pflaumann, 1986). Therefore tentative correlations to isotope stages were attempted during the cruise.
5. The coiling direction of *G. tumida* has been shown to change with time (Pujol and Duprat, 1983). Predominant coiling direction during the Pleistocene is left, while during the Pliocene it is right. Sediments older than Pliocene or that have been significantly reworked exhibit mixed coiling directions.
6. The *G. truncatulinoides truncatulinoides* Zone was divided into one Holocene subzone (*Gr. fimbriata*) and four Pleistocene subzones (*Gg. bermudezi, Gg. calida calida, Gr. crassaformis hessi, Gr. crassaformis viola*) by Bolli and Saunders (1985).

Table 4. Planktonic foraminifer datums and estimated ages.

Event	Species	Oxygen isotopic stage[a]	Age/ka[b]	Ericson Zone[c]
AS	*Globorotalia menardii*	1	6.25	Z
AS	*Globorotalia tumida*	1/2[b]	9	Z–Y
RA	*Pulleniatina obliquiloculata*	1/2[b]	11	Y
DA	*Pulleniatina obliquiloculata*	3	40	$Y_{P.\ obliq.}$
LA	*Globorotalia tumida flexuosa*	5	85	X–Y
AS	*Globorotalia menardii*	5	85	X–Y
AS	*Globorotalia tumida*	5	85	X–Y
OA	*Globorotalia hexagonus*	5e	125	X
OA	*Globorotalia tumida flexuosa*	5e	125	X
AS	*Globorotalia menardii*	5/6[b]	130	X–W
AS	*Globorotalia tumida*	5/6[b]	130	X–W
AS	*Globorotalia menardii*	6	165	W–V
AS	*Globorotalia menardii*	11/12	425	V–U
AS	*Globigerinoides ruber* (pink)	12.2	430	
AS	*Globorotalia tumida flexuosa*	12.2	430	
AS	*Globorotalia menardii*	14/15	565	U–T
LO	*Globorotalia tosaensis*		600	
FA	*Globorotalia tumida flexuosa*	16	625	
FA	*Globigerinoides ruber* (pink)	18	760	
AS	*Globorotalia menardii*		920	T–S
AS	*Globorotalia menardii*		1400	S–R
AS	*Globorotalia menardii*		1700	R–Q
LO	*Globigerinoides fistulosus*		1700	

Notes: AS = abundance shift, RA = reappearance, DA = disappearance, LA = last appearance, OA = onset acme, LO = last occurrence, FA = first appearance.
[a]Oxygen isotopic stages and ages are based on SPECMAP (Imbrie et al., 1984; Prell et al., 1986, and Martinson et al., 1987).
[b]Glacial-interglacial fluctuations of *Globorotalia menardii* and *Globorotalia tumida* occur throughout the Pleistocene and are referred to as Ericson zones.
[c]Ericson et al. (1961), Ericson and Wollin (1968).

The definitions of oxygen isotopic stages and ages used in this study are those of SPECMAP reported by Imbrie et al. (1984), Prell et al. (1986), and Martinson et al. (1987).

Methods

Samples were prepared according to the degree of lithification. Unlithified calcareous clay was washed with tap water over a 63-µm mesh sieve. Samples with cohesive mud lumps were soaked in a weak Calgon solution, then gently stirred in a beaker with a magnetic stirrer, then washed with warm tap water over a 63-µm mesh sieve. Samples were air dried at 65°C in an oven. Preservation in the >150-µm-size fraction was estimated for all samples from a visual examination of the dried sample in the following categories:

g = good (>90% of the specimens unbroken; few signs of dissolution);
m = moderate (30%–90% of specimens broken or dissolved);
p = poor (<30% of specimens intact).

Planktonic foraminifer abundances were quantified for key species according to the following:

a = abundant (>30%);
c = common (15%–30%);
f = few (3%–15%);
r = rare (<3%);
b = barren.

The species were identified following the taxonomy of Bé (1977) and Bolli and Saunders (1985).

Diatoms

Zonation and Datum Levels

The Quaternary diatom zonation of Barron (1985a, 1985b) was used. The majority of markers in this zonation have been directly calibrated to magnetostratigraphy (Burckle, 1977; Burckle et al, 1982; Barron, 1985b). The species events and their assigned age estimates are listed in Table 5.

Table 5. Diatom and silicoflagellate datums and age estimates.

Event	Species	Zone* (base)	Age (Ma)
T	*Nitzschia reinholdii*	NTD17	0.65
T	*Mesocena quadrangula*		0.73
T	*Thalassiosira plicata*		0.8
T	*Nitzschia fossilis*		0.85
B	*Mesocena quadrangula*		0.91
T	*Rhizosolenia matuyamai*		0.94
B	*Rhizosolenia matuyamai*		1.1
T	*Rhizosolenia praebergonii* var. *robusta*	NTD16b	1.55
B	*Azpeitia barronii*		1.6
B	*Pseudoeunotia doliolus*	NTD16a	1.77

Notes: T = top/last occurrence, B = base/first occurrence. * Zonation of Barron (1985a,b).

Methods

Core-catcher samples and samples from critical core intervals were processed. Less than 0.5 gm of sample was placed in a 100-ml beaker with 10% HCl; 30% H_2O_2 was added to the beaker, and the sample was gently heated until the liquid became light yellow. The beaker was filled with distilled water and left to settle for 2 hr. The supernatant was decanted off and the sample was repeatedly washed until the liquid reached pH 6. Strewn slides of acid-cleaned material were mounted on glass slides with Hyrax mounting medium.

The diatom slides were examined with a Zeiss Axioplan microscope at 650× magnification; verification of individual species was made at 1250× when necessary. The criteria for distinguishing whole from broken diatoms followed Schrader and Gersonde (1978).

Abundance and preservation

Diatom abundance was quantified based on the number of specimens observed per field of view at 650× magnification and recorded as follows:

a = abundant (10 or more specimens per field of view);
c = common (five to 10 specimens per field of view);
f = few (one to five specimens per field of view);
r = rare (less than one specimen per field of view);
b = barren (no diatoms observed).

Preservation of diatoms was determined qualitatively and was recorded as follows:

g (good) = finely silicified forms present without alteration;
m (moderate) = finely silicified forms present with some alteration;
p (poor) = finely silicified forms fragmented and rare or absent; assemblages dominated by robust forms.

Phytoliths

Phytoliths, minute siliceous bodies precipitated in the epidermic cells of mainly grass and related savannah plants, are found in varying quantities in marine sediment. Previous studies of the occurrence of phytoliths in deep-sea cores include work by Kolbe (1955), Parmenter and Folger (1974), and Bukry (1980). The occurrence of phytoliths was recorded in the shipboard samples prepared for siliceous microfossil analyses.

Palynomorphs

Palynomorphs (spores, pollen, dinoflagellates, wood/structured plant debris) from core-catcher samples and selected core samples were examined microscopically.

Methods

The pollen and spore assemblage (usually from core-catcher samples) was described from smear slides prepared from processed sediment. The mechanical and chemical extraction techniques for 10–20 cm^3 of sediment consisted of decalcification with 10% HCl, followed by treatment with warm KOH solution. Sand and clay were removed with HF. After each chemical treatment the samples were washed and centrifuged for 4 min at 3000 rpm. The slides were prepared by smearing a fraction of the final residues onto a glass slide with a drop of water. The slide was then dried on a hot plate and subsequently mounted with glycerin jelly. The slides were examined with a Zeiss Axioplan light microscope under transmitted light at 400× magnification. Individual pollen and spore grains were identified to genera and family level (after Absy, 1979) where possible. Pollen and spore identification was usually done under oil immersion (1250× magnification).

Palynomorph Abundance, Preservation, and Zonation

The abundance of palynomorph groups (pollen, spore, dinoflagellates, wood/structured organic detritus) in the assemblage was based on the number of specimens observed per transect (40 mm) at 400× magnification as follows:

a = abundant (>10 specimens per 2 transects);
c = common (5–10 specimens per 2 transects);
f = few (2–4 specimen per 2 transects);
r = rare (<2 specimens per 2 transects);
b = barren (no specimens observed).

The preservation of palynomorphs was evaluated using the following criteria:

g = good (>75%, undamaged, i.e., not oxidized, broken, or folded);
m = moderate (25%–75% undamaged);
p = poor (<25% undamaged).

Reworked pollen and spores derived from older, previously deposited sediments generally show greater damage than fresh (non-reworked) pollen and spores.

Palynological zonations have been established for the Late Cenozoic of most of northern South America and are based on correlation with planktonic zones (Germeraad et al., 1968; Lorente, 1986; Muller et al., 1987). The most recent datum, and the only datum point referred to here, is found at the Pliocene/Pleistocene boundary and is defined by the abundance of *Alnipollenites verus* (*A. verus* is the fossil form of the modern *Alnus* and represents the establishment of North American temperate elements in South America). There are a number of important terrestrial pollen sequences associated with a cooler and possibly drier climate during the late Pleistocene. In the lowlands of the Amazon Basin few sites extend back to the late Pleistocene, and there remains no consensus as to the nature of vegetation present in the region during the Last Glacial Maximum (Colinvaux, 1989; Van der Hammen, 1974). The changes in relative abundance of key pollen and spore types (e.g., *Alnus, Cecropia,* Compositae, Cyperaceae [sedges], Rhizophoraceae [mangroves], Poaceae [grasses]) from Leg 155 sediments should contribute to our understanding of the response of continental vegetation to glacial/interglacial changes in climate. We also anticipate that variation in palynomorph abundance will be used to assist stratigraphic interpretation.

Identification of Reworked Sediments

An important component of biostratigraphy of the Amazon Fan is the identification of reworked sediment. The magnitude of the contri-

bution of reworked sediment is important as it affects the interpretation of age and origin of the sediment. When a whole sedimentary unit is reworked (e.g., a mass flow unit or debris flow), which is common in the Amazon Fan, then the taxa present in these sediments can be used to identify the age and the source of the reworked sediment. The criteria used to identify reworked sediment is given below. No shipboard attempt was made to quantify the reworked sedimentary components.

1. A high abundance of bathyal benthic foraminifers, which are highly adapted to sediment rich in organic matter. These are found in shelf sediments and down to a depth of 2,000 m off the coast of Brazil (van Morkhoven et al., 1986).
2. Iron-stained or heavily calcified benthic and planktonic foraminifers. This suggests that the foraminifers have been near the surface, after original deposition. This also may be a good indicator to distinguish reworked individual foraminifers from those in situ. This is an important distinction for stable isotope analysis.
3. Large broken siliceous and carbonate spicules (100–700 µm).
4. Macro and microscopic wood and organic matter fragments.
5. Shell fragments, ostracod shells, fish scales, echinoid shells, and spines.

PALEOMAGNETISM

Paleomagnetic studies on the *JOIDES Resolution* included measurement of natural remanent magnetization (NRM) in archive-half sections, before and after alternating field (AF) demagnetization up to 27 mT, and in discrete samples from the working half, before and after demagnetization of up to 50 mT. Measurements were also performed on discrete samples to obtain bulk susceptibility. Discrete sample volumes of 1, 5, and 7 cm^3 were used. The 1-cm^3 samples were intended solely for post-cruise analysis, to obtain high resolution results. The magnetic susceptibility was measured for each whole-core section as part of the multisensor track (MST) analyses. A standard 10-cm measurement interval was used for remanence measurements of the archive half core sections, except in the first core of some holes, where a 3-cm interval was employed. This smaller interval was chosen to provide more detail about diagenetic changes that often occur in the first few meters below the water-sediment interface. A measurement interval of 2 cm was employed for some core sections that contained records of secular variation or geomagnetic excursions. Both whole-core and discrete-sample susceptibility data were corrected before plotting to correct for downhole increases due to compaction.

Laboratory Instruments

A 2-G Enterprises (760R) superconducting magnetometer, with a 7.7-cm (3-in.) access diameter, was employed in the pass-through measurement of the archive half of the core sections. The system has an in-line, three-axis demagnetization system enclosed within a three-stage, mu-metal shield. The axial field within the demagnetization coils was continuously monitored and the shields were degaussed when this field exceeded 200 nT, which often happened when the ship changed heading. The pass-through magnetometer and demagnetization system is completely automated and controlled by a PC-AT-compatible computer. The three orthogonal sensing coils of the cryogenic magnetometer have a response interval of about 20 cm. Despite instrument noise arising from the rolling motion of the ship and the inherent magnetization of the core liner material, sediment magnetization intensities of 1 mA/m and above can be measured with a high degree of accuracy. The cryogenic magnetometer pass-through was also used to simultaneously measure remanence in up to seven spatially separated discrete samples from zones of particular interest using a discrete-sample measuring program.

Discrete-sample remanence measurements were also made using a Molspin Minispin spinner magnetometer in conjunction with a Schonstedt Alternating Field Demagnetizer (GSD-1). This system allows maximum demagnetization levels of 100 mT and 800°C, respectively. IRM acquisition was accomplished using an ASC Impulse Magnetizer (IM-10), which can generate transient DC fields of up to 1.2 T. A DTECH Partial Anhysteretic Remanent Magnetizer was used to impart ARMs at 100 mT AF in ambient DC fields of up to 1 mT.

The Kappabridge KLY-2 Magnetic Susceptibility System is used to measure AMS as an indicator of magnetic mineral alignment relating to paleocurrent direction analysis. This instrument measures discrete-sample susceptibilities in 15 different orientations and resolves the three-dimensional distribution of magnetic susceptibility values within the sample into vectors that define both the axis of maximum susceptibility (lineation) and the axis perpendicular to the maximum susceptibility plane (foliation). A Bartington Instruments magnetic susceptibility meter was employed for measurements of bulk susceptibility on discrete samples at the rate of one sample per core section. This instrument can produce a 0.1-mT AC magnetic field at either low (0.465 kHz) or high (4.65 kHz) frequency. A comparison of susceptibility at both frequencies helps resolve the relative contribution of hyper-fine superparamagnetic grains to the susceptibility signal. The susceptibilities of the whole-core sections were measured on another Bartington susceptometer, mounted on the multisensor track (MST) with a MS1/CX 80-mm whole-core sensor loop set at 0.465 kHz. The full width of the impulse response peak (at half maximum) for this instrument, which can be operated on two sensitivity scales, is less than 5 cm. Because no standards existed aboard ship for the Bartington systems, bulk susceptibility data reported in this volume are on a relative basis.

Ambient Field Environment

Before arrival at the first site, a three-component fluxgate magnetometer was used to investigate the magnetic environment of the laboratory space where the sample cores were likely to reside. Several locations where the ambient field exceeded 0.1 mT were detected. These included the core rack adjacent to the elevator (particularly the third shelf from the bottom) and the track of the cryogenic pass-through magnetometer system in the vicinity of the cryo-cooler cold head, which is mounted directly above the front access port of the magnetometer. An attempt was made to demagnetize the mu-metal shielding adjacent to the cold head unit, but no reduction in ambient field was achieved. Therefore, we minimized the time the core halves spent in this area and the core rack region, so as to mitigate the acquisition of viscous remanence prior to measurement. Later measurements during the cruise indicated that the field strength near the pass-through track bed diminished to <0.1 mT, probably due to a change in the heading of the ship.

Core Orientation

During advanced hydraulic piston corer (APC) drilling, core orientation was achieved with a Tensor orientation tool. This tool, which stabilizes after about 5 min at bottom, consists of a three-component fluxgate magnetometer and a three-component accelerometer attached to the core barrel, which record the drift of the hole and the orientation of the double line on the working half of the plastic core liner. By ODP convention, this double line defines the positive X-direction of the cores. Ten or more readings were taken at 30-s intervals over a 5- to 10-min interval, and average values were computed to achieve precise orientations. Testing had shown that standard deviations below 1° can be achieved from multiple declination readings.

Data from the Tensor tool was corrected for local magnetic variation before its use in the computation of remanence field directions and AMS vector orientations. Oriented discrete samples were taken from the working half cores by pressing sample cubes into the soft sediment. To minimize sediment deformation, a thin stainless steel spatula was used to cut into the more lithified sediment zones before insertion of the sample cubes.

Magnetostratigraphy

Because Leg 155 holes that did not encounter sediment older than middle Pleistocene, standard magnetostratigraphic dating based on reversal stratigraphy could not be employed. Instead we concentrated on locating polarity excursions and events within the Brunhes normal polarity chron that are thought to have more than regional occurrence. These include the Lake Mungo Excursion (~30 ka) and the Blake Event (~105 ka), which have been identified in widely dispersed sites (Stupavsky and Gravenor, 1984).

ORGANIC GEOCHEMISTRY

Geochemical analyses performed during Leg 155 included quantification of volatile hydrocarbons and other gases, determination of inorganic carbon, total carbon, nitrogen, and sulfur, and characterization of organic matter. These analyses were performed using methods previously published by Emeis and Kvenvolden (1986) and those detailed in the "Explanatory Notes" chapters from previous legs (Legs 150, 151, and 152). This work was performed as part of the routine safety procedures required by ODP (JOIDES PPSP, 1992) and to provide initial information on the composition of organic matter during the cruise.

Volatile Hydrocarbons and Other Gases

Volatile hydrocarbons and additional gases were routinely obtained from cores by headspace (HS) and vacutainer (VAC) sampling (Kvenvolden and McDonald, 1986). For HS, about 5 cm^3 of sediment was taken from the top of the section directly below the sampling site for interstitial water (IW). The sediment was extruded from the sampling tool into a 21.5-cm^3 glass vial, capped, and heated in the oven at 70°C for 30 min. After this, a subsample of the headspace gas was injected into both of the chromatographic instruments described below. The VAC method for gas collection was used to sample gas pockets and/or expansion voids observed through the core liner. A special sampling tool attached to a gas syringe was used to puncture the core liner and collect the gas into a pre-evacuated, septum-sealed glass tube, or vacutainer. A portion of the gas was then injected into the gas chromatographs according to the techniques described below. Both analyses yield concentrations of gases as a volume percent of total gas. The headspace sampling technique necessarily dilutes gases produced by heating the sample with air in the headspace of the sample container. Vacutainer sampling, on the other hand, attempts to directly sample gases measured in sediment pore space, and sample dilution by air is greatly reduced. Thus, measured headspace gas concentrations will be much lower than vacutainer concentrations, and a direct comparison between the two is not meaningful.

Five cm^3 of gas obtained from both collection methods was injected into a series 100/Model 211 Hach-Carle (HC) gas chromatograph to quantify low molecular weight hydrocarbons, C_1–C_3. Samples were introduced through a 1-cm^3 sample loop into a 0.32-cm × 1.8-m chromatographic column packed with 80% Poropak N and Poropak Q (80/100 mesh). Chromatographic separation was achieved under isothermal conditions (90°C), with helium as the carrier gas and detection by a flame ionization detector (FID). A Hewlett-Packard (HP) Chemstation was used to collect the data and calculate gas concentrations from peak areas and the response factors derived from daily calibrations using external standards. The concentrations of C_1–C_3 compounds, including methane (C_1), ethane (C_2), ethene (C_2=), and propane (C_3), were determined from each HS and VAC sample. Propene (C_3=) was not separated from its saturated counterpart, propane, so both of these compounds were reported together as propanes.

Because elevated C_2+C_3 hydrocarbon concentrations were not detected at any Leg 155 sites, no results from the Natural Gas Analyzer (NGA) are reported.

Inorganic Carbon

Inorganic carbon was determined using a Coulometer Model 5030 carbon dioxide analyzer. Approximately 10 mg of freeze-dried crushed sediment was acidified with 2N HCl to convert carbonate (CO_3^{2-}) to CO_2. The CO_2 was then introduced into the coulometer where it reacted with a solution of monoethanolamine, causing a fading of the color of the solution that was measured by a photodetector. A back titration current was applied to generate base and return the solution to its original color. The percentage of carbonate was calculated from the inorganic carbon (IC) content, simply assuming that all carbonate occurs as calcite as follows:

$$CaCO_3 = IC \times 8.33.$$

Other carbonate minerals, in particular siderite ($FeCO_3$), were detected by X-ray diffraction and may be present in many carbonate samples even though all inorganic carbon is reported as $CaCO_3$.

Elemental Analysis and Total Organic Carbon

Total nitrogen, carbon, sulfur, and hydrogen were determined using a Carlo Erba Model NA 1500 CHNS analyzer. About 5 mg of freeze-dried and crushed sediment was mixed with about 5 mg vanadium pentoxide (which serves as an oxidizer) in a tin boat. The sample was then combusted at 1000°C in an O_2-enriched atmosphere yielding mainly CO_2, SO_2, NO_2, and H_2. These products were swept by a helium flow into a column filled in layers with Cr_2O_3 as catalyst and splintered copper as reductant. This process reduced NO_2 to N_2. The CO_2, SO_2, H_2, and N_2 were then chromatographically separated and quantified by a thermal conductivity detector. After calibration against external standards, the concentration of carbon, nitrogen, and sulfur were reported as weight percentages of the sample. Total organic carbon (TOC) was calculated as the difference between total carbon (TC) and inorganic carbon (IC):

$$TOC = TC - IC.$$

Characterization of Organic Matter Type

The Delsi-Nermag Rock-Eval II Plus TOC pyrolysis system was used to characterize the type and maturity of the organic matter, as described by Espitalié et al. (1977). These analyses were performed using the remains of the samples prepared for elemental analysis. In this procedure about 100 mg of the freeze-dried whole sediment was first heated at 300°C for 3 min to release volatile hydrocarbons (S1). Further heating from 300°C to 550°C at 25°C/min caused the cracking of the kerogen and the release of macromolecular hydrocarbons (S2). Both the S1 and S2 parameters were measured by FID and were reported as milligrams per gram of sediment. In addition to S1 and S2, two other parameters were derived from the Rock-Eval analysis that help characterize sedimentary organic matter. The temperature at which a maximum release of hydrocarbons from breakdown of the kerogen occurs (T_{max}), and the quantity of CO_2 produced from the pyrolysis of organic matter between 300°C and 390°C (S3) were used to assess the thermal maturity of the organic matter. Hydrogen Index

[HI = (100 × S2)/TOC], and Oxygen Index [OI = (100 × S3)/TOC] were automatically calculated for each analyzed sample. Both indices are proportional to the amount of atomic hydrogen and oxygen, respectively, in organic matter and can be used to characterize its origin (e.g., Stein et al., 1989).

When time permitted, we also performed analyses with a Geofina Hydrocarbon Meter (GHM). This instrument employs a Varian 3400 series gas chromatograph, a programmable pyrolysis injector linked to two 25-m capillary columns and flame ionization detectors. S1, S2, and T_{max} parameters were obtained by the GHM technique and compared to those obtained from Rock-Eval analyses. In addition, the Production Index, PI = S2/(S1 + S2), and the Petroleum Potential or Pyrolyzed Carbon, PC = 0.083 × (S1 + S2), were determined from both Rock-Eval and GHM analyses to further estimate the thermal maturity of the sediment.

Solvent extractions were conducted on selected samples. These sediments were freeze-dried and crushed, combined with 5 ml *n*-hexane and placed in an ultrasonic bath for 20 min. After centrifugation and removal of the overlying solution, the extraction was repeated. The combined extracts were almost completely evaporated in a weak flow of nitrogen at a temperature of 40°C. A 1- to 8-µL volume of the resulting solution was injected into a Hewlett-Packard 5890 gas chromatograph, which was equipped with a HP Ultra 1 capillary column (50 m × 0.2 mm × 0.11 µm film thickness). Helium was used as carrier gas, and the separated hydrocarbons were identified and quantified based on injections of hydrocarbon standards. Carbon preference index (CPI) values of detected *n*-alkanes were calculated according to the method of Bray and Evans (1961).

INORGANIC GEOCHEMISTRY

Interstitial Water Sampling and Analyses

Shipboard interstitial water analyses were performed on 5- to 15-cm-long whole-round sections that were cut immediately after the core arrived on deck. For all routine shipboard analysis at each site, samples were generally taken from the bottom of Section 1 of the first core, from Section 5 of cores 2–5, and from each third core thereafter. For three sites (931, 939, and 944), an additional high-resolution suite of 5-cm-long whole-round samples was analyzed. Samples were taken from B or C holes at approximately 1.5-m intervals for the first two cores and at 3-m intervals through Core 5.

Interstitial waters were collected by applying pressure to the sediment using a titanium and stainless steel squeezer (Manheim and Sayles, 1974). Prior to squeezing, the surface of each sample was carefully scraped with a spatula to remove potentially contaminated exteriors. The sample was then placed into a titanium cylinder on top of a Whatman No. 1 filter that was previously rinsed in deionized water to remove processing acids. A second filter paper and a stainless steel piston were placed on top of the sample in the cylinder. Up to 40,000 pounds of pressure (approximately 4150 psi) was applied with a hydraulic press. The interstitial water was expressed out of the hydraulic press through a 0.45-µm Gelman polysulfone disposable filter into a plastic syringe attached to the bottom of the assembly. Samples were stored in plastic vials pending analysis. Aliquots for future shore-based analyses were placed in acid-washed plastic tubes and glass ampoules and heat-sealed.

Interstitial water samples were routinely analyzed for: salinity as total dissolved solids (g/kg) with a Goldberg optical hand-held refractometer; alkalinity and pH by Gran titration with a Brinkmann pH electrode and a Metrohm autotitrator; dissolved chloride concentration by titration; dissolved calcium, magnesium, potassium, and sulfate concentrations by ion chromatography on a Dionex DX-100; and silica, phosphate, and ammonium by spectrophotometric methods with a Milton Roy Spectronic 301 spectrophotometer. The analytical techniques described by Gieskes et al. (1991) were followed for all analyses. International Association of Physical Sciences Organizations (IAPSO) standard seawater was used for calibration. Reproducibility for these analyses is expressed as 1σ of the means for multiple determinations of IAPSO standard seawater. These values are <1.5% for alkalinity and chloride, <1% for calcium and magnesium, 4%–5% for silica, phosphate, and ammonium, <3% for potassium, and <4% for sulfate. The dissolved sodium concentration was determined using charge balance calculations where Σ (cation charge) = Σ (anion charge).

Iron and manganese concentrations were measured using flame atomic absorption spectrophotometry with a Varian Spectra AA-20 atomic absorption unit using an air-acetylene flame. For both analyses a 1-mL aliquot of pore-water was diluted with 3 mL of a 0.1N HCL with 1000 ppm La solution to prevent precipitation of iron oxyhydroxides. Samples and standards for iron were further diluted with distilled water as necessary to keep within the linear working range of the instrument. Standard solutions were made in a seawater matrix to match matrix composition to the samples and were also diluted 3× with 0.1N HCL and 1000 ppm La. The reproducibility of these techniques (expressed as 1σ of the means of multiple determinations of IAPSO standard seawater or other standard) is: 2%–3% for iron, and 3%–5% for manganese. Chemical data for interstitial waters are reported in molar units.

X-ray Fluorescence Analyses

Mud and sand samples from most sites were selected for X-ray fluorescence (XRF) analysis of major and trace elements. All analyses were performed on board using a fully automated wavelength dispersive spectrometer (Applied Research Laboratory 8420) employing a 3-kW rhodium target X-ray tube as the excitation source.

To cleanse samples of seawater and seawater salt, 20-cm^3 of sample were mixed with 150 mL of distilled water and placed in a sonic bath for 10 min. Approximately 15 mL of methanol was added, the slurry was centrifuged, and the rinse water poured off. Rinsed samples were dried at 110°C for at least 12 hr, and powdered in a tungsten carbide mill in a Spex shatterbox for approximately 1 min.

Major element determinations were performed on fused glass beads to reduce matrix effects and eliminate particle size effects. Prior to fusion, samples were combusted at 975°C for 4 hr. Beads were prepared by mixing 0.500 g of the sample powder with 6.00 g of lanthanum-doped lithium tetraborate flux, and fused in a platinum-gold crucible at 1030°C for 8 min. The molten glass was poured into Pt/Au molds and cooled using a modified Claisse Fluxer apparatus. To reduce necessary matrix corrections, care was taken to choose calibration standards that matched as closely as possible the expected composition of the samples. Trace element data were acquired on pressed powder pellets made by mixing 5 to 7 g of rock powder with 30 drops of polyvinyl alcohol binder, and pressing the mixture into an aluminum cap with 7 tons of pressure. For a more detailed explanation of XRF techniques, see the "Geochemistry" section in the "Explanatory Notes" chapter of Legs 111 (Becker, Sakai, et al., 1988) and 147 (Gillis, Mével, Allan, et al., 1993).

Calibration factors for all elements were determined on a wide range of rock and mineral standards. Analyses of standards run as unknowns are given in Tables 6 and 7. Operating conditions and estimates of precision and detection limits are reported in Table 8.

PHYSICAL PROPERTIES

Physical properties were measured on whole-round sections and undisturbed parts of split cores. Nondestructive, whole-core measurements of wet-bulk density, compressional-wave velocity, magnetic susceptibility, and natural gamma radiation were obtained using

Table 6. Major element analysis (wt%) of geochemical reference standards.

Standard	Type	SiO_2	TiO_2	Al_2O_3	$Fe_2O_3^*$	MnO	MgO	CaO	Na_2O	K_2O	P_2O_5	Total
AGV-1	Andesite	60.49	1.06	17.70	6.76	0.10	1.49	4.92	4.63	2.97	0.47	100.57
AII92-29-1	Basalt	50.52	1.71	15.73	10.66	0.18	7.59	11.15	3.50	0.18	0.15	101.37
BE-N	Alkali basalt	39.78	2.64	9.79	12.76	0.20	13.55	14.41	4.10	1.49	1.08	99.80
BIR-1	Basalt	47.78	0.94	15.35	11.22	0.17	9.66	13.32	2.31	0.05	0.04	100.84
BR	Basalt	40.10	2.67	9.93	13.11	0.20	13.79	14.18	3.75	1.47	1.03	100.23
DR-N	Diorite	53.99	1.06	18.09	9.55	0.22	4.46	7.02	3.95	1.77	0.24	100.36
G-2	Granite	69.64	0.49	15.63	2.65	0.04	0.78	1.90	4.84	4.53	0.15	100.64
JF-1	Feldspar	67.85	—	19.09	0.21	—	—	0.91	3.60	10.02	—	101.63
JF-2	Feldspar	65.51	—	19.20	0.19	—	0.08	0.12	2.47	13.01	0.01	100.60
JR-2	Rhyolite	77.41	0.06	13.04	0.80	0.12	—	0.53	4.28	4.54	—	100.63
K1919-1	Basalt	49.86	2.75	13.43	11.96	0.17	6.93	11.38	3.23	0.57	0.28	100.56
MAG-1	Marine mud	58.00	0.82	19.01	7.70	0.10	3.59	1.59	4.51	4.02	0.18	99.52
Mica-Fe		35.49	2.54	19.78	25.80	0.36	4.85	0.42	0.27	9.05	0.41	98.96
Mica-Mg		39.32	1.64	15.34	9.44	0.25	21.06	0.04	—	10.36	—	97.40
SCo-1	Shale	68.65	0.63	15.10	5.53	0.06	3.06	2.77	1.11	2.97	0.20	100.08
SDC-1	Schist	67.17	0.99	16.38	6.81	0.12	1.75	1.43	2.30	3.33	0.12	100.39
SO-2	Soil	60.97	1.56	17.60	8.92	0.11	1.01	3.05	2.97	3.32	0.80	100.31
SO-4	Soil	76.26	0.63	11.50	3.77	0.09	1.07	1.72	1.63	2.29	0.24	99.21
STM-1	Syenite	59.31	0.14	18.65	5.22	0.23	—	1.13	8.93	4.28	0.18	98.02

Notes: — = not detected. *Total iron reported as Fe_2O_3.

Table 7. Trace element analyses (ppm) of geochemical reference standards.

Standard	Type	Ba	Ce	Cr	Cu	Nb	Ni	Rb	Sr	V	Y	Zn	Zr
504B	Basalt	24	8	349	88	0	136	2	68	255	25	69	42
AGV-1	Andesite	1218	59	10	56	13	16	64	644	126	22	104	252
BHVO-1	Basalt	131	42	283	137	19	127	9	392	267	27	108	188
BIR-1	Basalt	29	3	373	130	0	165	2	115	302	21	80	12
BR-1	Basalt	1088	144	341	81	108	259	41	1318	231	27	159	276
DR-N	Gabbro	384	42	33	52	7	21	67	401	215	27	173	136
G-2	Granite	1883	162	8	13	9	2	171	467	52	7	89	331
GBM-1	Garnet	—	17	26	23	2	35	3	13	130	29	69	96
GH	Granite	40	43	2	5	86	—	390	10	—	90	60	162
JB-2	Basalt	219	9	27	228	2	16	7	168	513	25	117	48
JB-3	Basalt	243	21	59	201	1	41	15	393	332	29	105	99
JG-1A	Granodiorite	447	29	19	4	9	4	177	186	21	32	34	119
JGB-1	Gabbro	59	12	62	87	3	34	6	333	578	15	119	24
JR-1	Rhyolite	64	47	4	4	11	2	251	26	—	49	25	98
JR-2	Rhyolite	48	34	4	4	14	1	307	8	—	54	26	102
MAG-1	Marine mud	495	87	96	32	17	53	149	143	118	25	143	144
Mica-Fe		89	438	95	3	259	38	1457	6	109	—	1357	861
MRG-1	Gabbro	35	34	526	125	22	194	7	254	426	16	197	102
RGM-1	Rhyolite	798	42	4	9	7	2	153	106	17	26	31	244
SCo-1	Shale	570	52	56	25	12	24	112	164	65	26	105	184
SO-1	Soil	894	116	161	60	10	85	116	310	97	23	145	90
SO-2	Soil	1095	119	7	9	23	5	70	351	68	45	120	823
STM-1	Syenite	566	255	2	3	278	2	120	731	60	48	245	1381

Note: — = not detected.

Table 8. X-ray fluorescence operating conditions, analytical error estimates, and detection limits.

Oxide or element	Line	Crystal	Detector	Collimator	Peak angle (°2θ)	Background offset (°2θ)	Count time on peak (s)	Count time on background (s)	Analytical error (rel %)	Detection limit
SiO_2	K-alpha	PET	FPC	Medium	109.21		40		0.5	0.07
TiO_2	K-alpha	LIF200	FPC	Fine	86.14		40		2.6	0.01
Al_2O_3	K-alpha	PET	FPC	Medium	145.12		100		0.6	0.05
Fe_2O_3	K-alpha	LIF200	FPC	Fine	57.52		40		1.1	0.04
MnO	K-alpha	LIF200	FPC	Fine	62.97		100		6.5	0.007
MgO	K-alpha	TLAP	FPC	Medium	45.17	±0.80	150	150	1.5	0.08
CaO	K-alpha	LIF200	FPC	Medium	113.09		40		1.2	0.005
Na_2O	K-alpha	TLAP	FPC	Medium	54.10	–1.20	150	150	3.0	0.60
K_2O	K-alpha	LIF200	FPC	Medium	136.69		100		0.8	0.02
P_2O_5	K-alpha	GE111	FPC	Medium	141.04		100		9.8	0.02
Rh	K-alpha Compton	LIF200	Scint	Fine	18.58		60			
Nb	K-alpha	LIF200	Scint	Fine	21.40	+0.35	200	100	4.6	0.9
Zr	K-alpha	LIF200	Scint	Fine	22.55	–0.35	100	50	1.0	0.6
Y	K-alpha	LIF200	Scint	Fine	23.80	–0.40	100	50	3.0	1.0
Sr	K-alpha	LIF200	Scint	Fine	25.15	–0.40	100	50	0.9	0.6
Rb	K-alpha	LIF200	Scint	Fine	26.62	–0.60	100	50	0.7	1.0
Zn	K-alpha	LIF200	Scint	Fine	41.81	–0.55	100	50	1.0	2.5
Cu	K-alpha	LIF200	Scint	Fine	45.03	–0.55	100	50	4.8	1.4
Ni	K-alpha	LIF200	Scint	Fine	48.67	–0.60	100	50	2.3	1.2
Cr	K-alpha	LIF200	FPC	Fine	69.35	–0.50	100	50	2.6	1.3
V	K-alpha	LIF220	FPC	Fine	123.06	–0.50	100	50	0.7	21.5
Ti	K-alpha	LIF200	FPC	Fine	86.14	+0.50	40	20	4.9	
Ce	L-alpha	LIF220	FPC	Medium	128.16	–1.50	100	50	3.2	3.4
Ba	L-Beta	LIF220	FPC	Medium	128.78	–1.50	100	50	1.8	6.3

Notes: All major elements measured using a rhodium X-ray tube operated at 30 kV and 80 mA. Trace elements are measured using a rhodium X-ray tube operated at 50 kV and 50 mA. Detector: FPC = flow proportional counter (P10 gas); Scint = NaI Scintillation counter. Detection limits in wt% for major oxides, ppm for trace elements.

the multisensor track. Thermal conductivity was measured on whole-round sections of selected holes, at discrete intervals (at least one every second section) using the needle probe method. Index properties (wet-bulk density, grain density, dry-bulk density, water content, and porosity), compressional-wave velocity, undrained shear strength, and resistivity were measured on samples from split sections at approximately the same intervals in the sections. Measurements were made at a varying frequency depending on lithology, but approximately one per section.

Multisensor Track

The multisensor track (MST) incorporates the gamma-ray attenuation porosity evaluator (GRAPE), *P*-wave logger (PWL), magnetic susceptibility meter, and natural gamma radiation (NGR) sensor. The MST sensors are most reliable in advanced hydraulic piston corer (APC) cores that have not been disturbed by gas expansion and in undisturbed extended core barrel (XCB) cores, because disturbed cores often contain artificial voids within the sediment or gaps between the core and liner. All intact sections, excluding core catchers and those with deformed core liners, were run through the MST.

Wet-bulk density was determined with the GRAPE at 2-cm intervals by comparing the attenuation of gamma rays through the cores with gamma-ray attenuation through aluminum and water standards (Boyce, 1976). Recalibration was typically performed between sites.

The PWL transmits a 500-kHz compressional-wave pulse through the core at a repetition rate of 1 kHz using transmitting and receiving transducers that are aligned perpendicular to the core axis. A pair of displacement transducers monitors the separation between the compressional-wave transducers, and variations in the outside diameter of the core liner, therefore, do not degrade the accuracy of the velocities. Measurements were taken at 3-cm intervals, and weak returns having low signal strength (<100) were removed from the database.

Magnetic susceptibility was measured on all sections at 3- to 5-cm intervals using the 0.1 and 1.0 ranges on the Bartington meter with an 8-cm diameter loop (refer to the "Paleomagnetism" section of this chapter for measurement details). The quality of the susceptibility data degrades in XCB sections in which the core is undersized or disturbed.

Natural gamma radiation was measured at 30-cm intervals. Background radiation was measured periodically for subsequent removal from the data. The NGR sensor is particularly sensitive to sample volume (Hoppie et al., 1994). Because microfractures and centimeter-to-decimeter-scale gaps were common in cores from all sites, it was not possible to apply a volume correction to the NGR data during Leg 155. The extent of the error in the uncorrected data was determined to be of sufficient magnitude that the NGR data are not described in the site chapters.

Thermal Conductivity

Thermal conductivity was measured using the needle probe method in full-space configuration for soft sediments (von Herzen and Maxwell, 1959). Measurements were made with a Thermcon-85 unit, and data are reported in units of W/(m·K). The estimated error is 5%–10%.

Cores were allowed to equilibrate until the sediments reached a temperature near that in the lab prior to measuring. A needle probe was inserted in every other section, through holes drilled through the liners. The test sequence was then delayed until the background drift in all samples had been reduced to an arbitrary level of 0.04°C/min.

Once the samples were fully equilibrated, the heater circuit was closed, and the temperature rise of the probes was recorded. After the heater has been on for about 60 s, the needle probe response is very close to that of a line source with a constant heat generation, and the subsequent temperature rise in the probe should vary logarithmically with time as:

$$T(t) = (q/4\pi k)\ln(t) + \text{constant} \quad (1)$$

where k is the apparent thermal conductivity, T is temperature, t is time, and q is the heat generated per unit length of the probe. Thermal conductivity measurements were not made in sediments that were too stiff to allow easy insertion of the probes.

The calibration of the thermal conductivity probes was checked by conducting measurements on three standards with known thermal conductivities: black rubber, 0.54 W/(m·K); red rubber, 0.96 W/(m·K); and macor ceramic, 1.61 W/(m·K). The linear regression of the known thermal conductivity to the probe reading results in a correction that was applied to the conductivity measurements. A reference standard was run with each group of sections and was rotated among probes between measurements.

Index Properties

Water content, wet-bulk density, grain density, dry-bulk density, and porosity were determined from measurements of wet and dry sediment weight and wet and dry sediment volume. Samples of approximately 10 cm^3 were taken from undisturbed core intervals and placed in precalibrated aluminum beakers. Sample weights were determined to a precision of ±0.01 g on a Scientech electronic balance. Wet and dry volumes were determined with a Quantachrome Penta-Pycnometer, a helium-displacement pycnometer, which measures volumes to an approximate precision of ±0.02 cm^3. Sample volumes were repeated until two consecutive measurements yielded volumes within 0.02 cm^3 of each other. A reference volume was run with each group of samples and was rotated among the cells between runs. Dry weights and volumes were measured after the samples dried at 105°C for 24 hr and were allowed to cool in a desiccator. A salt correction assuming 35 interstitial salinity was applied to grain density and porosity calculations (but not to bulk density) following Hamilton (1971) and Boyce (1976).

The index properties were calculated using the following relationships:

Water content (% wet weight): $WC_w = (M_t - M_d) \cdot (1 + s) / M_t$
Water content (% dry weight): $WC_d = (M_t - M_d) / (M_d - sM_t)$
Wet-bulk density: $\rho = M_t / V_t$
Dry-bulk density: $\rho_d = M_s / V_t$
Grain density: $\rho_s = M_s / V_s = (M_d - s) / [V_d - (s / \rho_{salt})]$
Porosity: $\phi(\%) = (V_v / V_t) \cdot 100$
or $\phi(\%) = (\rho_s - \rho) / (\rho_{salt} - \rho_{pw}) \cdot 100$
Void ratio: $e = V_v / V_s$

where:

M_t = total mass (saturated)
M_d = dry mass (sediment solids and salt)
M_s = mass of the sediment solids
V_t = total volume
V_d = dry volume
V_s = volume of the sediment solids
V_v = volume of the voids (equivalent to the volume of the pore water)
s = salinity (assumed to be 35 g/kg)
ρ_{pw} = pore water density (assumed to be 1.024 g/cm^3)
ρ_{salt} = density of salt (assumed to be 2.257 g/cm^3)

The values for M_s, V_s, and V_v are determined from the measured weights and volumes by using the mass of the evaporated water and

the assumed value of ρ_{pw} to estimate the mass and volume of the pore fluid. Wet-bulk density, dry-bulk density, porosity, and void ratio were determined directly using the measured total (wet) volume, and indirectly using the dry volume and assumed values for pore fluid salinity and density, to estimate the total volume according to the relationship:

$$V_t = V_d + (M_t - M_d) / \rho_{pw} \quad (2)$$

The variation in index properties at the Leg 155 sites is described primarily in terms of the variation in water content. Unless otherwise specified, the water content used is that expressed as percent wet weight.

Compressional-wave Velocity

In addition to the MST velocity measurements, compressional-wave (*P*-wave) velocities were determined using two additional systems, depending on the degree of lithification of the sediment. *P*-wave velocities in unconsolidated sediment were measured using a Digital Sound Velocimeter (DSV) (Mayer et al., 1992). The compressional velocity calculation was based on the accurate measurement of delay time of an impulsive acoustic signal travelling between a pair of piezoelectric transducers inserted in the split sediment cores. The DSV transducers emitted a 2 µs square wave; the transducers have resonances at about 250 and 750 kHz.

The DSV has two transducers to measure the longitudinal (perpendicular to bedding) *P*-wave velocity, and two additional transducers, orthogonal to the first set, to measure the transverse (parallel to bedding) *P*-wave velocity. The transducers were firmly fixed to a steel plate so that their separation remained relatively constant during the velocity determinations. The longitudinal transducer separation was approximately 7.35 cm, whereas the transverse transducer separation was approximately 3.85 cm. Before each hole, the transducer separation was evaluated by measuring the separation and running a calibration procedure in distilled water. A value of sound velocity in distilled water was determined (based on standard equations) for the measured temperature and the transducer separation was calculated from signal travel time.

A dedicated microcomputer controlled all functions of the velocimeter. The transmitted and received signals were digitized by a Nicolet 320 digital oscilloscope and transferred to the microcomputer for processing. The DSV software selected the first arrival and calculated sediment velocity; the full waveform was stored for later calculation of attenuation. The first arrivals were then picked manually. Sediment temperature was measured and recorded to permit in-situ temperature correction.

The Hamilton Frame Velocimeter was used to measure compressional-wave velocities at a signal frequency of 500 kHz in discrete sediment samples for which induration made it difficult to insert the DSV transducers without cracking the sample. Samples were either manually extracted or cut carefully using a double-bladed diamond saw, making two parallel sides. Sample thickness was measured directly from the velocimeter-frame lead screw through a linear resistor output to a digital multimeter. Delays for the transducers were estimated by linear regression of travel time vs. distance for a series of aluminum and lucite standards. Filtered seawater was used to improve the acoustic contact between the sample and the transducers. The DSV oscilloscope and processing software was used to digitize waveforms, calculate velocities, and store the waveforms. The routine procedure of measurement was to propagate the waveform parallel to the core axis (longitudinal) and across the core when possible. This approach provides a measure of the acoustic anisotropy within the sediments. We report here uncorrected velocities because corrections for in-situ temperature and pressure (Wyllie et al., 1956) were not made.

Velocity anisotropy was calculated when longitudinal and transverse velocities were measured with the DSV. Anisotropy was calculated using the relationship of Carlson and Christensen (1979), where anisotropy is given as the ratio of velocity difference to the mean velocity, expressed as a percentage:

$$A_V = 200\ (V_t - V_l)/(V_t + V_l) \quad (3)$$

where V_t = transverse velocity and V_l = longitudinal velocity.

Undrained Shear Strength

The undrained shear strength (S_u) of the sediment was determined using the ODP motorized miniature vane shear device following the procedures of Boyce (1976). The vane rotation rate was set to 65 degrees per minute. Measurements were made only in the fine-grained units from soft to very stiff consistencies and determined perpendicular to the core axis. The vane used for all measurements has a 1:1 blade ratio with a dimension of 1.27 cm. Springs of various strengths were available. These springs had been calibrated prior to Leg 155.

The instrument measures the torque and strain at the vane shaft using a torque transducer and potentiometer, respectively. Output for torque and strain are recorded on a microcomputer. The shear strength reported is the peak strength determined from the torque vs. strain plot. In addition to the peak shear strength, at selected intervals, the residual strength was determined from the same plot where the failure was not dominated by cracking of the sample (Pyle, 1984).

In the analyses of vane tests, the assumption is made that a cylinder of sediment is uniformly sheared about the axis of the vane in an undrained condition, with cohesion as the principal contributor to shear strength. Departures from this assumption include progressive cracking within and outside of the failing specimen, uplift of the failing core cylinder, drainage of local pore pressures (i.e., the test can no longer be considered to be undrained), and stick-slip behavior. Most samples failed by fracturing. The fractures varied from minor cracks on the split-core surface to large cracks (up to 5 mm wide) that extended across the core. The onset of failure by major fracturing typically coincided with the increase in variability in shear strength. Failure of samples at low strain angles (<15°) was rejected as being an inaccurate measure of shear strength.

In some sediments, where undrained shear strengths were anticipated to exceed the capability of the motorized shear vane, measurements were made using the pocket penetrometer. The pocket penetrometer is a small, flat-footed cylindrical probe of 6.33-mm diameter that is pushed into the split core 6.4 mm. The resulting resistance is the unconfined compressive strength q_u, which for fine-grained sediments approximates 2 S_u. A scale directly reads out in units of kg/cm^2. The values of unconfined compression are converted to values of S_u and are reported in units of kPa.

Electrical Resistivity

A four-probe configuration (Wenner spread) with two current and two potential electrodes system was used to determine electrical resistivity. The device applies a 5-volt alternating square wave across the outer electrodes and measures the potential drop between two electrodes with a 0.15-mm spacing. The resistance of the saturated sediment is determined from the potential drop in mV, which is converted to resistance by dividing by the instrument current. The resistance is then converted to resistivity by multiplying by the instrument cell constant, which is defined as the cross-sectional area divided by the length between the two voltage electrodes. The cell constant was determined for each instrument by measuring the resistance of a known fluid (seawater) at controlled temperatures. Electrical resistivity of the sediments was measured by pushing the electrodes approximately 2 mm into the split core surface. Measurements were made

both parallel to and perpendicular to the core axis to give longitudinal and transverse values.

The anisotropy of resistivity was calculated as the difference between the transverse (r_t) and longitudinal (r_l) resistivity divided by the mean resistivity, expressed as a percentage:

$$A_r = 200\,(r_t - r_l)/(r_t + r_l) \quad (4)$$

DOWNHOLE LOGGING

Introduction

The Lamont-Doherty Earth Observatory Borehole Research Group (LDEO-BRG) in conjunction with the University of Leicester (Borehole Research-Leicester), the Institut Méditerranéen de Technologie (IMT), and Schlumberger Well Logging Services, provided the geophysical well logging aboard the *JOIDES Resolution*. Primarily designed for use in hydrocarbon exploration, logging tools have been adapted to meet ODP requirements and hole conditions. This includes the reduction of tool diameter to allow insertion into the 3.8-in. drill-string bore. Downhole logs are used to directly determine physical, chemical, and structural properties of formations penetrated by drilling. Log data are collected continuously and allow for quantification of the formation's stratigraphic, lithologic, geophysical, and mineralogic characteristics. Where incomplete core recovery has occurred, log data may then serve as a proxy for physical properties and sedimentological data. They also complement the discrete measurements obtained from cores, and offer several advantages over core-based analyses in that they are rapidly collected and represent continuous, in-situ measurements of the formation. Integration of continuous and multivariate log data with core data can potentially ground-truth information provided by detailed core analyses, resulting in continuous and quantitative records of sediment lithologic variability. Geophysical well-logging is also used to aid in characterization of sedimentary sequences when integrated with core and seismic reflection data. Therefore, the implementation of high-resolution logging techniques available through the new Schlumberger MAXIS 500 logging system has provided Leg 155 a good opportunity to investigate well-log responses in a high-sedimentation-rate depositional setting such as the Amazon Fan.

Well-logging Operations

Standard logging operations are as follows. After coring was completed, the hole was flushed of debris by circulating a pill of heavy viscous drilling fluid (sepiolite mud with seawater) through the drill pipe to the mud line. The bottom-hole assembly (BHA) was pulled up (to ~60–100 mbsf), and then it was run down to the bottom of the hole again to condition the borehole for logging. Tool strings composed of one or more combinations of sensors were then lowered downhole by a 7-conductor wireline during sequential runs. A wireline heave-motion compensator (WHC) was employed to minimize the effect of ship's heave on the tool position in the borehole.

During each logging run, incoming data were acquired, archived, and monitored in real time on the Maxis 500 logging computer. The Cyber Space Unit (CSU) computer was used for the geochemical logging string. After logging, data were transferred to a Sun workstation and a Macintosh computer for preliminary shipboard interpretation.

Logging Tool Strings

Logging sensors continuously monitor geophysical, geochemical, or structural properties of the formation, which are recorded typically at 15-cm depth increments. The depths of investigation into and vertical resolutions of the formation are sensor-dependent, but are typically between 50 and 100 cm. Individual logging tools were combined in five different strings (Fig. 14): (1) quad-combination tool, (2) gamma-resistivity tool, (3) Formation MicroScanner tool (FMS), (4) geochemical logging tool (GLT), and (5) geological high-sensitivity magnetic tool (GHMT-A). The Quad-combination tool string reaches a total length of 31 m (33 m with the Lamont-Doherty Temperature Tool [TLT]), making it difficult or impractical to run in short holes, but provides for rapid acquisition of several parameters. Because of the limited time available to achieve all objectives of Leg 155, we did not "split" the Quad-combination tool into two separate tool strings. The TLT was attached to the bottom of all tool strings except the FMS and the GHMT-A. The natural gamma-ray tool (NGT) was placed at the top of all tool strings to facilitate correlation between logging runs at a single site.

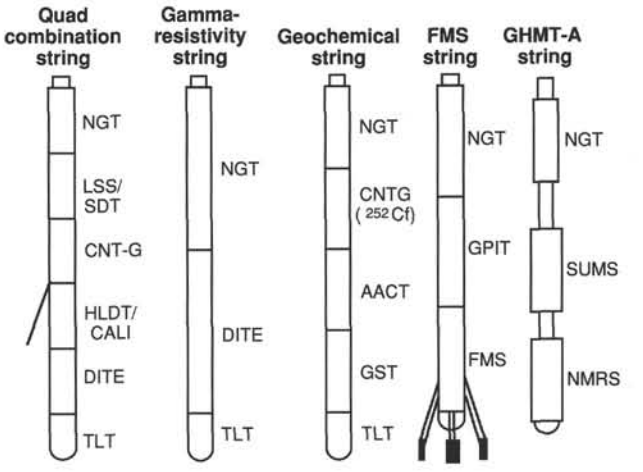

Figure 14. Schematic diagram of Schlumberger logging tool strings used during Leg 155. Tool strings are not drawn to scale.

A brief description of the logging tools employed during Leg 155 is given below. The detailed principles of operation of the various logging sensors can be found in Ellis (1987), Schlumberger (1989), Serra (1984), and Timur and Toksöz (1985).

Natural Gamma-ray Spectrometry Tool (NGT)

The NGT measures the natural radioactivity of the formation using a NaI scintillation crystal detector mounted inside the tool. This tool measures both the number of gamma rays and the energy level of each and permits the determination of the concentrations of radioactive potassium, thorium, and uranium in the formation (Lock and Hoyer, 1971). Gamma rays are emitted by radioactive isotopes of ^{40}K, and by the radioactive isotopes of the ^{238}U and ^{232}Th decay series that are present in the formation. Measurements are analyzed by dividing the incident gamma-ray signature into five discrete energy windows that correspond to the main spectral peaks for each element. The total counts recorded in each window, for a specified depth in the well, are inverted to give the elemental abundances of K (wt%), U (ppm), and Th (ppm). The NGT also provides a measure of the total gamma-ray signature [SGR = (K + U + Th)] and a uranium-free measurement [CGR = (K + Th)]. Values are recorded every 0.1524 m and have a vertical resolution of the order of 0.46 m. Gamma-rays emitted by the formation rarely reach the detector directly. They are scattered and lose energy through Compton scattering and pair production (Schlumberger, 1989). Therefore, the degree of detection depends primarily on the extent of variation in gamma-ray emission by the formation.

The NGT is run on all tool strings to provide a common basis for log correlations. Its measurement is also commonly used to estimate the clay or shale content due to the relatively high abundance of K,

U, and Th in clay minerals. The presence of these elements, for example, in volcaniclastic sediments and K-feldspar-rich sands requires cross correlation of the NGT data to recovered core and other logging data to verify lithologic interpretations. The gamma-ray data provided by the NGT are also useful in estimating the organic carbon content of the formation (usually associated with high U counts), and U/Th ratios have been used to distinguish changes in the oxidation state of diagenetic minerals.

Phasor Dual Induction Spherically Focused Resistivity Tool (DITE-SFL)

The DITE-SFL provides three different measurements of electrical resistivity. Each of these has a different depth of investigation into the formation: deep induction (IDPH), medium induction (IMPH), and shallow spherically focused resistivity signals (SFL). The measurements are combined through signal processing to provide a log with thin bed resolution, and with full correction for environmental distortions such as irregularities in borehole diameter (borehole effect) and rugosity (shoulder effect) (Schlumberger, 1989). The two induction devices (IDPH and IMPH) transmit high-frequency alternating currents through transmitter coils, creating magnetic fields that induce secondary (Foucault) currents in the formation. These ground-loop currents produce a new inductive signal, proportional to the conductivity of the formation, which is measured by the receiving coils. The measured conductivity is then converted to resistivity (in Ωm). The SFL measures the current necessary to maintain a constant voltage drop across a fixed interval. The vertical resolution for the resistivity values is 2 m, 1.5 m, and 0.75 m, respectively, for the IDPH, IMPH, and SFL. Values are recorded every 0.1524 m.

Water content and salinity are the most significant factors controlling the electrical resistivity of a formation. Resistivity is primarily related to the inverse square root of porosity (Archie, 1942). Other factors influencing resistivity of a formation include the concentration of hydrous and metallic minerals, hydrocarbons and gas hydrates, and pore structure geometry, distribution and interconnection.

Long Spaced Sonic Tool (LSS/SDT)

The sonic tool measures the time required for sound to travel through the formation between a transmitter and a receiver. It provides a direct measurement of sound velocity through sediments from the interval transit time (slowness, Δt) measured, and is likely to yield values free from the effects of formation damage and enlarged borehole from drilling processes (borehole compensation). Sound velocity is an indirect measurement of sediment porosity and lithification. The data were used in conjunction with density logs (from the HLDT, see next section) and core physical property measurements to compute synthetic seismograms.

The configuration of the LSS/SDT (long spaced sonic tool/digital sonic cartridge) used during the first logging run on Leg 155 failed as a result of flooding of the SDT. We then used a spare LSS sonde for the remainder of the leg. The tool contains two broadband piezoelectric ceramic transmitters spaced 2 ft (0.61 m) apart and two piezoelectric receivers spaced 2 ft (0.61 m) apart. This configuration provides a total of four different transit times with source-receiver spacings of 8 ft (2.44 m) to 10 ft (3.05 m) and 10 ft (3.05 m) to 12 ft (3.66 m). Depth-derived processing during acquisition gives the sonic transit times through 1 ft (0.31 m) of the formation, compensated for borehole irregularities. Interval transit times then are converted to compressional-wave velocities (km/s). Full waveforms are recorded by the tool, allowing shore-based post-processing to estimate shear and Stoneley-wave velocities, as well as amplitude attenuation. Logs were corrected for cycle-skipping (where the receiver misses the first arrival and responds to that of the second signal) using the multi-fold measurement redundancy and filtering.

High-temperature Lithodensity Tool (HLDT)

The HLDT uses a ^{137}Ce radioactive source and two detectors mounted on a shielded sidewall skid that is pressed against the formation by a hydraulically activated arm. The arm also provides a caliper measurement of borehole diameter. The medium-energy gamma rays (662 keV) emitted by the source lose energy by interaction with the electrons in the formation through Compton scattering until absorbed through the photoelectric effect. The number of gamma rays reaching the two detectors yields an energy spectrum for each detector that is directly related to the number of electrons in the formation, which in turn is related to the bulk density. The resulting bulk densities are computed, assuming that most rock-forming elements have a ratio of atomic weight to atomic number of two.

Photoelectric absorption occurs when the gamma rays reach a low energy (<150 keV) after being continually scattered in the formation. The photoelectric effect index (PEF) is determined by comparing the counts of the far detector in the high-energy portion of the spectrum, which primarily record Compton scattering, with the counts of the far detector in the low-energy window, where the counts depend on both Compton scattering and photoelectric absorption. The near detector is also used to determine corrections for borehole conditions and rugosity. The photoelectric effect depends on the atomic number of the elements in the formation, thus its magnitude is nearly independent of porosity. The PEF values, when used in combination with the NGT curves, may provide an indication of the different types of clay minerals in the sediments.

Good contact between the sensors and the borehole wall is essential for good HLDT logs. Poor contact leads to abnormally low density values, which are recognizable from large values of the density correction curves (DRHO). The vertical resolution of the measurements is of the order of 0.45 m. Recent comparisons with core data (ODP Leg 138: Harris et al., in press) suggest this value is closer to 0.8 m. An enhanced resolution mode can be attempted by decreasing the logging speed to 300 m/hr (from the standard 600 m/hr) and by taking advantage of the measurements of the near detector-source spacing (15 cm) and the more stable measurements of the far detector. Sample measurement interval is decreased from the standard 15 cm to 2.5 cm and the resolution approaches 15 cm. The enhanced resolution mode is only possible with ideal hole conditions and good tool-to-wall contact.

Compensated Neutron Porosity Tool (CNT-G)

The CNT-G uses a 16 Curie Am-Be source, which bombards the formation and borehole with fast neutrons (4.5 MeV), and two pair of sensors to detect the number of neutrons (count rates) in the epithermal (0.1–100 eV) and thermal (<0.025 eV) energy ranges. The emitted neutrons interact elastically with the surrounding atoms, and the greatest energy loss occurs with atoms of small capture cross section, in particular hydrogen atoms (almost the same mass as one neutron). Thus the slowing-down and capture of the emitted neutrons is primarily controlled by the amount of hydrogen surrounding the tool. This hydrogen resides almost entirely in water molecules. Because this tool is very sensitive to hydrogen, it may provide the capability to detect occurrences of gas and gas hydrates. The tool is designed to be run against the borehole wall. Because no eccentralizer springs were used on the Quad-combination tool string, neutron-porosity data from the CNT-G should be used with caution. Poor tool contact with the borehole wall generally leads to an overestimated formation porosity because, in addition to the borehole water, neutrons are strongly absorbed by C. Tool vertical resolution is approximately 0.45 m.

Both mineral-bound water (e.g., clay minerals) and water filling the pore space affect tool response, commonly leading to an overestimate of true porosity, although changes in neutron-porosity values are often useful to distinguish between mud and sand. Free water con-

tent (porosity) is determined from the thermal neutron counts. Water that is structurally bound can be estimated by subtracting free water from the total water estimates. Neutron logs are also affected to some extent by matrix lithology of the formation. When the borehole fluid is gas charged, this effect is reduced to a negligible level. However these effects and that caused by the amount and type of hydrocarbon, can be recognized and corrected for only if additional porosity information (i.e., from sonic and/or density logs) is available.

Geochemical Logging Tool String (GLT)

The geochemical logging tool consists of four parts: a natural gamma-ray spectrometry sensor (NGT), a neutron porosity tool (CNTG) used as a carrier for a ^{252}Cf source of neutrons (2 MeV instead of the 4.5 MeV for the Am-Be source) that serves as the activation source for the aluminum activation clay tool (AACT) (Hertzog et al., 1989), and the gamma-ray spectroscopy tool (GST) (Fig. 15).

These tools use three separate modes of gamma-ray spectroscopy for a comprehensive elemental analysis of the formation. The NGT is located at the top of the tool string so that it can measure the naturally occurring radionuclides, thorium (Th), uranium (U), and potassium (K), before the formation is irradiated by the nuclear sources contained in the lower tools (Fig. 15). The CNT, located below the NGT, carries a californium (^{252}Cf) neutron source to activate the Al atoms in the formation. The AACT, a modified NGT, is located below the ^{252}Cf source, measuring the activated gamma rays in the formation. The lower energy of the californium source in the CNTG, compared to the CNT-G tool described in the previous section, reduces the number of fast neutron reactions that would interfere with the aluminum activation (AACT) measurement. Neutrons emitted by the ^{252}Cf source react with ^{27}Al, and thermal neutron capture by ^{27}Al results in the formation of ^{28}Al (Scott and Smith, 1973). The latter decays to ^{28}Si with a half-life of 1.3 min and emits gamma rays with 1.78 MeV. The AACT is essentially similar to the NGT, but measures the gamma-ray spectrum of the activated formation in three additional windows. By combining the AACT measurements with those from the NGT in the same tool string, the background rotation is subtracted and a measure of the Al concentration in the formation is obtained (in wt%). The AACT is calibrated by taking irradiated core samples of known volume and density and measuring their gamma-ray signature while the samples are in a jig attached to the logging tool.

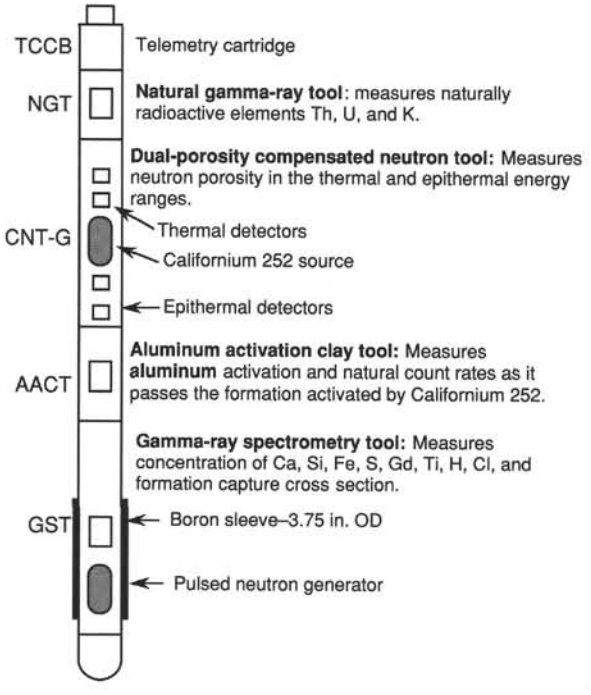

Figure 15. Schematic drawing of the Schlumberger geochemical logging tool string used by the Ocean Drilling Program.

The GST is located at the base of the string and consists of a high-energy pulsed neutron accelerator (14 MeV) and a NaI scintillation crystal detector. The gamma rays emitted by the nuclei in the formation after prompt-neutron capture are detected by a NaI (Tl) scintillation crystal detector. Each element has a characteristic spectral signature permitting derivation of the relative contribution (yields) of each of the major elements that dominate the spectrum: Si, Ca, Fe, K, S, Cl, and H. Calculation of absolute concentrations (wt%) of elemental oxides required additional shore-based processing to estimate the contribution of rare-earth elements (Gd and Sm in particular) and Ti (Hertzog et al., 1989). The GLT is run at approximately 200 m/hr, and data can be obtained through pipe, although results are severely degraded. Detailed information regarding the onshore processing of the GLT data for Leg 155 is given below.

Formation MicroScanner Tool String (FMS)

The FMS string produces high-resolution images of the microresistivity character of the borehole wall that can be used for detailed sedimentological and structural interpretations (Ekstrom et al., 1986; Hiscott et al., 1992). It allows continuous observation and description of detailed vertical and lateral variations, and detection of very thin anomalous features such as fractures that have an opening on the order of a few to tens of microns (Serra, 1989). The FMS tool comprises four orthogonal pads with 16 button electrodes (6.7 mm in diameter) on each pad that are pressed against the borehole wall (Serra, 1989). The electrodes are arranged in two diagonally offset rows of eight electrodes each. Each pad measures about 8 cm^2, and one pass of the tool covers approximately 30% of a 25.72 cm (10.12 in.) borehole. Each individual electrode emits a focused current into the formation. The button electrode current intensity measurements, which reflect microresistivity variations, are converted to variable intensity color images. Processing corrects the offset rows to one level, providing a vertical resolution of approximately 0.5 cm at a sampling interval of 0.25 cm (Serra, 1989). The FMS tool string contains a general purpose inclinometry tool (GPIT) that orients the resistivity measurements through the use of a three-axis accelerometer and a magnetometer. The raw data are processed in real-time during logging to transform individual microresistivity traces into complete, oriented images. Full-color images are available immediately after logging, although at a reduced scale, for quality control purposes. Detailed correlation of coring and logging depths, core orientation, mapping of fractures, faults, foliations, and other formation structures, as well as determination of strikes and dips of bedding planes are also possible. In addition, the FMS can be used to measure stress orientations in the borehole with precise measurements of borehole diameter in two orthogonal directions. Raster images of the FMS logs, prepared onshore after the leg, are on the CD-ROM that accompanies this volume (back pocket).

The Lamont-Doherty Temperature Tool (TLT)

The LDEO temperature logging tool (TLT) is a high-precision, low-temperature logging tool that can be attached to the base of any of the above Schlumberger tool strings. It is self-contained and provides a series of accurate temperature logs while keeping total logging time the same. Data from two thermistors and a pressure transducer are collected every 1 s and are recorded internally. Once the in-situ measurement is completed, the data are transferred to a shipboard computer for analysis. The fast-response thermistor, although less accurate, is able to detect small, abrupt temperature excursions caused by fluid flow from the formation. The slow-response

thermistor is more accurate and can be used to estimate the temperature gradient. Data are recorded as a function of time, with conversion to depth based on the pressure transducer and on the synchronized time-depth record of the wireline cable. The TLT measures the borehole water temperature, not the true formation temperature; it is common to observe gradual borehole warming (thermal rebound) as logging proceeds. The TLT data are not representative of the true thermal gradient and, hence, should not be used in heat flow calculations except in boreholes that have been left undisturbed for periods of time long enough for equilibrium with the formation to occur.

Geological High-sensitivity Magnetic Tool String (GHMT-A)

The GHMT-A, a high sensitivity total magnetic field sensor coupled with a susceptibility sensor, was deployed during Leg 155 to test its effectiveness in resolving borehole magnetic polarity transitions and susceptibility variations. This tool was developed jointly by Schlumberger, French government research institutions (CEA-LETI and CNRS-ENS), and an oil company (TOTAL). The tools were designed and constructed by a branch of the French Atomic Energy Commission (CEA-LETI), which also developed the analysis software.

Magnetic induction **B** in a borehole depends on position p and time t (Pozzi et al., 1988) with:

$$\mathbf{B}(p, t) = \mathbf{Br}(p) + \mathbf{Ba}(p) + \mathbf{Bf}(p) + \mathbf{Bt}(p, t). \quad (5)$$

Br(p) is the dipolar Earth's field, whereas **Ba**(p) is the anomaly field related to large-scale heterogeneities in susceptibility or in magnetic remanence. In the absence of such heterogeneities, the spatial variation of **Br** with depth is linear. **Bf**(p) is the induction due to the magnetization (induced and remanent) of the sediments around the borehole and can easily be separated from **Br**(p) and **Ba**(p), respectively, by subtracting a linear function (Earth's magnetic field gradient) and applying a high-pass filter. **Bt**(p, t) is time dependent and represents the induction due to transient variations of the Earth's magnetic field. At sea, the time-dependent component can be estimated by repeat sections. To obtain direct magnetostratigraphy from **Bf**(p), the susceptibility and the total field measurements are combined to discriminate the induced and remanent magnetizations. Specifications of the probes, such as impulse response, calibration ratio, and geomagnetic location of the hole, are used to calculate the susceptibility effect on the scalar total field magnetometer. From these data the scalar remanent magnetization can be calculated.

The GHMT-A tool string consists of two tools, NMRS and SUMS. The NMRS (Nuclear Magnetic Resonance Sonde) can be used in borehole temperatures up to 125°C; however, the NMRS used for Leg 155 is more precise and has a maximum operating temperature of 60°C. Average precision of 0.5 nT is based on duplicate runs. The SUMS (Susceptibility Magnetic Sonde) detects the mutual induction signal between two coils (0.8 m apart) caused by the surrounding borehole lithology. The excitation frequency is about 200 Hz. The precision between duplicate runs is generally better than 3 ppm (3×10^{-6} SI). Both sensors are housed by nonmagnetic materials; the tool is logged at 600 m/hr or at 300 m/hr (for higher resolution), and the data are recorded every 5 cm.

The two sondes have been used separately in numerous onshore and offshore scientific- and industry-based wells, including those drilled during Leg 134 at Site 833, and Leg 145 at Sites 883 and 884. The magnetostratigraphic interpretation of the recorded logs usually gave good results when compared to those obtained from cores recovered in the same holes (Pozzi et al., 1993; Dubuisson et al., in press a, b).

CD-ROM Materials

The CD-ROM in the back of this volume contains both depth-shifted and processed logging data that has been provided by the Borehole Research Group at Lamont-Doherty Earth Observatory (BRG-LDEO).The CD-ROM also contains shipboard measurements on cores collected on board *JOIDES Resolution* during Leg 155 (MST data, index and physical properties, and color spectra). CD-ROM production was done by the BRG-LDEO, wireline logging operator for ODP.

The CD-ROM contains an "INDEX" file with a summary of all the files loaded on the CD-ROM (see also table of contents, this volume). The software documentation file in the "GENERAL INFORMATION" directory contains information about which software packages work best to import portable bit map (PBM-8-bit binary) raster files. This file also includes network sources for the graphics software and data compression information. The "README" file contains information about whom to contact with any questions about the production of or data on the CD-ROM.

All of the ASCII files (basic logging and dipmeter files) are tab-delimited for compatibility with most spreadsheet and database programs. Holes that have long logging runs are often divided into "TOP," "MIDDLE," and "BOTTOM" directories. If the data were collected continuously or if two or more sections of data were spliced together, the files would be in the "SPLICED" directory.

In the "FMS-PBM" subdirectory there are two subdirectories: 1:1, with maximum 10-m-long raster images at a 1:1 scale, and 1:10, with maximum 100-m-long raster images at a 1:10 scale. The image raster files are named according to their depth interval. The raster documentation files contain image file parameter information necessary for use with most graphic-software packages.

Shore-based Log Processing

Additional log processing and display were performed on shore for each of the eight logged sites by the Borehole Research Group at LDEO, (Institut Méditerranéen de Technologie (IMT), and Borehole Research-Leicester University, using Schlumberger LOGOS software and additional programs developed by the BRG-LDEO. Displays of these processed data appear with accompanying text at the end of the appropriate site chapters in this volume. Files of all processed logs (including FMS, dipmeter, TLT, high-resolution density, and neutron data), sonic waveforms, and explanatory text are included in the CD-ROM (back pocket).

Shore-based processing of data from each hole consisted of: (1) depth adjustments of all logs to a common measurement below the seafloor; (2) corrections specific to certain tools; and (3) quality control and rejection of unrealistic values.

The depth-shifting procedure is based on an interactive, graphical depth-match program that allows the processor to visually correlate logs and define appropriate shifts. The reference log and the log to be adjusted in depth are displayed side-by-side on a screen, and vectors connect the two at positions chosen by the user. The total gamma-ray curve (SGR) from the NGT tool run on each logging string was used in most cases to correlate the logging runs. In general, the reference curve is chosen on the basis of constant, low cable tension and high cable speed (tools run at faster speeds are less likely to stick and are less susceptible to data degradation caused by ship's heave). Other factors, however, such as the length of the logged interval, the presence of drill pipe, and the statistical quality of the collected data (better statistics are obtained at lower logging speeds) are also considered in the selection. A list of the amount of differential depth shifts applied at each hole is available upon request to BRG (LDEO).

Specific tool corrections were performed on the gamma-ray data to account for changes in borehole size and for the composition of the

drilling fluid. Processing techniques unique to the AACT and GST tools of the geochemical string are described in detail below.

In addition to the standard 15.24-cm sampling rate, bulk density and neutron porosity data were recorded at a sampling rate of 2.54 and 5.08 cm, respectively. The enhanced bulk-density curve is the result of Schlumberger enhanced-processing technique performed on the MAXIS 500 system on board ship. Whereas in normal processing, short-spacing data are smoothed to match the long-spacing ones, in enhanced processing this is reversed. Where there is good contact between the HLDT pad and the borehole wall (low-density correction), the results are improved, because the short-spacing data have better vertical resolution.

Quality control was performed by cross-correlation of all logging data. If the data processor concluded that individual log measurements represented unrealistic values, the choices were to either discard the data outright and substitute the null value of "–999.25," or identify a specific depth interval containing suspect values that must be used with caution. The latter are noted in the text that accompanies all processed log displays. Quality control of the acoustic data was based on discarding any of the four independent transit time measurements that were negative or that fell outside a range of reasonable values selected by the processor.

Locally, some intervals of log data appeared unreliable (usually due to poor hole conditions) and were not processed beyond what had been done aboard the ship. In general, a large (>12 in.) and/or irregular borehole adversely affects most recordings, particularly those that require eccentralization and a good contact with the borehole wall (CNTG, HLDT). Hole deviation also can degrade the data; the FMS, for example, is not designed to be run in holes that are more than 10° off vertical, as the tool weight might cause the caliper to close.

ONSHORE GEOCHEMICAL PROCESSING[3]

Geochemical Tool String

During Leg 155 two holes (931B and 936A) were logged with the geochemical logging tool (GLT). In this section we describe in detail the processing steps performed on the data to derive the concentration of elemental oxides in the logged sediments. The processed logs are shown at the end of the appropriate site chapters and in the enclosed CD-ROM (back pocket). The gamma-ray spectrometry tool, at the base of the GLT string, carries a pulsed neutron generator to induce prompt-capture gamma-ray reactions in the borehole and formation and an NaI(Tl) scintillation detector to measure the energy spectrum of gamma rays generated by the prompt neutron capture reactions. As each of the elements in the formation is characterized by a unique spectral signature, it is possible to derive the contribution (or yield) of each of the elements silicon (Si), iron (Fe), calcium (Ca), titanium (Ti), sulfur (S), gadolinium (Gd), and potassium (K) from the measured spectrum and, in turn, to estimate the relative abundance of each in the formation when combined with the elemental concentrations from the NGT and AACT (Hertzog et al., 1989). The GST also measures the hydrogen (H) and chlorine (Cl) in the borehole and formation, although these elements are not used for determining the rock composition.

The only major rock-forming elements not measured by the GLT are magnesium (Mg) and sodium (Na); the neutron-capture cross sections of these elements are too small relative to their typical abundances for the GLT to detect. A rough estimate of Mg + Na can be made in some instances by using the photoelectric factor (PEF), measured by the lithodensity tool (Hertzog et al., 1989). This calculation was not implemented on the geochemical data from Hole 931B or 936A as the (Mg+ Na) calculation has proven to be erroneous in ODP logging conditions and only adds noise to the other elements when included (Pratson et al., 1993).

Data Reduction

The well-log data from the Schlumberger tools are transmitted digitally up a wireline and are recorded and processed on the *JOIDES Resolution* in the Schlumberger Cyber Service Unit (CSU). The results from the CSU are made available as "field logs" for initial, shipboard interpretation. Subsequent reprocessing is necessary to correct the data for the effects of fluids added to the borehole logging speed, and drill-pipe interference. Processing of the spectrometry data is required to transform the relative elemental yields into oxide weight fractions.

The processing is performed with a set of log-interpretation programs written by Schlumberger but have been slightly modified to account for the lithologies and hole conditions encountered in ODP holes. The processing steps are summarized below:

Step 1: Depth-shifting

The main pass of the geochemical tool string was chosen as the reference run both in Hole 931B and in Hole 936A.

Step 2: Calculation of Total Radioactivity and Th, U, and K Concentrations

The second processing routine calculates the total natural gamma-ray radiation in the formation, as well as concentrations of Th, U, and K, using the counts in five spectral windows from the NGT (Lock and Hoyer, 1971). This routine resembles shipboard processing; however, the results are improved during post-cruise processing by including corrections for hole-size changes and temperature variations. A Kalman filtering (Ruckebusch, 1983) is used in the CSU processing at sea to minimize the statistical uncertainties in the logs, which can otherwise create erroneous negative values and anti-correlations (especially between Th and U). An alpha filter has been introduced more recently and is now recommended by Schlumberger for shore-based processing. This filter strongly smooths the raw spectral counts but keeps the total gamma-ray curve unsmoothed before calculating out the Th, U, and K. The outputs of this program are K (wet wt%), U (ppm), and Th (ppm), as well as total gamma-ray and computed gamma-ray (total gamma ray minus U contribution). The results for Holes 931B and 936A are displayed in the log summary figures in the relevant site chapter.

Step 3: Reconstruction of Relative Elemental Yields From Recorded Spectral Data

The third processing step compares the measured spectra from the gamma-ray spectrometry tool with a series of standard spectra to determine the relative contribution (or yield) of each element. These standards approximate the spectrum of each element. Using a weighted, least-squares inversion method, the relative elemental yields are calculated at each depth level.

Six elemental standards (Si, Fe, Ca, S, Cl, and H) are used to produce the shipboard yields, but three additional standards (Ti, Gd, and K) can be included in the post-cruise processing to improve the fit of the spectral standards to the measured spectra (Grau and Schweitzer, 1989). Although Ti, Gd, and K often appear in the formation in very low concentrations, they can make a large contribution to the measured spectra because they have large neutron-capture cross sections. For example, the capture cross section of Gd is 49,000 barns, whereas that of Si is 0.16 barns (Hertzog et al., 1989). Therefore, including Gd is necessary when calculating the best fit of the standard spectra to the measured spectrum.

[3]Lee Ewert and Peter K. Harvey, Borehole Research, Department of Geology, University of Leicester, Leicester, LE1 7RH, United Kingdom.

The elemental standards (Si, Ca, Fe, Ti, Gd, Cl, and H) were used in the spectral analysis step for Holes 931B and 936A. The spectral standards for S and K were not used because these elements are present in concentrations below the detection resolution of the tool in these holes; their inclusion in the spectral inversion was found to increase the noise level in the other elemental yields. Note, however, that the concentration of K is later determined from the NGT data. A linear ten point (5 ft, 1.52 m) moving average was applied to the output elemental yields to increase the signal to noise ratios.

Step 4: Calculation of Al Concentration

The fourth processing routine calculates the concentration of Al in the formation using recorded gamma-ray data from four energy windows on the AACT. During this step, corrections are made for natural radioactivity, borehole-fluid neutron-capture cross section, formation neutron-capture cross section, formation slowing-down length, and borehole size.

Porosity and density logs are needed as inputs into this routine to convert the wet-weight percentages of K and Al curves to dry-weight percentages. Porosity logs from the neutron logs were used in both Holes 931B (modified slightly to eliminate tool noise) and 936A (extended above 128 mbsf with core values). The comparison of log-derived porosities with shipboard core measurements provided good correlation for Hole 931B and fair correlation for Hole 936A. The bulk density log-derived curve was used in processing Hole 931B, and core density data was used for Hole 936A.

A correction is also made for Si interference with Al; the ^{252}Cf source activates the Si, producing the aluminum isotope, ^{28}Al, (Hertzog et al., 1989). The program uses the Si yield from the GST to determine the Si background correction. The program outputs dry-weight percentages of Al and K, which are combined in the next processing step with the GST-derived elemental yields in the oxide closure model.

Step 5: Normalization of Elemental Yields from the GST to Calculate the Elemental Weight Fractions

Relative concentrations of the GST-derived elemental yields can be determined by dividing each elemental yield by a relative spectral sensitivity factor (S_i). This factor is principally related to the thermal neutron-capture cross sections and also to its gamma-ray production and detection probability of each element (Hertzog et al., 1989). The relative elemental concentrations are related to the desired absolute concentrations by a depth-dependent normalization factor (F), as defined by the relationship:

$$Wt_i = FY_i / S_i \tag{6}$$

where

Wt_i = absolute elemental concentration,
Y_i = relative elemental yield.

The normalization factor is calculated on the basis that the sum of all the elemental weight fractions is unity (100%). The closure model handles the absence of carbon and oxygen, which are not measured by this tool string, with the approximation that each of the measurable elements combines with a known oxide or carbonate. The dry weight percent of Al and K are normalized with the reconstructed elemental yields to the determine the normalization factor at each depth interval from the following equation:

$$F(\Sigma_i X_i Y_i / S_i) + X_k Wt_k + X_{Al} Wt_{Al} = 100, \tag{7}$$

where

X_i = oxide factor; atomic weight of the associated oxide or carbonate of element i ÷ atomic weight of element i,

Table 9. Oxide factors used in normalizing elements to 100% and converting elements to oxides.

Element	Oxide/ carbonate	Conversion factor
Si	SiO_2	2.139
Ca	$CaCO_3$	2.497
Fe	FeO*	1.358
K	K_2O	1.205
Ti	TiO_2	1.668
Al	Al_2O_3	1.889

Note: * = computed using an oxide factor that assumes a 50:50 combination of Fe_2O_3 and FeO factors.

X_k = oxide factor; atomic weight K_2O ÷ atomic weight of K,
Wt_k = dry wt% of K as determined from the NGT,
X_{Al} = oxide factor; atomic weight of Al_2O_3 ÷ atomic weight of Al,
Wt_{Al} = dry wt% of Al, as determined from the AACT.

The value X_i accounts for the C and O associated with each element. Table 9 lists the oxide factors used in this calculation for Holes 931B and 936A.

Step 6: Calculation of Oxide Percentages

This routine converts the elemental weight percentages into oxide percentages by multiplying each by its associated oxide factor, as shown in Table 9. The results for Holes 931B and 936A are displayed in the log summary figures in the relevant site chapter. Shipboard carbonate and XRF measurements are shown for comparison to the GST-derived oxides/carbonates.

Step 7: Calculation of Error Logs

The statistical uncertainty of each element is calculated for each of the elements measured with the GST and NGT (Grau et al., 1990; Schweitzer et al., 1988). This error is strongly related to the normalization factor, which is calculated at each depth level (Eq. 7). The normalization factor is displayed to the right of the logs in the log summary figures. A lower normalization factor represents better counting statistics and therefore higher quality data.

CORE-SEISMIC INTEGRATION

Introduction

Prior to Leg 155, seismic stratigraphy was the main method used to determine the architecture and growth pattern of the Amazon Fan. A working model of fan formation has been developed using stratigraphic relationships and acoustic facies interpretation (e.g., Damuth et al, 1983; Manley and Flood, 1988; Flood et al., 1991; Pirmez, 1994). To achieve the objectives of Leg 155, particularly those of determining fan chronology and evolution, seismic reflections must be accurately correlated to the core lithology. These correlations should permit extrapolation of the drilled sequences throughout larger areas of the fan.

Physical Properties and Lithologic Changes

The poor quality of laboratory *P*-wave and GRAPE density measurements on Leg 155 preclude the construction of a detailed vertical and *P*-wave velocity density profiles. In the absence of well-log data, changes in the physical property measurements with depth (e.g., pycnometer density-porosity measurements, vane-shear strength) and changes in sediment lithology (e.g., grain size, frequency of silt-sand beds) were used to correlate core depth to individual seismic reflections. Correlation was based on time-depth relationships obtained

from the regional sonobuoy solutions (see next section). The results of this method should be viewed with caution because seismic reflections result from interference patterns resulting from many thin beds (Mayer, 1979) or interval multiples.

Time-Depth Correlation

The most basic method of correlating between core sections and seismic profiles is to construct a time-depth plot based on a known velocity profile. This plot can then be used to determine the depth corresponding to a particular traveltime or a traveltime corresponding to a particular depth. Time-depth plots were constructed through three methods: (1) analysis of regional sonobuoy data; (2) laboratory velocity measurements through the *P*-wave logger, velocimeter (DVS) and Hamilton Frame (see "Physical Properties" section, this chapter); and (3) in-situ well-log data. This combination of techniques was required because not all holes were logged, and physical-property measurements of velocity and density were often lacking, or of poor quality because of core disturbance associated with gas in the sediments.

Sonobuoy data provide important information on overall sound-velocity structure. Houtz (1977) determined a linear regression of velocity vs. traveltime from sonobuoy solutions obtained from the western equatorial Atlantic Ocean. The velocity, V (km/s), determined for a layer at a one-way traveltime, t (s), is: $V = V_0 + kt/2$, where $V_0 = 1.740$ and $k = 1.128$. The resulting relation between depth, D (km), and two-way traveltime, T (s), is $D = C1(T1) + C2(T2)$, where $C1 = V_0/2 = 0.870$ and $C2 = k/8 = 0.141$. Thus, the linear velocity-traveltime curve can be integrated to give a quadratic time-depth relationship. In preparation for Leg 155, sonobuoy data in the vicinity of the Amazon Fan were re-evaluated (Flood, pers. comm., 1994; Fig. 16) as:

$$D = 0.871 \cdot (T) + 0.126 \cdot 10^{-4} \cdot (T)^2 \qquad (8)$$

where D is the layer depth (in m) and T is the two-way traveltime to the layer (in ms).

This revised time-depth relationship (Eq. 8) was used in this study for initial site planning and determination of drilling depths. It is similar to that originally derived by Houtz (1977), and the two formulae agree within ±1 m to 400 mbsf and differ by 3 m at 500 mbsf.

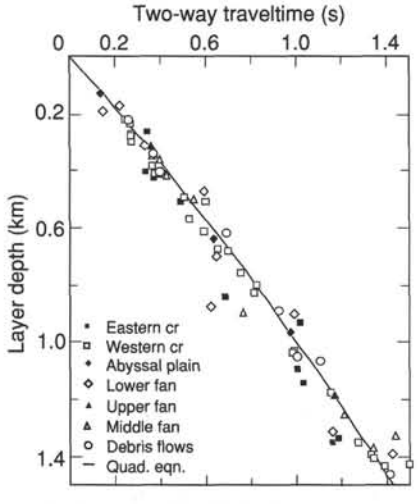

Figure 16. Time-depth relationships derived from sonobuoys collected on Amazon Fan. Separate symbols correspond to different morphologic provinces on the fan (e.g., Damuth et al., 1988), including the continental rise (cr) east and west of the fan. There is no apparent difference among the several different fan provinces. The best-fit regression line over the data corresponds to Equation 8.

Converting two-way traveltime of specific acoustic reflections to depth below seafloor permitted prediction of the depths at which distinctive seismic-facies units and reflections should be encountered prior to drilling (Table 10). Although the sonobuoy data provide a general relationship useful for planning purposes, there are many potential problems when this approach is used to determine depths to specific seismic reflections at a site. These include: (1) the lateral variability of the acoustic velocity within the sediments throughout the fan, (2) the lack of vertical resolution of sonobuoy data, and (3) the lack of sonobuoy velocity solutions for shallow depths. These factors can lead to an overall overestimation of the near-surface velocity. This velocity-depth relationship was revised based on drilling results as the leg progressed. A revised time-depth correlation, based on laboratory and downhole log velocity data at Site 931, was adopted as our working relationship early in the leg (Table 10).

Table 10. Two-way traveltime vs. sub-bottom depth determined from sonobuoy and in-situ logging data from the Amazon Fan.

Two-way traveltime (ms)	Depth* pre-Leg 155 (mbsf)	Depth Site 931 log (mbsf)
0	0	0
10	9	6
20	17	14
30	26	21
40	35	29
50	44	37
60	53	45
70	62	53
80	70	61
90	79	69
100	88	77
110	97	84
120	106	92
130	115	101
140	124	109
150	133	117
160	143	125
170	152	133
180	161	141
190	170	149
200	179	157
210	188	166
220	198	174
230	207	182
240	216	191
250	226	199
260	235	207
270	244	216
280	254	224
290	263	232
300	273	241
310	282	249
320	292	258
330	301	267
340	311	275
350	320	284
360	330	292
370	339	301
380	349	310
390	359	318
400	368	327
410	378	336
420	388	345
430	398	354
440	408	362
450	417	371
460	427	380
470	437	389
480	447	398
490	457	407
500	467	416

*$D = C1 \cdot T + C2 \cdot T^2$ (Eq. 8)
$C1 = V_D/2$; $C2 = k/8$
$V_D = 1.742$ km/s; $k = 1.008$ km/s^2

Synthetic Seismograms

Synthetic seismograms provide the best method of correlation of seismic records with borehole data. The synthetic seismograms were based on downhole sonic (LSS) and density (HLDT) data. Before producing an impedance log, we removed erroneous data points associated with cycle skips in the sonic logs and anomalously low density values. For the upper 75–100 m of each hole, where well logs were not available, we used laboratory density and velocity data. Although the laboratory data did not always produce detailed information regarding the acoustic impedance variations in the near surface sediments, they provided a means to determine the average velocity of the upper section. This helped constrain the depth of the first logged point to the traveltime in the seismic-reflection profile.

The reflection coefficient profile (*RC*) was calculated from acoustic impedance (*I*) and density profiles as a function of depth using:

$$I_i = \rho_i V_i \tag{9}$$

$$RC_i = (\rho_{i+1} V_{i+1} - \rho_i V_i) / (\rho_{i+1} V_{i+1} + \rho_i V_i) \tag{10}$$

where:

ρ_i = density of the i^{th} layer
V_i = compressional velocity of the i^{th} layer.

We convolved the reflection coefficient profile with a seismic source to produce synthetic seismograms. Seismic reflection data collected with differing acoustic sources were available at each site: (1) dual 80-in.^{3} water-gun data (*Conrad* cruise 25-14), (2) single 80-in.^{3} water-gun data (*JOIDES Resolution* Leg 155), (3) tuned 6 air-gun array (total of 1350 in.^{3}) (*Ewing* cruise 92-09), (4) single, 80-in.^{3} air-gun data (*Farnella* cruise 81-5), and (5) 3.5-kHz acoustic echograms collected during *Conrad* cruise C25-14 and during Leg 155. A source signature was obtained for each source from the digitally recorded seismic traces, and a synthetic trace was modelled and compared with the best resolution seismic-reflection data available at each site.

The 3.5-kHz echograms give a high-resolution image of the upper 50–100 m of the sediment column that cannot be resolved on the lower frequency seismic data. The 3.5-kHz data from previous cruises in the region were not recorded on tape, but some records acquired during Leg 155 were digitally recorded. Preliminary correlations between 3.5-kHz reflections (analog records) and lithologic intervals were attempted during the leg using time-depth relationships derived from laboratory measurements. Post-cruise analysis of the digitally recorded 3.5-kHz echograms and correlation to recovered cores will be required to understand the nature of reflection patterns and their implications for recent fan sedimentation.

Seismic Facies Classification

Where imaged on seismic-reflection profiles, many of the various architectural features and acoustic units of Amazon Fan are bounded by prominent reflecting horizons and are characterized internally by a variety of distinctive groups or "packages" of reflection patterns. Each discrete package of reflection patterns within a fan feature or acoustic unit is termed a seismic facies. Seismic facies are normally identified and classified on the basis of their internal reflection character and their external form or shape. Mitchum et al. (1977) developed a comprehensive classification for seismic facies as observed on multi-fold seismic data. The seismic-facies classification utilized in this volume (Fig. 17) was developed by J.E. Damuth through modification of Mitchum et al.'s (1977) classification in an attempt to simplify their original classification and alleviate the following problems:

1. The Mitchum et al. (1977) classification mixes non-genetic descriptive terms for both internal reflection character and external form of seismic facies with terms that imply genetic interpretations of depositional environments. Genetic terms such as fan, fan complex, contourite mound, channel fill, sheet drape, and slump are interpretations of particular depositional environments and processes. Such genetic terms should be avoided because particular seismic facies can be representative of more than one depositional environment or process. The revised classification (Fig. 17) is restricted to non-genetic, descriptive terms that clearly describe the internal reflection character (e.g., parallel, hummocky, contorted) and external form or geometry (e.g., wedge, mound) of the seismic facies.
2. The Mitchum et al. (1977) classification is somewhat confusing in terms of organization of various terms and headings. For example, some modifying terms for reflection configurations such as hummocky, lenticular, contorted, etc. seem equivalent to other principal classifications of reflection configurations such as parallel, subparallel, divergent, etc. and should be elevated to that stature in the classification. Other terms of the classification (including all genetic terms referred to in (1) above) seem unnecessary or redundant, and are eliminated from the revised classification for the sake of simplicity and improved organization.

In the classification presented in Figure 17, the terminology of Mitchum et al. (1977) has been retained wherever possible. Seismic facies are classified on the basis of internal reflection character and external form.

Internal Reflection Character

The internal reflection character of a seismic facies can be described by three parameters: (1) reflection configuration describes the geometric pattern, relationship and attitude of individual reflections to one another within the seismic facies; (2) reflection continuity describes the general continuity of individual reflections throughout the seismic facies; and (3) reflection amplitude describes the general range of amplitudes predominantly exhibited by the reflections throughout the seismic facies.

Reflection Configuration

1. Parallel: All reflections are essentially parallel to one another. Parallel configurations can be further described on the basis of orientation or attitude of reflections into horizontal, inclined or undulating (These modifying terms can also be applied to some of the following terms).
2. Subparallel: Individual reflections are subparallel to one another and converge and/or diverge from one another in a regular to random manner to form various configurations or geometries. Three subtypes of subparallel reflections are recognized:
   a. Clinoforms are groups of regular, laterally repeated, inclined reflections that generally converge downward and/or upward toward the lateral limits of the facies. Several subtypes of clinoform patterns have been recognized including sigmoid, oblique, parallel, shingled, and complex. These various types and their depositional significance are discussed in detail in Mitchum et al. (1977).
   b. Regular migrating are groups of superposed wave-shaped reflections that show regular, periodic convergence and divergence between individual reflections; each reflection is progressively offset laterally from the adjacent reflection resulting in a reflection pattern resembling migrating waves.

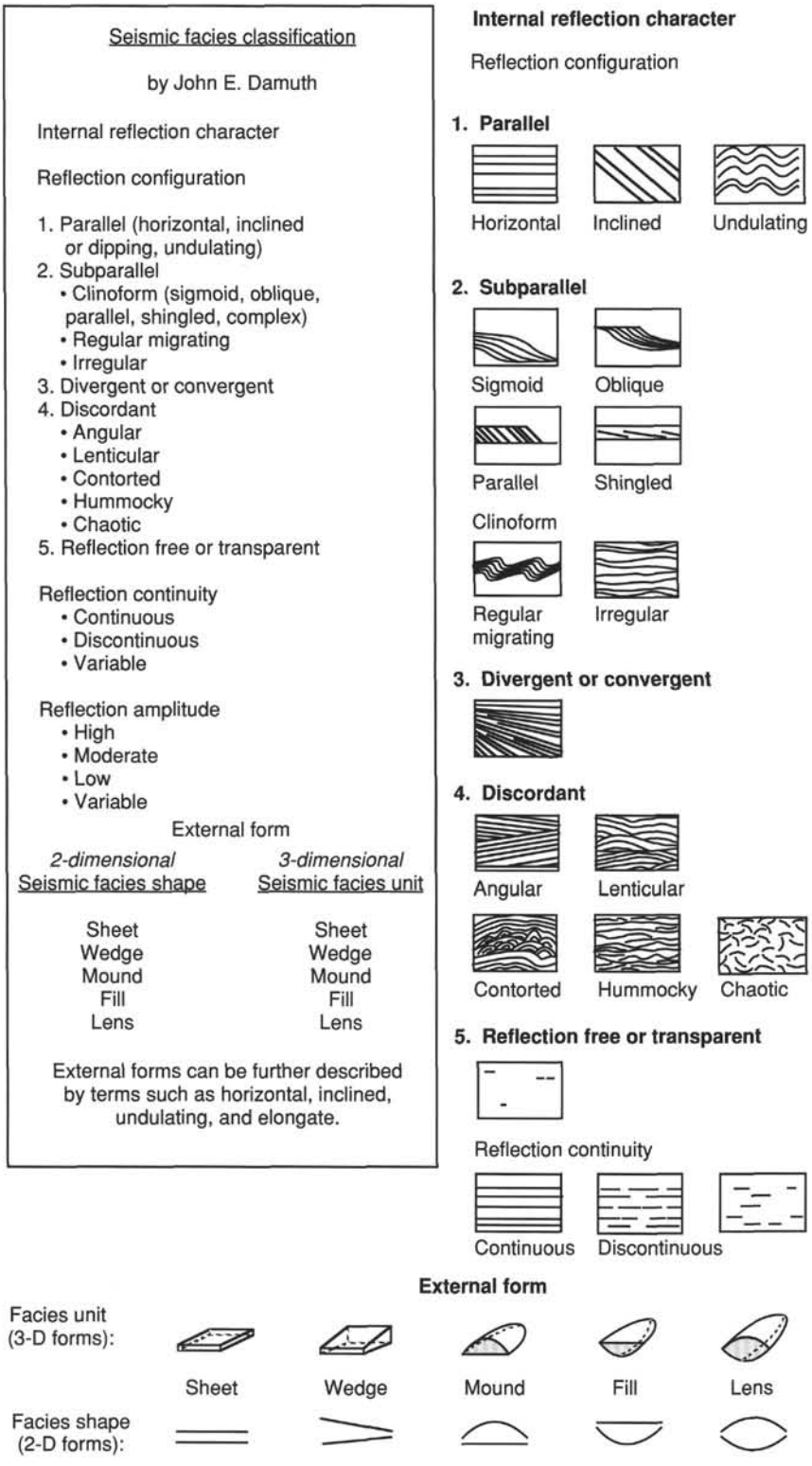

Figure 17. Classification of seismic facies used in this volume. This classification is a modified version of the seismic-facies classification of Mitchum et al. (1977).

c. Irregular groups of reflections have individual reflections that randomly converge and diverge in relation to adjacent reflections. These convergence/divergence patterns range from random to nearly regular, at which point they grade into regular migrating patterns.

3. Divergent or convergent: Most or all individual reflections progressively diverge (or conversely, converge) in a single direction within the facies. The number of individual reflections may increase in the direction of divergence. Conversely, nonstrategic lateral termination of some reflections occur in the direction of convergence. Seismic facies within channel-levee systems on the Amazon Fan are classified as divergent if reflections diverge toward the channel axis and convergent if they converge toward the channel axis.

4. Discordant: Individual reflections or groups of reflections are oriented at various (usually acute) angles to one another, and commonly terminate against one another by apparent onlap, downlap, or truncation. Five subtypes of discordant reflections are recognized and form a spectrum of reflection patterns that are gradational from well organized to very disorganized or random.
   a. Angular: Individual or groups of essentially parallel, relatively continuous reflections that are oriented at various angles and terminate against one another by apparent truncation, onlap, or downlap.
   b. Lenticular: Somewhat similar to angular, but individual or groups of reflections form broad, gentle convex-upward or lens-shaped patterns that onlap, downlap, or terminate against one another.
   c. Contorted: Individual or groups of reflections form tight, generally convex-upward or lens-shaped patterns that downlap, onlap, or terminate against one another. These patterns are somewhat similar to lenticular, but are much more common, random, and disorganized, and often present a convoluted appearance.
   d. Hummocky: Irregular discontinuous undulating reflections that form practically random, disorganized hummocky patterns marked by nonsystematic reflection terminations and splits. Relief on individual undulations or hummocks is low, commonly approaching the limits of seismic resolution.
   e. Chaotic: Individual reflections are short, discontinuous and randomly oriented with respect to one another giving a disordered, random appearance to the overall reflection pattern.
5. Reflection free or transparent: Acoustically transparent facies in which individual or groups of reflections are essentially absent throughout. Individual reflections may rarely occur, but are of extremely short lateral extent and commonly low amplitude.

Reflection Continuity

1. Continuous: Most individual reflections are continuous or unbroken throughout the facies.
2. Discontinuous: Individual reflections are discontinuous or broken and are only intermittently present throughout the facies. If individual reflections become infrequent to rare and of very short lateral extent, then the facies would be classified as reflection free or transparent (see 5 above).
3. Variable: A range or gradation of reflection continuity occurs throughout the facies (Note: commonly a more specific range of continuity can be stated; i.e., continuous to discontinuous, discontinuous to reflection free).

Reflection Amplitude

The amplitudes of individual reflections or groups of reflections can be classified as high, moderate or low amplitude. Large and frequent changes in amplitude within the facies, or within an individual reflection, can be classified as variable, although a more specific range can often be stated (for example, moderate-to-high amplitude or high-to-low amplitude).

External Form

External form describes the external geometry or shape of the upper and lower boundaries of a seismic facies in both two and three dimensions. A two-dimensional external form is termed a seismic facies shape (i.e., a seismic facies observed on an individual seismic line), whereas, a three-dimensional external form is termed a Seismic-facies Unit (i.e., a seismic facies mapped throughout a grid of seismic lines), thereby retaining the original definition of Mitchum et al. (1977). However, the same name is used for both a seismic-facies shape and its equivalent seismic-facies unit to minimize the terminology (Fig. 17).

1. Sheet: The upper and lower boundaries are essentially parallel. The seismic-facies unit has boundaries that are parallel in all directions. Thus, a sheet represents a deposit of uniform thickness throughout its lateral extent.
2. Wedge: The upper and lower boundaries progressively converge and the facies thins in one direction, thus presenting a wedge-shaped appearance in two dimensions. The seismic-facies unit is essentially a wedge-shaped deposit that thins in one or more directions.
3. Mound: The upper boundary is convex upward and the lower boundary is essentially horizontal or flat. The seismic-facies unit is a lobate-shaped deposit that is convex-upward in all directions.
4. Fill: The upper boundary is essentially horizontal or flat and the lower boundary is convex downward. The seismic-facies unit represents a deposit that has essentially a convex-downward shape in most directions.
5. Lens: The upper boundary is convex upward and the lower boundary is convex downward, thus presenting a lens-shaped appearance. The seismic-facies unit represents a deposit that thins laterally outward in all directions.

Various orientations, attitudes, and irregularities of shape associated with seismic-facies shapes and units can be further described by modifying terms such as horizontal, inclined, undulating, and elongate.

IN-SITU TEMPERATURE MEASUREMENTS

Introduction

In-situ temperature measurements are important for assessing the stability field of potential gas hydrates and characterizing the environment of early diagenesis. For all but two Leg 155 sites, temperature gradients and heat flow were determined downhole from ADARA and WSTP measurements.

Water Sampler Temperature Probe (WSTP) Temperature Measurements

The WSTP provides downhole temperature measurements in sediment not yet affected by mechanical drilling disturbance or borehole fluid circulation. The WSTP tools aboard the *JOIDES Resolution* are based on the Uyeda temperature tool (Yokota et al., 1980). Two forms of the tool are available. One includes a Barnes fluid sampler (Barnes, 1979), the other measures temperature only.

The current WSTP probe includes a stainless-steel temperature-probe tip, which is pushed ahead of the bit into the undisturbed sediments at the bottom of the hole. This tip has a minimum diameter of 1.3 cm (Fig. 18; Table 11). During Leg 139, a 2.7-cm-diameter sleeve was fabricated to fit over the temperature probe for use when only temperatures were needed from the instrument. This sleeve is run instead of the filter assembly to reduce the time constant of the probe and improve the geometry of the measurement so that (1) the frictional heat pulse associated with insertion of the probe can be assumed to approximate more closely a line source of heat, and (2) insertion of the instrument is less likely to disturb or fracture semi-lithified sediments.

The WSTP is mounted in a standard coring barrel, with a narrow stainless-steel probe extending 1.1 m beyond the end of the barrel (Fig. 18). The probe contains the thermistor used during temperature

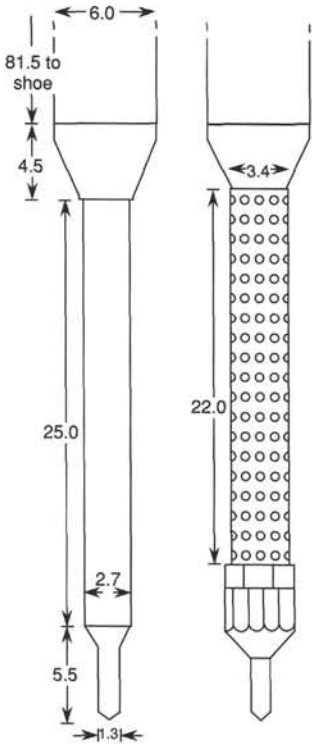

Figure 18. Scale plan drawings of the WSTP probe assembly, configured for temperature only (left diagram), and for temperature and water sampling (right diagram). All dimensions are in centimeters. The probe tips extend 1.1 m ahead of the bit when latched in place.

measurements, as well as the filtering system for obtaining the pore-fluid sample in the version of the tool that includes the Barnes fluid sampler. In operation, the WSTP is lowered down the drill pipe by wireline while the drill bit is held slightly off the bottom of the hole. The WSTP is held at the mud line for 10 to 15 min to allow the probe to equilibrate with bottom-water temperatures. The tool is then lowered to the bottom of the drill string, where it is latched into place with the probe extending through the center of the drill bit. The drill string is then lowered, forcing the probe into the bottom-hole sediments. Temperature is measured by the WSTP and recorded every 4.369 s (Table 11). A colleted delivery system allows the probe to retract up inside the bit if the formation is too hard for penetration. With an APC/XCB bottom-hole assembly, the bit can be decoupled from the tool after penetration so that the probe will not be disturbed by drill-string heave. The driller can continuously circulate fluid if necessary to keep the hole clear of fill, as circulation of cold bottom water in the hole will have little influence on measured temperatures at times less than a few hours after drilling, as long as the probe penetrates at least 50 cm (Fisher and Hounslow, 1990).

Table 11. Specifications of temperature measurement instruments used during Leg 155.

Tool	Thermistor housing	Sensor recording, resolution interval	Accuracy
APC tool (ADARA)	Steel annular cylinder OD: 0.0907 m ID: 0.0617 m	0.01°C programmable, generally 5 s	±0.04°C
WSTP	Steel cylindrical probe OD: 0.0127 m	0.01°C, 4.369 s	±0.1°C

Notes: OD = outer diameter, ID = inner diameter.

In practice, equilibrium formation temperatures are never reached because the thermal state of the tool and the formation are disturbed by insertion of the probe. The period required for the sediments and probe to equilibrate is prohibitively long, so the steady-state temperature must be estimated by extrapolating the transient thermal signal recorded by the probe (Fig. 19). During Leg 155, equilibrium temperatures were estimated from approximately 15-min records of the transient temperature. An updated version of the thermal data processing software first used on Leg 146 was used for routinely estimating the equilibrium temperature.

Several potential sources of error contribute to limiting the accuracy of the equilibrium temperature estimated from the WSTP data. First, heating of the probe on insertion is not instantaneous as the processing software assumes. Because the time of insertion is not known with great precision, the duration of the transient thermal signal is uncertain. In practice, this problem was resolved by applying an empirical time shift to the thermal data to best fit the theoretical transient response functions of Bullard (1954). Second, the relatively short length of the narrow probe appears to allow only a few minutes of undisturbed measurements before a thermal disturbance is conducted down from the larger-diameter section above, limiting the accuracy of temperature extrapolations to about ±0.1°–0.2°C. In addition, because of its relative size and geometry, probe calibration is difficult, and, consequently, only the thermistors can be calibrated, not the entire instrument. An offset (different for each run) usually needs to be applied to the resistance of WSTP thermistors to be consistent with temperatures obtained from ADARA (see next section). Because the exact depth of penetration of the tool is never known, all temperatures measured with the WSTP must be considered lower bounds on in-situ conditions. From the shape of the temperature-time records and comparison with nearby measurements it is often possible to determine if the tool was pressed into fill at the bottom of a hole or if the formation cracked upon insertion. A review of thermal data obtained with this type of probe during the Deep Sea Drilling Project (DSDP) is given by Hyndman et al. (1987).

APC Tool (ADARA) Temperature Measurements

The advanced piston corer heat-flow coring shoe (ADARA) was used to obtain in-situ sediment temperatures during regular piston-coring operations. The instrument contains an electronics section, composed of three circuit boards and two battery packs, built into a cylindrical frame. These components of the thermal tool fit inside an annular cavity of a special APC coring shoe. Two steel prongs extend from the base of the frame and anchor the electronics in place inside the shoe. Inside one of the two prongs is a platinum resistance-temperature device (RTD), which has been calibrated over a range of –20° to 100°C, with resolution of 0.01°C. Tools used during Leg 155 were calibrated at Woods Hole Oceanographic Institution (WHOI) in April 1993. The platinum sensor records temperature measurements during coring. The tool is programmed after it has been inserted into the coring shoe, and repeated deployments can be run without removing the tool or batteries. After programming and starting the test sequence, a crossover subassembly with o-rings seals the cavity containing the electronics.

In operation, the coring shoe is mounted on a core barrel and lowered down the pipe by wireline. The tool is typically held for 5 to 10 min at the mud line to equilibrate with the bottom temperature, and then lowered to the end of the drill string. Standard APC coring techniques are used, with the core barrel being fired out through the drill bit using hydraulic pressure. The tool is then left in place for 10 min, so that the tool can begin thermal equilibration with the formation. During Leg 155, the ADARA collected temperature measurements at 5-s intervals over a 10-min period (Table 11). This provided a sufficiently long transient record for reliable extrapolation of the steady-state temperature. Processing of the temperature measurements is similar to that for the WSTP tool, and is described in the next section.

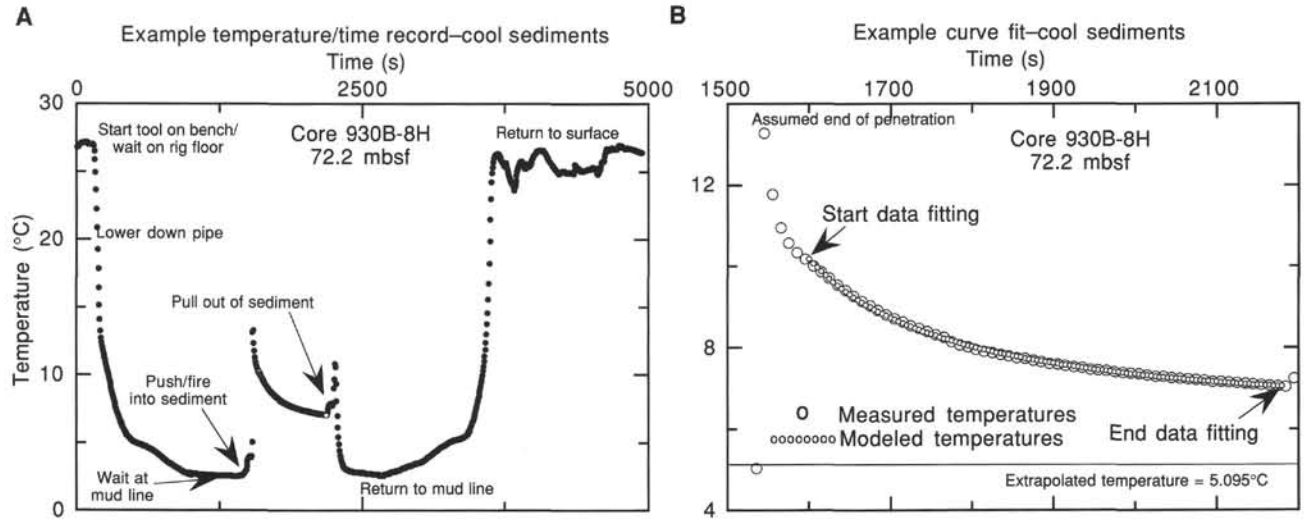

Figure 19. Examples of temperature/time and curve-fit records. **A.** A good temperature/time record for a measurement in relatively cool sediments. The heat pulse resulting from insertion of the probe is clearly visible. The WSTP probe is pushed into the sediments, while the APC tool is fired in along with a core barrel. **B.** Measured and modeled temperatures from the same run as in (A). The modeled temperature curve extrapolates to 5.095°C.

The nominal accuracy of the unreduced temperature measurements is estimated to be 0.1°C.

Data Reduction

Although the WSTP and ADARA tools have different geometries, the methods used for analysis of recovered temperature data are similar. The data reduction method for both tools estimates the steady-state bottom-hole temperature by forward modeling the recorded transient temperature curve as a function of time. The shape of the transient temperature curve is determined by the response function of the tool and the thermal properties of the bottom-hole sediments (Bullard, 1954; Horai and Von Herzen, 1985). For both instruments, synthetic curves are constructed based on tool geometry, sampling interval, and the thermal properties of the tools and surrounding sediments. Both tools have thermal time constants of several minutes under normal conditions, requiring that the probes be kept on bottom for at least 10–15 min to allow extrapolation of the temperature curves with confidence. In general, temperature increases immediately following emplacement of the probe, as a result of frictional heating of the probe tip during insertion. The temperature peaks after a short period and decreases monotonically thereafter, approaching the steady-state temperature of the sediments at a rate inversely proportional to time.

The theoretical decay curves simulate the instantaneous heating (or cooling) of the sediment following probe penetration, but in practice a finite time is required for the sensors to reach a maximum temperature. As a result, the effective origin time of the thermal pulse is delayed as a function of tool and sediment properties. In addition, the recorders sample temperatures at fixed intervals, leaving the exact penetration time uncertain. An effective penetration time and an extrapolated temperature are estimated by shifting the time axis of the theoretical thermal decay curves to fit the actual data. Temperatures from the first 5–10 measurements (20–50 s) following penetration commonly do not follow the theoretical curves, but later parts of the records usually provide a very good match (Fig. 19). The choice of which data should be included in the matching, and which time shift should be used, is partly subjective; it is probably best to use as much of the actual decay curve as possible. The variations in extrapolated temperatures that result from choosing different time intervals and time shifts can be used to estimate errors associated with the temperatures finally assigned to represent in-situ conditions.

Data reduction software developed by ODP was used during Leg 155 to interactively model the transient temperature curve and extrapolate for the equilibrium temperature. Variables in the modeling method are the thermal conductivity of the sediments, tool insertion time, delay time between tool insertion and peak temperature, and the length of the portion of the curve to be fitted. In practice, relatively few iterations of the modeling procedure were required to obtain reasonable fits to the temperature data.

Sediment thermal conductivities were derived from laboratory physical properties measurements from Sites 930, 931, and 935. The thermal conductivity values were used in a regression of thermal conductivity with depth to estimate at each site the conductivity at the maximum depth for which temperature was measured. Separate regression estimates were determined for Sites 930, 931, and 935 and averaged to obtain the thermal conductivity used in temperature calculations. The shipboard thermal conductivity measurements were consistent with the modeling and produced reliable equilibrium temperatures.

Equilibrium temperatures were plotted as a function of depth (mbsf) to determine the geothermal temperature gradient. Where several temperature determinations were made, the gradient was found to be nonlinear, increasing with depth. We calculated heat flow by adopting a constant geothermal temperature gradient and a linear increase in thermal conductivity. These heat flow estimates should be treated with caution, because the geothermal gradient is probably not linear, heat transfer can take place also by convection (such as pore-fluid advection), and nonlinear variations in temperature with depth can vary depending on fluid advection processes and relative changes in the medium that the heat passes through (Carslaw and Jaeger, 1959; Menke and Abbott, 1990).

REFERENCES*

Absy, M.L., 1979. A palynological study of Holocene sediments in the Amazon Basin [Ph.D. thesis]. Univ. of Amsterdam, The Netherlands.

Archie, G.E., 1942. The electrical resistivity log as an aid in determining some reservoir characteristics. *J. Pet. Tech.*, 5:1–8.

*Abbreviations for names of organizations and publications in ODP reference lists follow the style given in *Chemical Abstracts Service Source Index* (published by American Chemical Society).

Barnes, R.O., 1979. Operation of the IPOD in-situ pore water sampler [Introduction and explanatory notes]. *In* Sibuet, J.-C., Ryan, W.B.F., et al., *Init. Repts. DSDP,* 47 (Pt. 2): Washington (U.S. Govt. Printing Office), 19–22.

Barron, J.A., 1985a. Late Eocene to Holocene diatom biostratigraphy of the equatorial Pacific Ocean, Deep Sea Drilling Project Leg 85. *In* Mayer, L., Theyer, F., Thomas, E., et al., *Init. Repts. DSDP,* 85: Washington (U.S. Govt. Printing Office), 413–456.

Barron, J.A., 1985b. Miocene to Holocene planktic diatoms. *In* Bolli, H.M., Saunders, J.B., and Perch-Nielsen, K. (Eds.), *Plankton Stratigraphy:* Cambridge (Cambridge Univ. Press), 763–809.

Bé, A.W.H., 1977. An ecological, zoogeographic and taxonomic review of Recent planktonic foraminifera. *In* Ramsay, A.T.S. (Ed.), *Oceanic Micropaleontology* (Vol. 1): London (Academic Press), 1–100.

Becker, K., Sakai, H., et al., 1988. *Proc. ODP, Init. Repts.,* 111: College Station, TX (Ocean Drilling Program).

Berggren, W.A., Kent, D.V., Flynn, J.J., and Van Couvering, J.A., 1985. Cenozoic geochronology. *Geol. Soc. Am. Bull.,* 96:1407–1418.

Blow, W.H., 1969. Late middle Eocene to Recent planktonic foraminiferal biostratigraphy. *In* Brönniman, P., and Renz, H.H. (Eds.), *Proc. First Int. Conf. Planktonic Microfossils, Geneva, 1967:* Leiden (E.J. Brill), 1:199–422.

Bolli, H.M., and Saunders, J.B., 1985. Oligocene to Holocene low latitude planktonic foraminifera. *In* Bolli, H.M., Saunders, J.B., and Perch-Nielsen, K. (Eds.), *Plankton Stratigraphy:* Cambridge (Cambridge Univ. Press), 155–262.

Bouma, A.H., 1962. *Sedimentology of Some Flysch Deposits: A Graphic Approach to Facies Interpretation:* Amsterdam (Elsevier).

Boyce, R.E., 1976. Definitions and laboratory techniques of compressional sound velocity parameters and wet-water content, wet-bulk density, and porosity parameters by gravimetric and gamma ray attenuation techniques. *In* Schlanger, S.O., Jackson, E.D., et al., *Init. Repts. DSDP,* 33: Washington (U.S. Govt. Printing Office), 931–958.

Bray, E.E., and Evans, E.D., 1961. Distribution of *n*-paraffins as a clue to recognition of source beds. *Geochim. Cosmochim. Acta,* 22:2–15.

Bukry, D., 1973. Low-latitude coccolith biostratigraphic zonation. *In* Edgar, N.T., Saunders, J.B., et al., *Init. Repts. DSDP,* 15: Washington (U.S. Govt. Printing Office), 685–703.

Bukry, D., 1975. Coccolith and silicoflagellate stratigraphy, northwestern Pacific Ocean, Deep Sea Drilling Project Leg 32. *In* Larson, R.L., Moberly, R., et al., *Init. Repts. DSDP,* 32: Washington (U.S. Govt. Printing Office), 677–701.

Bukry, D., 1978. Biostratigraphy of Cenozoic marine sediment by calcareous nannofossils. *Micropaleontology,* 24:44–60.

Bukry, D., 1980. Opal phytoliths from the tropical eastern Pacific Ocean, Deep Sea Drilling Project Leg 54. *In* Rosendahl, B.R., Hekinian, R., et al., *Init. Repts. DSDP,* 54: Washington (U.S. Govt. Printing Office), 575–589.

Bullard, E.C., 1954. The flow of heat through the floor of the Atlantic Ocean. *Proc. R. Soc. London A,* 222:408–429.

Burckle, L.H., 1977. Pliocene and Pleistocene diatom datum levels from the equatorial Pacific. *Quat. Res.,* 7:330–340.

Burckle, L.H., Keigwin, L.D., and Opdyke, N.D., 1982. Middle and late Miocene stable isotope stratigraphy: correlation to the paleomagnetic reversal record. *Micropaleontology,* 28:329–334.

Cande, S.C., and Kent, D.V., 1992. A new geomagnetic polarity time scale for the Late Cretaceous and Cenozoic. *J. Geophys. Res.,* 97:13917–13951.

Carlson, R.L., and Christensen, N.I., 1979. Velocity anisotropy in semi-indurated calcareous deep-sea sediments. *J. Geophys. Res.,* 84:205–211.

Carslaw, H.S., and Jaeger, J.C., 1959. *Conduction of Heat in Solids* (2nd ed.): Oxford (Clarendon Press).

Chaisson, W.P., and Leckie, R.M., 1993. High-resolution Neogene planktonic foraminifer biostratigraphy of Site 806, Ontong Java Plateau (western equatorial Pacific). *In* Berger, W.H., Kroenke, L.W., Mayer, L.A., et al., *Proc. ODP, Sci. Results,* 130: College Station, TX (Ocean Drilling Program), 137–178.

Colinvaux, P.A., 1989. Forest palaeoecology: ice-age Amazon revisited. *Nature,* 340:188–189.

Cook, H.E., Johnson, P.D., Matti, J.C., and Zemmels, I., 1975. Methods of sample preparation and X-ray diffraction data analysis, X-ray Mineralogy Laboratory, Deep Sea Drilling Project, University of California, Riverside. *In* Hayes, D.E., Frakes, L.A., et al., *Init. Repts. DSDP,* 28: Washington (U.S. Govt. Printing Office), 999–1007.

Damuth, J.E., 1977. Late Quaternary sedimentation in the western equatorial Atlantic. *Geol. Soc. Am. Bull.,* 88:695–710.

Damuth, J.E., Flood, R.D., Kowsmann, R.O., Belderson, R.H., and Gorini, M.A., 1988. Anatomy and growth pattern of Amazon deep-sea fan as revealed by long-range side-scan sonar (GLORIA) and high-resolution seismic studies. *AAPG Bull.,* 72:885–911.

Damuth, J.E., Kowsmann, R.O., Flood, R.D., Belderson, R.H., and Gorini, M.A., 1983. Age relationships of distributary channels on Amazon deep-sea fan: implications for fan growth pattern. *Geology,* 11:470–473.

Dubuisson, G., de Menocal, P., and Bristow, J., in press a. Comparison of susceptibility logs with classical logs: relation with lithology. *Proc. ODP, Sci. Results,* 145: College Station, TX (Ocean Drilling Program).

Dubuisson, G., Thibal, J., Pozzi, J.-P., Barthes, V., and Pocachard, J., in press b. Downhole magnetostratigraphy at Site 884: comparison with core results. *Proc. ODP, Sci. Results,* 145: College Station, TX (Ocean Drilling Program).

Ekstrom, M.P., Dahan, C.A., Chen, M.-Y., Lloyd, P.M., and Rossi, D.J., 1986. Formation imaging with microelectrical scanning arrays. *Trans. SPWLA Annu. Logging Symp.,* 27:Pap. BB.

Ellis, D.V., 1987. *Well Logging For Earth Scientists:* New York (Elsevier).

Emeis, K.-C., and Kvenvolden, K.A., 1986. Shipboard organic geochemistry on *JOIDES Resolution. ODP Tech. Note,* 7.

Ericson, D.B., 1961. Pleistocene climatic record in some deep-sea sediment cores. *Ann. N.Y. Acad. Sci.,* 95:537–541.

Ericson, D.B., Ewing, M., Wollin, G., and Heezen, B.C., 1961. Atlantic deep-sea sediment cores. *Geol. Soc. Am. Bull.,* 72:193–286.

Ericson, D.B., and Wollin, G., 1968. Pleistocene climates and chronology in deep-sea sediments. *Science,* 162:1227–1234.

Espitalié, J., Laporte, J.L., Leplat, P., Madec, M., Marquis, F., Paulet, J., and Boutefeu, A., 1977. Méthode rapide de caractérisation des roches mères, de leur potentiel pétrolier et de leur degré d'évolution. *Rev. Inst. Fr. Pet.,* 32:23–42.

Fisher, A. and Hounslow, M., 1990. Heat flow through the toe of the Barbados accretionary complex. *In* Moore, J.C., Mascle, A., Taylor, E. (Eds.), *Proc. ODP, Sci. Results,* 110, College Station, TX (Ocean Drilling Program), 345–363.

Flood, R.D., Manley, P.L., Kowsmann, R.O., Appi, C.J., and Pirmez, C., 1991. Seismic facies and late Quaternary growth of Amazon submarine fan. *In* Weimer, P., and Link, M.H. (Eds.), *Seismic Facies and Sedimentary Processes of Submarine Fans and Turbidite Systems:* New York (Springer-Verlag), 415–433.

Folk, R.L., 1980. *Petrology of Sedimentary Rocks* (2nd ed.): Austin, TX (Hemphill Publ.).

Gartner, S., 1977. Calcareous nannofossil biostratigraphy and revised zonation of the Pleistocene. *Mar. Micropaleontol.,* 2:1–25.

Germeraad, J.H., Hopping, C.A., and Müller, J., 1968. Palynology of Tertiary sediments from tropical areas. *Rev. Palaeobot. Palynol.,* 6:189–348.

Gieskes, J.M., Gamo, T., and Brumsack, H.J., 1991. Chemical methods for interstitial water analysis aboard *JOIDES Resolution. ODP Tech. Note,* 15.

Gillis, K., Mével, C., Allan, J., et al., 1993. *Proc. ODP, Init. Repts.,* 147: College Station, TX (Ocean Drilling Program).

Grau, J.A., and Schweitzer, J.S., 1989. Elemental concentrations from thermal neutron capture gamma-ray spectra in geological formations. *Nucl. Geophys.,* 3:1–9.

Grau, J.A., Schweitzer, J.S., and Hertzog, R.C., 1990. Statistical uncertainties of elemental concentrations extracted from neutron induced gamma-ray measurements. *IEEE Trans. Nucl. Sci.,* 37:2175–2178.

Hamilton, E.L., 1971. Prediction of in-situ acoustic and elastic properties of marine sediments. *Geophysics,* 36:266–284.

Harland, W.B., Armstrong, R.L., Cox, A.V., Craig, L.E., Smith, A.G., and Smith, D.G., 1990. *A Geologic Time Scale 1989:* Cambridge (Cambridge Univ. Press).

Harris, S., Hagelberg, T., Mix, A., Pisias, N., and Shackleton, N.J., in press. Sediment depths determined by comparisons of GRAPE and logging density data during Leg 138. *In* Pisias, N.G., Mayer, L.A., Janecek, T.R., Palmer-Julson, A., and van Andel, T.H. (Eds.), *Proc. ODP, Sci. Results,* 138: College Station, TX (Ocean Drilling Program).

Hertzog, R., Colson, L., Seeman, B., O'Brien, M., Scott, H., McKeon, D., Wraight, J., Grau, J., Ellis, D., Schweitzer, J., and Herron, M., 1989. Geochemical logging with spectrometry tools. *SPE Form. Eval.,* 4:153–162.

Hiscott, R.N., Colella, A., Pezard, P., Lovell, M.A., and Malinverno, A., 1992. Sedimentology of deep-water volcaniclastics, Oligocene Izu-Bonin

forearc basin, based on formation microscanner images. *In* Taylor, B., Fujioka, K., et al., *Proc. ODP, Sci. Results,* 126: College Station, TX (Ocean Drilling Program), 75–96.

Hoppie, B.W., Blum, P., and the Shipboard Scientific Party, 1994. Natural gamma-ray measurements on ODP cores: introduction to procedures with examples from Leg 150. *In* Mountain, G.S., Miller, K.G., Blum, P., et al., *Proc. ODP, Init. Repts.,* 150: College Station, TX (Ocean Drilling Program), 51–59.

Horai, K., and Von Herzen, R.P., 1985. Measurement of heat flow on Leg 86 of the Deep Sea Drilling Project. *In* Heath, G.R., Burckle, L.H., et al., *Init. Repts. DSDP,* 86: Washington (U.S. Govt. Printing Office), 759–777.

Houtz, R.E., 1977. Sound velocity characteristics of sediment from eastern South American margin. *Geol. Soc. Am. Bull.,* 88:720–722.

Hyndman, R.D., Langseth, M.G., and Von Herzen, R.P., 1987. Deep Sea Drilling Project geothermal measurements: a review. *Rev. Geophys.,* 25:1563–1582.

Imbrie, J.M., Hays, J.D., Martinson, D.G., McIntyre, A., Mix, A.C., Morley, J.J., Pisias, N.G., Prell, W.L., and Shackleton, N.J., 1984. The orbital theory of Pleistocene climate: support from a revised chronology of the marine ^{18}O record. *In* Berger, A., Imbrie, J., Hays, J., Kukla, G., and Saltzman, B. (Eds.), *Milankovitch and Climate* (Pt. 1): Dordrecht (D. Reidel), 269–305.

Ingram, R.L., 1954. Terminology for the thickness of stratification units and parting units in sedimentary rocks. *Geol. Soc. Am. Bull.,* 65:937–938.

Jansen, E., and Veum, T., 1990. Evidence for two-deglaciation and its impact on North Atlantic deep-water circulation. *Nature,* 343:612–616.

JOIDES PPSP, 1992. Ocean Drilling Program guidelines for pollution prevention and safety. *JOIDES J.,* 18.

Kolbe, R.W., 1955. Diatoms from equatorial Atlantic cores. *Rep. Swed. Deep-sea Exped., 1947–1948,* 7:149–184.

Kolla, V., and Perlmutter, M.A., 1993. Timing of turbidite sedimentation on the Mississippi Fan. *AAPG Bull.,* 77:1129.

Kvenvolden, K.A., and McDonald, T.J., 1986. Organic geochemistry on the *JOIDES Resolution*—an assay. *ODP Tech. Note,* 6.

Lock, G.A., and Hoyer, W.A., 1971. Natural gamma-ray spectral logging. *Log Analyst,* 12:3–9.

Lorente, M.A., 1986. Palynology and palynofacies of the Upper Tertiary in Venezuela. *Diss. Bot.* (Vol. 99): Berlin (J. Cramer).

Manheim, F.T., and Sayles, F.L., 1974. Composition and origin of interstitial waters of marine sediments based on deep sea drill cores. *In* Goldberg, E.D. (Ed.), *The Sea* (Vol. 5): New York (Wiley Interscience), 527–568.

Mankinen, E.A., and Dalrymple, G.B., 1979. Revised geomagnetic polarity time scale for the interval 0–5 m.y.B.P. *J. Geophys. Res.,* 84:615–626.

Mankinen, E.A., Donnelly, J.M., and Grommé, C.S., 1978. Geomagnetic polarity event recorded at 1.1 m.y. B.P. on Cobb mountain, Clear Lake volcanic field, California. *Geology,* 6:653–656.

Manley, P.L., and Flood, R.D., 1988. Cyclic sediment deposition within Amazon Deep-Sea Fan. *AAPG Bull.,* 72:912–925.

Martini, E., 1971. Standard Tertiary and Quaternary calcareous nannoplankton zonation. *In* Farinacci, A. (Ed.), *Proc. 2nd Int. Conf. Planktonic Microfossils Roma:* Rome (Ed. Tecnosci.), 2:739–785.

Martinson, D.G., Pisias, N.G., Hays, J.D., Imbrie, J., Moore, T.C., Jr., and Shackleton, N.J., 1987. Age dating and the orbital theory of the ice ages: development of a high-resolution 0 to 300,000-year chronostratigraphy. *Quat. Res.,* 27:1–29.

Maslin, M.A., 1993. Palaeoceanography of the Northeast Atlantic in the late Pleistocene [Ph.D. thesis]. Cambridge Univ., Cambridge, U.K.

Mayer, L.A., 1979. The origin of fine scale acoustic stratigraphy in deep-sea carbonates. *J. Geophys. Res.,* 84:6177–6184.

McGeary, D.F.R., and Damuth, J.E., 1973. Postglacial iron-rich crusts in hemipelagic deep-sea sediment. *Geol. Soc. Am. Bull.,* 84:1201–1212.

Menke, W., and Abbott, D., 1990. *Geophysical Theory:* New York (Columbia Univ. Press).

Mix, A.C., Rugh, W., Pisias, N.G., Veirs, S., Leg 138 Shipboard Sedimentologists (Hagelberg, T., Hovan, S., Kemp, A., Leinen, M., Levitan, M., Ravelo, C.), and Leg 138 Scientific Party, 1992. Color reflectance spectroscopy: a tool for rapid characterization of deep-sea sediments. *In* Mayer, L., Pisias, N., Janecek, T., et al., *Proc. ODP, Init. Repts.,* 138 (Pt. 1): College Station, TX (Ocean Drilling Program), 67–77.

Mitchum, R.M., Vail, P.R., and Sangree, J.B., 1977. Stratigraphic interpretation of seismic reflection patterns in depositional sequences. *In* Payton, C.E. (Ed.), *Seismic Stratigraphy—Applications to Hydrocarbon Exploration.* AAPG Mem., 26:117–134.

Moore, D.M., and Reynolds, R.C., Jr., 1989. *X-ray Diffraction and the Identification and Analysis of Clay Minerals:* New York (Oxford Univ. Press).

Muller, J., Di Giacomo, E., and Van Erve, A.W., 1987. A palynological zonation for the Cretaceous, Tertiary, and Quaternary of northern South America. *AASP Contrib. Ser.,* 19:7–76.

Munsell Soil Color Charts, 1975. Baltimore (Munsell Color).

Okada, H., and Bukry, D., 1980. Supplementary modification and introduction of code numbers to the low-latitude coccolith biostratigraphic zonation (Bukry, 1973; 1975). *Mar. Micropaleontol.,* 5:321–325.

Parmenter, C., and Folger, D.W., 1974. Eolian biogenic detritus in deep sea sediments: a possible index of equatorial ice age aridity. *Science,* 185:695–698.

Pflaumann, U., 1986. Sea-surface temperatures during the last 750,000 years in the eastern equatorial Atlantic: planktonic foraminiferal record of "Meteor"-cores 13519, 13521, and 16415. *"Meteor" Forschungsergeb. Reihe C,* 40:137–161.

Philips Analytical, 1990. *PC-APD Software for Automated Powder Diffraction* (3rd ed.): Operation manual for program vers. 3.0. Almelo, Netherlands.

Pirmez, C., 1994. Growth of a submarine meandering channel-levee system on the Amazon Fan [Ph.D. thesis]. Columbia Univ., New York.

Pozzi, J.-P., Barthés, V., Thibal, J., Pocachard, J., Lim, M., Thomas, T., and Pages, G., 1993. Downhole magnetostratigraphy in sediments: comparison with the paleomagnetism of a core. *J. Geophys. Res.,* 98:7939–7957.

Pozzi, J.-P., Martin, J.P., Pocachard, J., Feinberg, H., and Galdeano, A., 1988. In situ magnetostratigraphy: interpretation of magnetic logging in sediments. *Earth Planet. Sci. Lett.,* 88:357–373.

Pratson, E.L., Broglia, C., and Jarrard, R., 1993. Data report: geochemical well logs through Cenozoic and Quaternary sediments from Sites 815, 817, 820, 822, and 823. *In* McKenzie, J.A., Davies, P.J., Palmer-Julson, A., et al., *Proc. ODP, Sci. Results,* 133: College Station, TX (Ocean Drilling Program), 795–817.

Prell, W.L., and Damuth, J.E., 1978. The climate related diachronous disappearance of *Pulleniatina obliquiloculata* in Late Quaternary sediments of the Atlantic and Caribbean. *Mar. Micropaleontol.,* 3:267–277.

Prell, W.L., Imbrie, J., Martinson, D.G., Morley, J.J., Pisias, N.G., Shackleton, N.J., and Streeter, H.F., 1986. Graphic correlation of oxygen isotope stratigraphy: application to the late Quaternary. *Paleoceanography,* 1:137–162.

Pujol, C., and Duprat, J., 1983. Quaternary planktonic foraminifers of the southwestern Atlantic (Rio Grande Rise) Deep Sea Drilling Project Leg 72. *In* Barker, P.F., Carlson, R.L., Johnson, D.A., et al., *Init. Repts. DSDP,* 72: Washington (U.S. Govt. Printing Office), 601–615.

Pyle, M.R., 1984. Vane shear data on undrained residual strength. *J. Geotech. Engr. Div., Am. Soc. Civ. Eng.,* 110:543–547.

Raffi, I., Backman, J., Rio, D., and Shackleton, N.J., 1993. Plio-Pleistocene nannofossil biostratigraphy and calibration to oxygen isotopes stratigraphies from Deep Sea Drilling Project Site 607 and Ocean Drilling Program Site 677. *Paleoceanography,* 8:387–408.

Ruckebusch, G., 1983. A Kalman filtering approach to natural gamma ray spectroscopy in well logging. *IEEE Trans. Autom. Control,* AC-28:372–380.

Schlumberger, 1989. *Log Interpretation Principles/Applications:* Houston, TX (Schlumberger Educational Services).

Schrader, H.J., and Gersonde, R., 1978. Diatoms and silicoflagellates. *Utrecht Micropaleontol. Bull.,* 17:129–176.

Schweitzer, J.S., Grau, J.A., and Hertzog, R.C., 1988. Precision and accuracy of short-lived activation measurements for in situ geological analyses. *J. Trace Microprobe Techniques,* 6:437–451.

Scott, H.D., and Smith, M.P., 1973. The aluminum activation log. *Log Analyst,* 14:3–12.

Serra, O., 1989. *Formation MicroScanner Image Interpretation:* Houston (Schlumberger Educ. Services), SMP-7028.

Serra, O., 1984. *Fundamentals of Well-Log Interpretation* (Vol. 1): *The Acquisition of Logging Data:* Amsterdam (Elsevier).

Shepard, F., 1954. Nomenclature based on sand-silt-clay ratios. *J. Sediment. Petrol.,* 24:151–158.

Shipboard Scientific Party, 1992. Explanatory notes. *In* Mayer, L., Pisias, N., Janecek, T., et al., *Proc. ODP, Init. Repts.,* 138: College Station, TX (Ocean Drilling Program), 13–42.

Shipboard Scientific Party, in press. Explanatory notes. *In* Curry, W.B., Shackleton, N.J., Richter, C., et al., *Proc. ODP, Init. Repts.,* 154: College Station, TX (Ocean Drilling Program).

Stein, R., ten Haven, H.L., Littke, R., Rullkötter, J., and Welte, D.H., 1989. Accumulation of marine and terrigenous organic carbon at upwelling Site 658 and nonupwelling Sites 657 and 659: implications for the reconstruction of paleoenvironments in the eastern subtropical Atlantic through late Cenozoic times. *In* Ruddiman, W., Sarnthein, M., et al., *Proc. ODP, Sci. Results,* 108: College Station, TX (Ocean Drilling Program), 361–385.

Stupavsky, M., and Gravenor, C.P., 1984. Paleomagnetic dating of Quaternary sediments: a review. *In* Mahaney, W.C. (Ed.), *Quaternary Dating Methods:* Amsterdam (Elsevier).

Takayama, T., and Sato, T., 1987. Coccolith biostratigraphy of the North Atlantic Ocean, Deep Sea Drilling Project Leg 94. *In* Ruddiman, W.F., Kidd, R.B., Thomas, E., et al., *Init. Repts. DSDP,* 94 (Pt. 2): Washington (U.S. Govt. Printing Office), 651–702.

Terry, R.D., and Chilingar, G.V., 1955. Summary of "Concerning some additional aids in studying sedimentary formations" by M. S. Shvetsov. *J. Sediment. Petrol.,* 25:229–234.

Thierstein, H.R., Geitzenauer, K., Molfino, B., and Shackleton, N.J., 1977. Global synchroneity of late Quaternary coccolith datum levels: validation by oxygen isotopes. *Geology,* 5:400–404.

Timur, A., and Toksöz, M.N., 1985. Downhole geophysical logging. *Annu. Rev. Earth Planet. Sci.,* 13:315–344.

Van der Hammen, T., 1974. The Pleistocene changes of vegetation and climate in tropical South America. *J. Biogeogr.,* 1:3–26.

van Morkhoven, F.P.C.M., Berggren, W.A., and Edwards, A.S., 1986. Cenozoic cosmopolitan deep-water benthic foraminifera. *Bull. Cent. Rech. Explor.-Prod. Elf-Aquitaine,* Mem. 11.

Von Herzen, R.P., and Maxwell, A.E., 1959. The measurement of thermal conductivity of deep-sea sediments by a needle-probe method. *J. Geophys. Res.,* 64:1557–1563.

Wentworth, C.K., 1922. A scale of grade and class terms of clastic sediments. *J. Geol.,* 30:377–392.

Wyllie, M.R.J., Gregory, A.R., and Gardner, L.W., 1956. Elastic wave velocities in heterogeneous and porous media. *Geophysics,* 21:41–70.

Yokota, T., Kinoshita, H., and Uyeda, S., 1980. New DSDP (Deep Sea Drilling Project) downhole temperature probe utilizing IC RAM (memory) elements. *Bull. Earthquake Res. Inst., Univ. Tokyo,* 55:75–88.

Ms 155IR-104